

**APPLICATION OF THE SPECTRAL WAVE MODEL
SWAN IN DELAWARE BAY**

BY

WENTING QIN, JAMES T. KIRBY AND MOHSEN BADIEY

RESEARCH REPORT NO. CACR-05-09
NOVEMBER 2005

This study was supported by the Delaware Sea Grant Program
Project Number NOAA SG0507 R/ETE-3



CENTER FOR APPLIED COASTAL RESEARCH

Ocean Engineering Laboratory
University of Delaware
Newark, Delaware 19716

ACKNOWLEDGEMENT

The study was supported by the Delaware Sea Grant Program, Project Number NOAA SG0507 R/ETE-3.

TABLE OF CONTENTS

LIST OF FIGURES	vi
LIST OF TABLES	xv
ABSTRACT	xvi

Chapter

1 INTRODUCTION	1
1.1 Background	1
1.2 Review of SWAN Applications	2
1.3 Outline of Present Work	7
2 NUMERICAL MODEL	9
2.1 Action Balance Equation	9
2.2 Wind Generation	11
2.3 Dissipation	12
2.4 Nonlinear Wave-Wave Interactions	15
2.5 Numerical Solution Scheme	15
2.6 Boundary Conditions	17
2.7 Initial Condition	17
3 MODEL IMPLEMENTATION FOR DELAWARE BAY	19
3.1 Model Domain	19
3.2 Model Grid	20
3.3 Basic Input	20
3.4 Boundary Condition	21
3.5 Wind Data from Lighthouse	22
3.6 Currents	24

4	MODEL SENSITIVITY	37
4.1	Spatially Interpolated Wind	37
4.2	Influence of Tidal Currents	41
4.2.1	Shelf Circulation Model ROMS	42
4.2.2	Coupling the Model Systems	43
4.3	Conclusion	44
5	MODEL-DATA COMPARISON	74
5.1	HFA97 Experiment	74
5.2	2003 Experiment	76
5.3	2005 Experiment	79
5.4	Conclusion	82
6	CONCLUSION	105
6.1	Conclusion	105
6.2	Suggestions for Future Work	107
	BIBLIOGRAPHY	108

LIST OF FIGURES

3.1	Bathymetry in simulation. The large scale mesh represents the grid system used in WWIII model around the area of SWAN model domain. The wave parameters calculated by WWIII are chosen at the black points which are set at the seaward boundary (approximately along 100m isobath) in SWAN simulation. (Unit in color bar is m)	25
3.2	Bathymetry in the simulation coordination. Black squares A , B , C and D are the points nearest to the black points in Figure 3.1 along 100m isobath. (Unit in color bar is m)	26
3.3	Grid cells in the model domain with 0m (blue line), 10m, 20m, 50m, 100m (red lines) isobaths	27
3.4	Grid cell size in x -direction (left panel) and y -direction (right panel) (Unit in color bar is km)	28
3.5	Significant wave height at points A , B , C and D at seaward boundary from WWIII in 2003	29
3.6	Peak period at points A , B , C and D at seaward boundary from WWIII in 2003	30
3.7	Peak direction (CCW) at points A , B , C and D at seaward boundary from WWIII in 2003	31
3.8	H_s distribution driven by boundary condition from WWIII at 00:00 Oct. 21, in 2003	32
3.9	Fourteen Ft. Bank Lighthouse in Delaware Bay	33
3.10	Location of DBOS on Fourteen Ft. Bank Lighthouse (Red cross, 75°11'W, 39°01'N) in Delaware Bay (Badiy et al., 2002)	34

3.11	Wind speed and direction from Fourteen Ft. Bank Lighthouse in 2003. In the upper panel, the black line is the wind speed from DBOS record for every <i>6min</i> , the red line is the averaged wind speed for every <i>1hr</i> , the blue line is the adjusted wind speed from 18 <i>m</i> to 10 <i>m</i> above the sea surface. In the lower panel, the black line is the wind direction from DBOS record for every <i>6min</i> , the red line is the averaged wind direction for every <i>1hr</i>	35
3.12	Significant wave height along wind blowing up direction with different uniform currents on even bottom with 10 <i>m</i> water depth .	36
4.1	PORTS Stations and NDBC 44009 (red circle), Fourteen Ft. Bank Lighthouse (red square) in Delaware Bay (Whitney, 2003)	45
4.2	Wind speed and direction (CCW) measured at different stations during October 27 through 29, 2003. Black filled diamond: NDBC 44009; Green diamond: Lewes; Magenta diamond: Brandywine Shoals Light; Red diamond: Ship John Shoal Light; Black square: Delaware City; Blue circle: Fourteen Foot Bank Lighthouse	46
4.3	Spatially constant wind field (blue arrow) and interpolated wind field (black arrow) in model domain in the left panel; Right panel shows the three wind vectors used in interpolation and a reference vector at 13:00 October 27, 2003	47
4.4	Significant wave height with spatially constant wind field (left panel) and interpolated wind field (right panel) in model domain at 13:00 October 27, 2003 (Unit in color bar is <i>m</i>)	48
4.5	Difference of significant wave height with spatially constant wind field and interpolated wind field in model domain at 13:00 October 27, 2003 (Unit in color bar is percentage)	48
4.6	Peak period with spatially constant wind field (left panel) and interpolated wind field (right panel) in model domain at 13:00 October 27, 2003 (Unit in color bar is <i>s</i>)	49
4.7	Difference of peak period with spatially constant wind field and interpolated wind field in model domain at 13:00 October 27, 2003 (Unit in color bar is percentage)	49

4.8	Comparison of Significant wave height (H_s), Peak period (T_p) near Fourteen Ft. Bank Lighthouse between spatially constant wind field (blue diamond), interpolated wind field (red cross) and measured by WSB (black circle) at some time in 2003	50
4.9	Spatially constant wind field (blue arrow) and interpolated wind field (black arrow) in model domain in the left panel; Right panel shows the three wind vectors used in interpolation and a reference vector at 20:00 October 27, 2003	51
4.10	Significant wave height with spatially constant wind field (left panel) and interpolated wind field (right panel) in model domain at 20:00 October 27, 2003 (Unit in color bar is m)	52
4.11	Difference of significant wave height with spatially constant wind field and interpolated wind field in model domain at 20:00 October 27, 2003 (Unit in color bar is percentage)	52
4.12	Peak period with spatially constant wind field (left panel) and interpolated wind field (right panel) in model domain at 20:00 October 27, 2003 (Unit in color bar is s)	53
4.13	Difference of peak period with spatially constant wind field and interpolated wind field in model domain at 20:00 October 27, 2003 (Unit in color bar is percentage)	53
4.14	Spatially constant wind field (blue arrow) and interpolated wind field (black arrow) in model domain in the left panel; Right panel shows the three wind vectors used in interpolation and a reference vector at 03:00 October 28, 2003	54
4.15	Significant wave height with spatially constant wind field (left panel) and interpolated wind field (right panel) in model domain at 03:00 October 28, 2003 (Unit in color bar is m)	55
4.16	Difference of significant wave height with spatially constant wind field and interpolated wind field in model domain at 03:00 October 28, 2003 (Unit in color bar is percentage)	55

4.17	Peak period with spatially constant wind field (left panel) and interpolated wind field (right panel) in model domain at 03:00 October 28, 2003 (Unit in color bar is s)	56
4.18	Difference of peak period with spatially constant wind field and interpolated wind field in model domain at 03:00 October 28, 2003 (Unit in color bar is percentage)	56
4.19	Spatially constant wind field (blue arrow) and interpolated wind field (black arrow) in model domain in the left panel; Right panel shows the three wind vectors used in interpolation and a reference vector at 00:00 October 29, 2003	57
4.20	Significant wave height with spatially constant wind field (left panel) and interpolated wind field (right panel) in model domain at 00:00 October 29, 2003 (Unit in color bar is m)	58
4.21	Difference of significant wave height with spatially constant wind field and interpolated wind field in model domain at 00:00 October 29, 2003 (Unit in color bar is percentage)	58
4.22	Peak period with spatially constant wind field (left panel) and interpolated wind field (right panel) in model domain at 00:00 October 29, 2003 (Unit in color bar is s)	59
4.23	Difference of peak period with spatially constant wind field and interpolated wind field in model domain at 00:00 October 29, 2003 (Unit in color bar is percentage)	59
4.24	Spatially constant wind field (blue arrow) and interpolated wind field (black arrow) in model domain in the left panel; Right panel shows the three wind vectors used in interpolation and a reference vector at 12:00 October 29, 2003	60
4.25	Significant wave height with spatially constant wind field (left panel) and interpolated wind field (right panel) in model domain at 12:00 October 29, 2003 (Unit in color bar is m)	61
4.26	Difference of significant wave height with spatially constant wind field and interpolated wind field in model domain at 12:00 October 29, 2003 (Unit in color bar is percentage)	61

4.27	Peak period with spatially constant wind field (left panel) and interpolated wind field (right panel) in model domain at 12:00 October 29, 2003 (Unit in color bar is s)	62
4.28	Difference of peak period with spatially constant wind field and interpolated wind field in model domain at 12:00 October 29, 2003 (Unit in color bar is percentage)	62
4.29	Comparison of depth-averaged current velocity between measurement of ADCP (circle) and ROMS (solid line) at measuring station in October, 2003. Positive values point to east and north.	63
4.30	Spatially variable wind field (left panel) and tidal current field (right panel) in model domain at 20:00 October 27, 2003	64
4.31	Significant wave height without (left panel) and with (right panel) tidal current field on spatially variable wind field in model domain at 20:00 October 27, 2003 (Unit in color bar is m)	65
4.32	Difference of significant wave height with and without current field in spatially interpolated wind field in model domain at 20:00 October 27, 2003 (Unit in color bar is percentage)	65
4.33	Peak period without (left panel) and with (right panel) tidal current field on spatially variable wind field in model domain at 20:00 October 27, 2003 (Unit in color bar is s)	66
4.34	Difference of peak period with and without current field in spatially interpolated wind field in model domain at 20:00 October 27, 2003 (Unit in color bar is percentage)	66
4.35	Comparison of Significant wave height (H_s), Peak period (T_p) near Fourteen Ft. Bank Lighthouse without (red cross) and with (blue diamond) tidal current field on spatially variable wind field and measured data by WSB (black circle) at some time in 2003	67
4.36	Spatially variable wind field (left panel) and tidal current field (right panel) in model domain at 03:00 October 28, 2003	68

4.37	Significant wave height without (left panel) and with (right panel) tidal current field on spatially variable wind field in model domain at 03:00 October 28, 2003 (Unit in color bar is m)	69
4.38	Difference of significant wave height with and without current field in spatially interpolated wind field in model domain at 03:00 October 28, 2003 (Unit in color bar is percentage)	69
4.39	Peak period without (left panel) and with (right panel) tidal current field on spatially variable wind field in model domain at 03:00 October 28, 2003 (Unit in color bar is s)	70
4.40	Difference of peak period with and without current field in spatially interpolated wind field in model domain at 03:00 October 28, 2003 (Unit in color bar is percentage)	70
4.41	Spatially variable wind field (left panel) and tidal current field (right panel) in model domain at 00:00 October 29, 2003	71
4.42	Significant wave height without (left panel) and with (right panel) tidal current field on spatially variable wind field in model domain at 00:00 October 29, 2003 (Unit in color bar is m)	72
4.43	Difference of significant wave height with and without current field in spatially interpolated wind field in model domain at 00:00 October 29, 2003 (Unit in color bar is percentage)	72
4.44	Peak period without (left panel) and with (right panel) tidal current field on spatially variable wind field in model domain at 00:00 October 29, 2003 (Unit in color bar is s)	73
4.45	Difference of peak period with and without current field in spatially interpolated wind field in model domain at 00:00 October 29, 2003 (Unit in color bar is percentage)	73
5.1	First two panels: measured wind speed, wind direction measured at DBOS from 08:13 Sept. 23 to 18:23 Sept. 29, 1997; Third panel: H_s calculated by SWAN with uniform wind field without (black line) and with (red line) current fields. Acoustic experiment data are black circles; Last panel: θ_p comparison between no-current (black diamonds) and current (red crosses)	84

5.2	First panel: Simulated depth-averaged current velocity in east-west (black line) and north-south (red line) at HFA experiment site from 08:13 Sept. 23 to 18:23 Sept. 29, 1997. Second panel: Comparison of depth-averaged current velocity between measurement of ADCP (blue circle) and ROMS (black line) in east-west. Positive values point to east and north.	85
5.3	Left panel: Recorded wind speed (black solid line) and direction (red points, CCW) during 08:13 Sept. 23 through 18:23 Sept 29, 1997 at Fourteen Ft. Bank Lighthouse; Middle panel: Frequency spectrum from acoustic experiment; Right panel: Frequency spectrum from SWAN simulation with uniform wind field	86
5.4	Left panel: Recorded wind speed (black solid line) and direction (red points, CCW) during 08:13 Sept. 23 through 18:23 Sept 29, 1997 at Fourteen Ft. Bank Lighthouse; Middle panel: Frequency spectrum from acoustic experiment; Right panel: Frequency spectrum from SWAN simulation with uniform wind field and current fields from ROMS	87
5.5	Frequency spectrum at different times in 1997. Black line: spatially uniform wind fields without current fields; Blue line: spatially uniform wind fields with current fields; Black circles: measured data	88
5.6	Recorded wind speed and direction at three locations: NOAA buoy station (black star); Delaware City (red diamond); Fourteen Ft. Bank Lighthouse (blue circle) during 23:00 October 20 through 22:00 October 29, 2003	89
5.7	Left panel: Recorded wind speed (black solid line) and direction (red points, CCW) during 11:00 October 27 through 10:00 October 29, 2003 at Fourteen Ft. Bank Lighthouse; Middle panel: Frequency spectrum from WSB; Right panel: Frequency spectrum from SWAN simulation with uniform wind field	90
5.8	Left panel: Recorded wind speed (black solid line) and direction (red points, CCW) during 11:00 October 27 through 10:00 October 29, 2003 at Fourteen Ft. Bank Lighthouse; Middle panel: Frequency spectrum from WSB; Right panel: Frequency spectrum from SWAN simulation with uniform wind field and current fields from ROMS .	91

5.9	Left panel: Recorded wind speed (black solid line) and direction (red points, CCW) during 11:00 October 27 through 10:00 October 29, 2003 at Fourteen Ft. Bank Lighthouse; Middle panel: Frequency spectrum from WSB; Right panel: Frequency spectrum from SWAN simulation with variable wind field and current fields from ROMS	92
5.10	Frequency spectrum at different times in 2003. Black line: spatially uniform wind fields; Blue line: spatially uniform wind fields and current fields; Red line: spatially variable wind fields and current fields; Black circles: measured data by WSB	93
5.11	Comparison of H_s and θ_p with different wind fields and current fields during 11:00 October 27 through 10:00 October 29, 2003 at Fourteen Ft. Bank Lighthouse. First panel: wind speed; Second panel: wind vector; Third panel: current panel; Fourth panel: H_s with uniform wind field only (black line), with uniform wind field and current field (blue line) and with variable wind field and current field (red line); Fifth panel: θ_p with uniform wind field only (black stars), with uniform wind field and current field (blue crosses) and with variable wind field and current field (red diamonds). The black circles are the values measured by WSB.	94
5.12	Recorded wind speed and direction at three stations: NDBC 44009 (black star); Delaware City (red diamond); Fourteen Ft. Bank Lighthouse (blue circle) during 00:00 May 22 through 23:00 May 29, 2005	95
5.13	Significant wave height at points A , B , C and D at seaward boundary from WWIII in 2005	96
5.14	Peak period at points A , B , C and D at seaward boundary from WWIII in 2005	97
5.15	Peak direction (CCW) at points A , B , C and D at seaward boundary from WWIII in 2005	98
5.16	Comparison of depth-averaged current velocity between measurement of ADCP (circle) and ROMS (solid line) at measuring station in May, 2005. Positive values point to east and north.	99

5.17	Left panel: Recorded wind speed (black solid line) and direction (red points, CCW) during 13:00 May 22 through 15:00 May 27, 2005 at Fourteen Ft. Bank Lighthouse; Middle panel: Frequency spectrum from WSB; Right panel: Frequency spectrum from SWAN simulation with uniform wind field	100
5.18	Left panel: Recorded wind speed (black solid line) and direction (red points, CCW) during 13:00 May 22 through 15:00 May 27, 2005 at Fourteen Ft. Bank Lighthouse; Middle panel: Frequency spectrum from WSB; Right panel: Frequency spectrum from SWAN simulation with uniform wind field and current fields from ROMS .	101
5.19	Left panel: Recorded wind speed (black solid line) and direction (red points, CCW) during 13:00 May 22 through 15:00 May 27, 2005 at Fourteen Ft. Bank Lighthouse; Middle panel: Frequency spectrum from WSB; Right panel: Frequency spectrum from SWAN simulation with variable wind field and current fields from ROMS .	102
5.20	Frequency spectrum at different times in 2005. Black line: spatially uniform wind fields; Blue line: spatially uniform wind fields and current fields; Red line: spatially variable wind fields and current fields; Black circles: measured data by WSB	103
5.21	First panel is the wind vector recorded at Fourteen Ft. Bank Lighthouse during May 22 through May 27, 2005; Second panel shows the current vector at the measurd station calculated by ROMS; Third panel shows H_s with uniform wind field only (black solid line), with uniform wind field and current field (blue solid line) and with variable wind field and current field (red dash line); Fourth panel shows θ_p with uniform wind field only (black stars), with uniform wind field and current field (blue crosses) and with variable wind field and current field (red diamonds). The black circles are the values measured by WSB.	104

LIST OF TABLES

4.1	Wind speed and direction at three stations	39
5.1	Overall mean values of statistical parameters at the measuring station (with and without current field)	82
5.2	Overall mean values of statistical parameters at the measuring station (uniform wind field and variable wind field)	82

ABSTRACT

SWAN (Simulating Waves Nearshore) is a third-generation numerical wave model to simulate the random, short-crested, wind-generated waves in coastal regions with shallow water and ambient currents. This study focuses on the application of SWAN in Delaware Bay.

A bathymetry based on an orthogonal curvilinear grid taken from Whitney (2003), including the entire Delaware Bay and its adjacent ocean region, is used as the model domain. The grid has higher resolution in the bay than offshore, satisfying the resolution need in shallow water and calculation efficiency. Most of the physical processes presented in SWAN are utilized in the simulations, such as wave shoaling, refraction, nonlinear interactions, depth-induced breaking, wave-current interaction, bottom friction and whitecapping dissipation. The offshore boundary condition is set by the wave parameters from WAVEWATCH III simulation.

Two sensitivity factors in SWAN model are discussed. One is the wind field distribution in space. On one hand, SWAN is run with a uniform wind field; on the other hand, it is driven by spatially variable wind field. SWAN is sensitive to the current field as well. The current field calculated by ROMS (Regional Ocean Model System) with tidal input at seaward boundary has been introduced into SWAN model.

Finally, three sets of field measurement data are used to test SWAN simulation results. First, an experiment was conducted in Delaware Bay in September 1997 to investigate acoustic fluctuations and the environmental parameters. The sea surface elevation and spectrum were measured using an inverted echo sounding

technique. In 2003 and 2005, a Wave Sentry Buoy (WSB) was deployed to measure the surface at the same site as experiment in 1997. The simulated current velocities from ROMS at the measuring station are compared to the ADCP data. SWAN simulations during these periods are compared to the field data in significant wave height, dominant direction and frequency spectrum.

Chapter 1

INTRODUCTION

1.1 Background

Delaware Bay is a main part of the Delaware River estuary, which is one of the major estuaries on the U.S. east coast. The bay is fed by the Delaware River and empties into the Atlantic Ocean between Cape Henlopen on the Delaware side and Cape May on the New Jersey side. It is bordered by the state of Delaware on the south and the state of New Jersey on the north. It has a productive ecosystem with a range of habitats for many different species of plants and animals. The water body in the bay is widely used in transportation, fishing and recreation. By the end of 19th century, the upper estuary was contaminated heavily by increased population and industrialization. It became worse through World War II, and the water had zero dissolved oxygen in some warmer months of the year up through 1950. Since then, people's attention and effort improved the estuary's water quality dramatically. Although the Delaware estuary is much cleaner than before, further improvement and protection are still required. It is necessary and important for us to know the physical and ecological processes well in the estuary.

Winds, tides and freshwater inflows as well as discharge from human activities are the main forcing to affect the evolution of the estuary. For instance, the surface waves generated by winds blowing through the bay are responsible for the littoral sediment transport and shoreline erosion. The waves and tidal currents sometimes slow down the pollution flowing into the bay and sometimes speed the spreading

of the contamination. The ability to conduct simultaneous measurement of surface water waves and the capability to predict and assess their potential impact on the environment is of critical importance to populations who live in coastal regions.

The nearshore wind waves statistical characteristics are widely applied in coastal engineering design, safe management of coastal resources and resorts, studies of sediment transport, coastal erosion and pollution processes. So surface waves and their interaction with currents are more concerned in coastal areas. A well developed wave forecast capability that utilizes the real-time measurements currently available throughout Delaware Bay and the adjacent Atlantic region could be used by local and federal agencies with applications to hazard evaluation, shoreline erosion management, and estuarine environmental studies. Furthermore, the accurate prediction of surface wave conditions can be combined with weather prediction to enhance the safety of mariners and fishermen in this area.

1.2 Review of SWAN Applications

Several types of numerical models for coastal wave processes have been developed. For larger scale application, spectral phase-averaged models are the most suitable (Battjes, 1994). Waves in the deep ocean can be well predicted by third generation wave models based on the energy or action balance equation, such as the Wave Model (WAM) (WAMDI Group, 1988), WAVEWATCH model of Tolman (1991), the model of Li and Mao (1992), or the Program for Hindcasting of Waves in Deep, Intermediate and Shallow Water (PHIDIAS) model of Van Vledder et al. (1994). Most of these models cannot be realistically applied to coastal regions with horizontal scales less than 20-30km and water depth less than 20-30m with estuaries, tidal inlets, barrier islands, tidal flats, or channels, because shallow water effects of depth-induced wave breaking and triad wave-wave interaction are not included in these simulations (Booij et al., 1999). Also, the explicit numerical schemes for propagation used in these models requires an impracticably short time

step for high spatial resolution in coastal applications. Booij et al. (1999) developed a similar model called Simulating Waves Nearshore (SWAN) to adapt the shallow water formulations from deep water processes to shallow water by incorporating (1) the use of shallow-water phase speed in the expression for wind input; (2) a depth-dependent scaling of the quadruplet wave-wave interactions; (3) a reformulation of the whitecapping in terms of wave number rather than frequency; (4) adding bottom dissipation; (5) depth-induced wave breaking and (6) triad wave-wave interactions.

Ris et al. (1999) verified SWAN for cases of Haringvliet, Norderneyer Seegat and Friesche Zeegat in Netherlands and Germany. The time for waves to travel through these areas is smaller than the time scale for variation of wind, current and tide, so the stationary (time-independent) mode was used. The wind speed and direction were assumed to be uniform over the computed area. Repeated computations with various source terms activated and deactivated investigated the contribution of each term to the significant wave height and mean wave period. The difference between SWAN results and observations were analyzed using statistical characteristics such as the scatter index (SI), model performance index (MPI) and operational performance index (OPI).

Gorman and Neilson (1999) used SWAN to simulate wave transformation in Manukau Harbor, a New Zealand estuary with relatively large fetches and extensive intertidal flats. The simulation incorporated refraction by currents, which were simulated by a circulation model 3DD (Black, 1983; Black et al., 1993). SWAN was run in the stationary mode. Two kinds of wind fields were applied: (1) wind observed at one platform was applied throughout the model domain; (2) a spatially variable wind field was constructed by interpolating winds measured at two platforms. The slower initial growth for the spatially variable wind field resulted in waves arriving at the mid-estuary banks with less energy in the lower frequencies. The wave spectrum obtained from pressure sensors and current meters set at six sites across the estuary

were compared with the model results. Nonlinear interaction was computed both by discrete interaction approximation (DIA) and by the EXACT-NL algorithm of Hasselmann and Hasselmann (1985).

Padilla-Hernández (2004) evaluated three third generation ocean wave models, SWAN (Version 40.20, Booij et al., 1999), WAM (Version WAMC4-PROMISE by Monbaliu et al., 2000 based on WAM4 version of the WAMDI group 1988), and WAVEWATCH III (Version 2.22 by Tolman, 2002, hereafter WWIII) through comparisons with measurements. They showed that WWIII with the hourly wind field and fine resolution grid performed better than the other models with the highest index of agreement and the smallest bias, scatter index and root mean square error for significant wave height (H_s). SWAN nested in WWIII performed better than SWAN nested in WAM. All models generally underestimated the peak storm H_s value. SWAN is more efficient due to its implicit scheme, which is not constrained by a CFL criterion when the time interval is increased.

Lalbeharry (2002) also used these three numerical models to simulate wave height for two extreme storms which traversed the Canadian buoy network in the Northwest Atlantic in 2000 and 2002. The winds forcing the models are generated by the Canadian Meteorological Centre (CMC) weather prediction at three-hourly intervals. He assumed there were no currents and the water depths were time-independent. Since the models are applied to shelf seas and the deep ocean in shallow water mode, the depth-induced wave breaking and SWAN triad nonlinear wave-wave interaction were ignored. SWAN has the option of using WAM3 or WAM4 physics for the source terms for wind wave generation (S_{in}) and dissipation due to whitecapping (S_{ds}), say SWAN(WAM3) and SWAN(WAM4). WAM4 were used both on fine and coarse grid as WAM4(FGSH) and WAM4(CGSH). Lalbeharry stated there was little or no difference between the WAM4(FGSH) and WAM4(CGSH) in significant wave height (H_s) and the impact of a higher resolution grid on H_s at water depths of their

buoys is rather marginal. SWAN(WAM3) outperformed SWAN(WAM4) for wave heights but not for peak periods. The fine or nested grid WAM4 is a little better than SWAN(WAM3). The coarse grid WAM4 did a better job than the coarse grid WWIII using Tolman and Chalikov physics in simulating the extreme wave heights.

Pires-Silva et al. (2002) assess the SWAN model in the west coast of Portugal, north of Sines Harbor. The model was forced with data from a "WAVEC" directional buoy, moored in 97m depth, and with simulation from a WAM model at seaward boundary. The significant wave height and the peak wave period were compared to the nearshore ADCP measurements (17m depth). The model was used in the stationary mode with variable tides, but without wind input. They concluded that the simulated periods were sensitive to the degree of sophistication of the offshore boundary condition. The 2D full spectra estimated with the Extended Maximum Likelihood Method (EMLM) used as a boundary condition made improvement in the statistics of the peak period.

Lin et al. (2002) compared the SWAN model with the Great Lakes Environmental Research Laboratory (GLERL) model in Chesapeake Bay (CB). The locally generated wind seas dominate wave climate in the mid- and upper-CB. Ocean swell from the Atlantic Ocean only affects the wave climate near the bay mouth. The wind was adjusted from anemometer height to 10m above sea elevation by modified wind profile (U.S. Army Corps of Engineers, SPM84; Monin and Obukhov, 1954; Large and Pond, 1982; Erickson, 1993). Then the converted wind velocities from three buoys were linearly interpolated over latitude to generate wind fields for wind input. Compared to measured wave data, both SWAN and GLERL over-predicted significant wave height. Both models slightly under-predicted peak period with a fairly large scatter and low correlation coefficient. The significant wave height distribution predicted by SWAN and GLERL for the same wind field showed significant differences in deeper water areas of the Bay. The GLERL model runs 50 times faster

than the SWAN model, but the final choice still needs more comprehensive testing.

Rogers et al. (2002) investigated the wave growth and decay characteristics in SWAN. They found that there was consistent under-prediction of lower-frequency (0.05-0.19Hz) energy by comparing the model results with measurements from the SandyDuck'97 experiment. The wave model has such questionable performance in duration-limited simulations because high-frequency wave components generally reach equilibrium state early in the growth process and could be predicted well, but low frequencies may be predicted poorly until they approach equilibrium state. Then they presented two methods to improve the prediction of low-frequency energy. One is to alter the weighting of the relative wave number term that exists in whitecapping formulation. Another one is to disallow the breaking of swell. The modified model was applied to two other tests, Lake Michigan and Mississippi Bight. Although the agreement with observation was improved by the modification, they pointed out that there still needs development of the manner in which phase-associated processes is represented in stochastic models.

Chen et al. (2004) performed SWAN calculations of surface waves in Mobile Bay, Alabama using the linear wave growth formulation of Cavaleri and Malanotte-Rizzoli (1981). The curvilinear wave model is tested using both the laboratory data set on wave transformation over a circular shoal and measured field data in the bay. A three-dimensional circulation model Estuarine and Coastal Ocean Model (ECOM) is used to investigate the effect of estuarine circulation on wave predictions in the estuary by using the varying current field and water levels as the input to the wave model. The ambient currents and the water level affect wave propagation little in the channel, where the water is deep.

1.3 Outline of Present Work

Using existing lighthouses as observational platforms, a real-time observing system called the Delaware Bay Observing System (DBOS) provides real-time measurements of oceanographic and atmospheric conditions in Delaware Bay. Based on preliminary data collected at these stations, SWAN model is run and compared with the measured data. The following chapters describe the simulation model, experiments and the comparison of the simulated results and measured data, as well as the conclusion.

Chapter 2 details the SWAN model including the governing equations, generation force, dissipation formula, numerical scheme, boundary condition and initial condition.

Chapter 3 set up the model implementation for Delaware Bay. The model domain and bathymetry are presented. Grids are taken from Whitney (2003). Some of the basic parameters are set down. The boundary condition is specified by the spectrum information from WWIII. Wind is adjusted from the measured data to simulation input by an exponential profile. The effects of currents on waves are investigated by a simple case.

Chapter 4 discusses two sensitivity factors in the SWAN model. One is the distribution of wind in Delaware Bay and adjacent coastal area. Another one is effect of the current field.

Chapter 5 compares the SWAN model results with the measured data. One set of data is from the experiment conducted in September 1997 near Fourteen Ft. Bank Lighthouse in Delaware Bay, which investigated acoustic fluctuations due to the variable environmental parameters. Although during that experiment the sea surface was not directly measured by a surface rider buoy, the sea surface spectrum was calculated from acoustic wave reflection using a bottom mounted sound and receiver source (Heitsenrether, 2004). Another two sets of data are from

the experiments conducted in 2003 and 2005 near the same lighthouse. A Wave Sentry Buoy (WSB) was deployed to measure the surface. SWAN model results are compared to the experiment data.

Chapter 2

NUMERICAL MODEL

The SWAN (Simulating Waves Nearshore) model is a third-generation numerical wave model to compute random, short-crested, wind-generated waves in coastal regions with shallow water and ambient currents. Physical processes in SWAN include wave shoaling, refraction, nonlinear interactions, depth-induced breaking, wave-current interaction, and bottom friction and whitecapping dissipation. SWAN does not account for diffraction or reflections due to bottom scattering. SWAN is driven by local winds and wave input through boundary conditions, and waves are modulated by tidal currents. The numerical scheme is implicit, unconditionally stable and not subject to a Courant criteria.

2.1 Action Balance Equation

In the presence of ambient current, the action density is conserved while the energy density is not. The action density $N(\sigma, \theta)$ is equal to the energy density $E(\sigma, \theta)$ divided by the relative angular frequency σ , i.e. $N(\sigma, \theta) = E(\sigma, \theta)/\sigma$. SWAN solves for the evolution of the wave spectrum by using the action density spectrum. The governing equation for Cartesian coordinates is

$$\frac{\partial}{\partial t}N + \frac{\partial}{\partial x}c_x N + \frac{\partial}{\partial y}c_y N + \frac{\partial}{\partial \sigma}c_\sigma N + \frac{\partial}{\partial \theta}c_\theta N = \frac{S}{\sigma} \quad (2.1)$$

where x, y are horizontal Cartesian coordinates, t is time, θ is the propagation direction of each wave component, $c_x, c_y, c_\sigma, c_\theta$ stand for the propagation velocity

in x -space, y -space, σ -space, θ -space respectively. S is the source term in terms of energy density, which include the effects of generation, dissipation, and nonlinear wave-wave interaction. The first term on the left-hand side of Eq. (2.1) is the rate of change of action density in time, the second and third terms are propagation of action in physical space. The fourth and fifth terms show the shifting of the relative frequency and the refraction due to variations in depth and currents.

The propagation velocity is taken from linear wave theory (Whitham, 1974; Dingemans, 1997). Based on the dispersion relation $\sigma^2 = gk \tanh kh$, the group velocity without current velocity is calculated by $c_{g0} = \frac{\partial \sigma}{\partial k}$, where k is wave number, h is water depth, g is gravitational acceleration, and c_{g0} is dependent on x , y and σ . According to the deep water theory, $c_{g0} = \frac{g}{2\sigma}$. For very shallow water, $c_{g0} = \sqrt{gh}$. Finally, the group velocity with current velocity in terms of x , y , σ and θ is expressed by (Bretherton and Garrett, 1969):

$$c_g(x, y, \sigma, \theta) = c_{g0}(x, y, \sigma) + U_x \cos \theta + U_y \sin \theta \quad (2.2)$$

Then,

$$c_x = c_{g0} \cos \theta + U_x \quad (2.3)$$

$$c_y = c_{g0} \sin \theta + U_y \quad (2.4)$$

$$c_\sigma = \frac{k\sigma}{\sinh 2kh} \left[\frac{\partial h}{\partial t} + U_x \frac{\partial h}{\partial x} + U_y \frac{\partial h}{\partial y} \right] - c_{g0} k \left[\frac{\partial U_x}{\partial x} \cos^2 \theta + \frac{\partial U_x}{\partial y} \cos \theta \sin \theta + \frac{\partial U_y}{\partial x} \sin \theta \cos \theta + \frac{\partial U_y}{\partial y} \sin^2 \theta \right] \quad (2.5)$$

$$c_\theta = \frac{\sigma}{\sinh 2kh} \left[\frac{\partial h}{\partial x} \sin \theta - \frac{\partial h}{\partial y} \cos \theta \right] - \left[\frac{\partial U_x}{\partial x} - \frac{\partial U_y}{\partial y} \right] \sin \theta \cos \theta + \frac{\partial U_y}{\partial x} \sin^2 \theta - \frac{\partial U_x}{\partial y} \cos^2 \theta \quad (2.6)$$

in which U_x and U_y are the current velocity components in x - direction and y - direction respectively.

2.2 Wind Generation

The wind generation source term can be described as:

$$S_{in}(\sigma, \theta) = A + BE(\sigma, \theta) \quad (2.7)$$

The expression for A from Cavaleri and Malanotte-Rizzoli (1981) is used with a filter to eliminate wave growth at frequencies lower than the Pierson-Moskowitz frequency (Tolman, 1992a).

$$A = \frac{1.5 \times 10^{-3}}{g^2 2\pi} [U_* \max[0, \cos(\theta - \theta_w)]]^4 H \quad (2.8)$$

with

$$H = \exp(-(\sigma/\sigma_{PM}^*)^{-4}) \quad (2.9)$$

$$\sigma_{PM}^* = \frac{0.13g}{28U_*} 2\pi \quad (2.10)$$

in which θ_w is the wind direction, H is the filter and σ_{PM}^* is the peak frequency of the fully developed state according to Pierson and Moskowitz (1964).

Although the specified wind speed in SWAN is U_{10} , the speed at 10m elevation, the friction velocity U_* is used in computation. U_* is obtained by:

$$U_*^2 = C_D U_{10}^2 \quad (2.11)$$

where C_D is the drag coefficient from Wu (1982):

$$C_D(U_{10}) = \begin{cases} 1.2875 \times 10^{-3} & U_{10} < 7.5m/s \\ (0.8 + 0.065s/m \times U_{10}) \times 10^{-3} & U_{10} \geq 7.5m/s \end{cases} \quad (2.12)$$

B can be chosen from Komen et al. (1984) or Janssen (1989, 1991). The former expression is:

$$B = \max \left[0, 0.25 \frac{\rho_a}{\rho_w} \left[28 \frac{U_*}{c_{ph}} \cos(\theta - \theta_w) - 1 \right] \right] \sigma \quad (2.13)$$

in which c_{ph} is the phase speed, ρ_a and ρ_w are the density of air and water respectively.

Based on a quasi-linear wind-wave theory, Janssen (1989, 1991) expresses B as follows:

$$B = \beta \frac{\rho_a}{\rho_w} \left(\frac{U_*}{c_{ph}} \right)^2 [\max(0, \cos(\theta - \theta_w))]^2 \sigma \quad (2.14)$$

where β is Miles constant, which is estimated by:

$$\begin{aligned} \beta &= \frac{1.2}{\kappa^2} \lambda \ln^4 \lambda & \lambda \leq 1 \\ \beta &= 0 & \lambda > 1 \end{aligned} \quad (2.15)$$

with

$$\lambda = \frac{gz_e}{c_{ph}^2} e^r \quad (2.16)$$

$$r = \frac{\kappa C}{|U_* \cos(\theta - \theta_w)|} \quad (2.17)$$

where κ is the Von Karman constant, $\kappa = 0.41$. z_e is the effective surface roughness.

2.3 Dissipation

The dissipation terms of the wave energy include whitecapping $S_{ds,w}(\sigma, \theta)$, bottom friction $S_{ds,b}(\sigma, \theta)$, and depth-induced breaking $S_{ds,br}(\sigma, \theta)$.

The whitecapping formulation is (WAMDI, 1988)

$$S_{ds,w}(\sigma, \theta) = -\Gamma \tilde{\sigma} \frac{k}{\tilde{k}} E(\sigma, \theta) \quad (2.18)$$

in which Γ is a steepness dependent coefficient, k is wave number, and $\tilde{\sigma}$ and \tilde{k} denote a mean frequency and a mean wave number respectively.

The steepness dependent coefficient has been adapted by Günther et al. (1992) based on Janssen (1991a, 1991b) as

$$\Gamma = C_{ds} \left((1 - \delta) + \delta \frac{k}{\tilde{k}} \right) \left(\frac{\tilde{S}}{\tilde{S}_{PM}} \right)^p \quad (2.19)$$

where C_{ds} , δ and p are tunable coefficients. \tilde{S} is the overall wave steepness defined as:

$$\tilde{S} = \tilde{k} \sqrt{E_{tot}} \quad (2.20)$$

\tilde{S}_{PM} is the value of \tilde{S} for the Pierson-Moskowitz spectrum (1964, $\tilde{S}_{PM} = (3.02 \times 10^{-3})^{1/2}$).

$\tilde{\sigma}$, \tilde{k} and E_{tot} are calculated by (WAMDI, 1988)

$$\tilde{\sigma} = \left(E_{tot}^{-1} \int_0^{2\pi} \int_0^\infty \frac{1}{\sigma} E(\sigma, \theta), d\sigma, d\theta \right)^{-1} \quad (2.21)$$

$$\tilde{k} = \left(E_{tot}^{-1} \int_0^{2\pi} \int_0^\infty \frac{1}{\sqrt{k}} E(\sigma, \theta), d\sigma, d\theta \right)^{-2} \quad (2.22)$$

$$E_{tot} = \int_0^{2\pi} \int_0^\infty E(\sigma, \theta), d\sigma, d\theta \quad (2.23)$$

This steepness dependent coefficient is used when the wind input term B of Janssen (1991a) is used. Corresponding to the coefficient B of Komen et al. (1984), there is another expression for Γ in Cycle 3 of the WAM model. Komen et al. (1984) calculated C_{ds} , δ and p by closing the energy balance of the waves in idealized wave growth conditions for deep water. This implies that Γ depends on the formulation of wind input.

An alternative formulation for whitecapping is the Cumulative Steepness Method (CSM) from Alkyon et al. (2002).

$$S_{ds,w,csm}(\sigma, \theta) = \int_0^\sigma \int_0^{2\pi} k^2 |\cos(\theta - \theta')|^m E(\sigma, \theta) d\sigma d\theta \quad (2.24)$$

where m controls the directional dependence. The default value is $m = 0$. Then the whitecapping source term is expressed by:

$$S_{ds,w}(\sigma, \theta) = -C_w^{cms} S_{ds,w,csm}(\sigma, \theta) E(\sigma, \theta) \quad (2.25)$$

with a tunable coefficient C_w^{cms} . Default $C_w^{cms} = 1.8$.

The bottom friction dissipation can be expressed as:

$$S_{ds,b}(\sigma, \theta) = -C_{bottom} \frac{\sigma^2}{g^2 \sinh^2(kd)} E(\sigma, \theta) \quad (2.26)$$

in which C_{bottom} is a bottom friction coefficient. SWAN uses the simplest version of several types of friction models. They are: the empirical Joint North Sea Wave Project (JONSWAP) model of Hasselmann et al. (1973) with $C_{bottom} = 0.038m^2s^{-3}$ for swell conditions and $C_{bottom} = 0.067m^2s^{-3}$ for wind sea conditions; the drag law model of Collins (1972) with $C_{bottom} = C_f g U_{rms}$ with bottom friction coefficient C_f , gravitational acceleration g , and root-mean-square wave-induced orbital velocity at the bottom U_{rms} ; the eddy-viscosity model of Madsen et al. (1988) with $C_{bottom} = f_w g U_{rms} / \sqrt{2}$ and f_w taken from Jonsson (1966, 1980) and Jonsson and Carlsen (1976).

The depth-induced wave breaking in SWAN is the bore-based model of Battjes and Janssen (1978). The mean rate of energy dissipation per unit horizontal area due to wave breaking is

$$D_{tot} = -\frac{1}{4} \alpha_{BJ} Q_b \left(\frac{\bar{\sigma}}{2\pi} \right) H_m^2 \quad (2.27)$$

where $\alpha_{BJ} = 1$ in SWAN. H_m is the maximum wave height at given water depth d with $H_m = \gamma d$. In SWAN, the breaking parameter $\gamma = 0.73$. Q_b is the fraction of breaking waves determined by

$$\frac{1 - Q_b}{\ln Q_b} = -8 \frac{E_{tot}}{H_m^2} \quad (2.28)$$

$\bar{\sigma}$ is a mean frequency defined as:

$$\bar{\sigma} = E_{tot}^{-1} \int_0^{2\pi} \int_0^\infty \sigma E(\sigma, \theta), d\sigma, d\theta \quad (2.29)$$

The dissipation for a spectral component per unit time is calculated by extending the expression of Eldeberky and Battjes (1995) to include the spectral directions as following:

$$S_{ds,br} = D_{tot} \frac{E(\sigma, \theta)}{E_{tot}} \quad (2.30)$$

2.4 Nonlinear Wave-Wave Interactions

Quadruplet wave-wave interactions dominate the evolution of the spectrum in deep water. SWAN computes it with the discrete interaction approximation (DIA) of Hasselmann et al. (1985). Triad wave-wave interactions transfer energy from lower frequencies to higher frequencies in very shallow water. The formulation used in SWAN is taken from Eldeberky and Battjes (1996). For finite-depth water, the quadruplet wave-wave interactions for a JONSWAP-type spectrum can be scaled with a simple expression (Hasselmann and Hasselmann, 1981).

2.5 Numerical Solution Scheme

The numerical solution scheme in SWAN is an implicit scheme. The action balance equation (2.1) is discretized by:

$$\begin{aligned} & \left[\frac{N^{i_t, n} - N^{i_t, n-1}}{\Delta t} \right]_{i_x, i_y, i_\sigma, i_\theta} + \left[\frac{[c_x N]_{i_x} - [c_x N]_{i_x-1}}{\Delta x} \right]_{i_y, i_\sigma, i_\theta}^{i_t, n} + \left[\frac{[c_y N]_{i_y} - [c_y N]_{i_y-1}}{\Delta y} \right]_{i_x, i_\sigma, i_\theta}^{i_t, n} \\ & + \left[\frac{(1 - \nu) [c_\sigma N]_{i_\sigma+1} + 2\nu [c_\sigma N]_{i_\sigma} - (1 + \nu) [c_\sigma N]_{i_\sigma-1}}{2\Delta\sigma} \right]_{i_x, i_y, i_\theta}^{i_t, n} \\ & + \left[\frac{(1 - \eta) [c_\theta N]_{i_\theta+1} + 2\eta [c_\theta N]_{i_\theta} - (1 + \eta) [c_\theta N]_{i_\theta-1}}{2\Delta\theta} \right]_{i_x, i_y, i_\sigma}^{i_t, n} \\ & = \left[\frac{S}{\sigma} \right]_{i_x, i_y, i_\sigma, i_\theta}^{i_t, n^*} \quad (2.31) \end{aligned}$$

in which i_t is the time level index, i_x , i_y , i_σ and i_θ are grid counters. Δt , Δx , Δy , $\Delta\sigma$, $\Delta\theta$ are the increments in time, physical space, and spectral space, respectively. n is the iterative of the computation. n^* is n or $n - 1$, which depends on the source term. ν and η are the coefficients to determine the scheme in spectral space is upwind or central.

In SWAN, implicit upwind schemes are chosen both in physical and in spectral space, supplemented with an implicit central approximation in spectral space. “Implicit” means that all derivatives of action density in t , x or y are formulated at one computational level i_t , i_x or i_y , except the derivative in the integration dimension for which also the previous or upwave level is used. The fact that in physical space the state at a grid point is determined by the state at the upwave grid points permits a decomposition of the spectral space into four quadrants (eight octants would be an alternative) (Booij, 1999).

The discrete action density both in physical and in spectral space is described by a large basic matrix. The matrix could be solved with a Gauss-Seidel technique (e.g., Golub and van Loan, 1986) by excluding refraction, frequency shifting, and nonlinear source terms. The matrix is decomposed in four sections (the above four directional quadrants), which are each solved in one step. Including the refraction and frequency shifting to the matrix, the solution of sub-matrix for each physical grid point is required. If $c_\sigma = 0$ (no current) or the depth is stationary, the sub-matrix is a tridiagonal matrix, which is solved by the Tomas algorithm (e.g., Abbott and Basco, 1989). If there is current or the depth is not stationary, the sub-matrix is a band matrix, which is solved by an iterative Incomplete Lower and Upper Triangular Matrix Decomposition-Bi-Conjugate Gradient Stabilized (ILU-BiCGSTAB) method (Vuik, 1993; Van der Vorst, 1992).

The basic matrix is solved iteratively until some break-off criteria are met. For instance, set the break-off criterion for the significant wave height, such as 0.1%, which means the change of significant wave height from one iteration to the next is less than 0.1%. Otherwise, the number of iteration with wave generated by wind is typically set as 5-15.

In the curvilinear grid, the gradient in each grid point at location (x_i, y_i) is approximately from the up-wind grid points. If the grid points are ordered in x ,

y -space with label i, j respectively, then

$$\frac{\partial}{\partial x} c_x N = \left[\frac{[c_x N]_{i,j} - [c_x N]_{i-1,j}}{\Delta \tilde{x}_1} \right] + \left[\frac{[c_x N]_{i,j} - [c_x N]_{i,j-1}}{\Delta \tilde{x}_2} \right] \quad (2.32)$$

in which $\Delta \tilde{x}_1 = \Delta x_1 - (\Delta y_1 / \Delta y_2) \Delta x_2$, $\Delta \tilde{x}_2 = \Delta x_2 - (\Delta y_2 / \Delta y_1) \Delta x_1$. The increments are $\Delta x_1 = x_{i,j} - x_{i-1,j}$, $\Delta x_2 = x_{i,j} - x_{i,j-1}$, $\Delta y_1 = y_{i,j} - y_{i-1,j}$, $\Delta y_2 = y_{i,j} - y_{i,j-1}$. The other terms in Eq. (2.1) are discretized in the same way.

2.6 Boundary Conditions

The boundary conditions in SWAN in physical and spectral space are fully absorbing for wave energy that is leaving the computational domain or crossing a coastline. In coastal region, the deep water boundary is specified by the incoming wave energy, while the lateral physical boundary is set to be zero. This choice will cause errors in the computational area near lateral boundary. Hence, the lateral boundary should be sufficiently far away from the area the users are interested in.

The shape of spectrum at the boundary of the computational grid could be defined as JONSWAP spectrum, Pierson-Moskowitz (PM) spectrum, Gaussian-shaped frequency spectrum, or simulated results provided by external model predictions.

2.7 Initial Condition

SWAN has four options for initial condition. The default initial spectra are computed from the local wind velocities by using the deep water growth curve of Kahma and Calkoen (1992) and cutting off at values of significant wave height and peak frequency from Pierson and Moskowitz (1964). The average spatial step size is used as fetch with local wind. The shape of the spectrum is default JONSWAP with a \cos^2 directional distribution. Another one is to set the initial spectra as $N = 0$. In this case, the waves are generated only by wind and become non-zero only by the presence of the coefficient of A in the growth model Eq. (2.7). The third option is to set the spectra in the entire computational area by the parameters of significant

wave height, peak or mean period, peak wave direction, the coefficient of directional spreading. The fourth option is to read the initial wave field from a file generated by a previous SWAN run.

Chapter 3

MODEL IMPLEMENTATION FOR DELAWARE BAY

Delaware Bay is a semi-enclosed bay. The waves in the bay are mostly locally generated wind waves. Ocean swell from the Atlantic Ocean only affects the region near the mouth of the bay. In this chapter, SWAN model is set up to simulate the waves mainly driven by the local wind in Delaware Bay. First, the model domain will be specified. The bathymetry is based on an orthogonal curvilinear grid. The physics, such as quartet interactions, triad interactions, whitecapping, breaking and friction are chosen in the model. The seaward boundary condition is specified by the wave parameters from WWIII. The wind data used in the simulation are from Fourteen Ft. Bank Lighthouse and Delaware Bay Observing System (DBOS). Finally, the effect of tidal currents is investigated in the simple case.

3.1 Model Domain

The simulation domain includes the entire Delaware estuary and the adjacent continental shelf with the corresponding bathymetry (Figure 3.1, Whitney, 2003). The offshore boundary is along the 100m isobath. It is important to have the offshore side follow an isobath where the tidal forcing will be applied. Although the Chesapeake Bay, Chincoteague Bay, Assawoman Bay, Indian River Bay, Great Egg Harbor, Great Bay, and smaller inlets are located geographically within the domain region, they are replaced by land in modeling. Also, the Delaware River is rotated into the simulation domain. To save the grids in simulation, the topography

is rotated counterclockwise by 28.28° as shown in Figure 3.2. In this figure, the dimensions of the calculation domain are in units of km .

3.2 Model Grid

Figure 3.3 shows the grids in the model domain (Whitney, 2003). This orthogonal curvilinear grid is generated by Gridpack grid generation software development at Rutgers University by Wilkin and Hedström (1998). The grids contain 150×300 cells covering the $240km \times 340km$ area. The variable cells are generated to optimize computing efficiency. The highest horizontal resolution is around $0.75km$ in the bay, while the lowest resolution is $8km$ offshore, which reduces grid number efficiently in calculation. The grid cell sizes are shown in Figure 3.4. Left panel shows the grid cell size in x -direction and right panel shows the grid cell size in y -direction. A degree of cell size variation has been introduced by the curvilinear grid generation (Whitney, 2003). The lower bay is covered by square cells $0.75km$ wide. The rest of the bay and river has $0.75km$ across-estuary resolution and $1.5km$ along-estuary resolution (Whitney, 2003).

3.3 Basic Input

Both the stationary and the nonstationary mode of SWAN are used in Delaware Bay cases. The physics includes quartet interactions, triad interactions, whitecapping, breaking and friction. The Komen et al. (1984) wave generation with exponential growth given by (2.13) is activated. For the whitecapping, the Cumulative Steepness Method (CSM) by Alkyon et al. (2002) is chosen. The semi-empirical expression derived from the JONSWAP model of Hasselmann et al. (1973) is chosen for bottom friction dissipation, i.e. $C_{bottom} = 0.038m^2s^{-3}$ for swell conditions and $C_{bottom} = 0.067m^2s^{-3}$ for wind sea conditions. The latter is the default value. A constant breaker parameter is used in depth-induced wave breaking simulation. The breaking parameter $\gamma = 0.73$.

The BSBT scheme is applied in the curvilinear grids in order to avoid losing accuracy due to the sharp transitions in the grids. The maximum number of iterations per time step for stationary mode is 15, and for nonstationary mode is changed to 5.

The spectral directions cover the full circle. The resolution in θ -space is 10° . The resolution in frequency-space is not constant. It is defined as:

$$\frac{\Delta f}{f} = \left(\frac{f_{high}}{f_{low}} \right)^{1/m} - 1 \quad (3.1)$$

in which f_{high} is the highest discrete frequency used in the calculation, f_{low} is the lowest discrete frequency, and m is one less than the number of frequencies. Due to the limitation of SWAN, the DIA approximation for the quartet wave-wave interactions asks for $\frac{\Delta f}{f} = 0.1$. Based on choosing $\frac{\Delta f}{f}$ a priori, m is then determined by:

$$m = \frac{\log(f_{high}/f_{low})}{\log(1 + \Delta f/f)} \quad (3.2)$$

3.4 Boundary Condition

In the present calculations with the bathymetry indicated in Figure 3.2, the lateral boundaries are far away from Delaware Bay where we are concerned. It is safe to set the spectra on these lateral boundaries to be zero. The deep water boundary is along the 100m isobath. The incoming wave components of these spectra are used in SWAN run. The default spectrum at the deep water boundary is the JONSWAP spectrum with $\gamma = 3.3$ and cosine power directional spreading. Based on the options in SWAN, TPAR files containing nonstationary wave parameters will be used at the deep water boundary. A TPAR file is only for one location. The time, significant wave height(H_s), average or peak period, peak direction should be provided in this file. These wave parameters are obtained from another full spectral third-generation wind-wave model WWIII. The wave data of significant wave height, peak period and peak direction simulated in Western North Atlantic model by WWIII

are downloaded from <ftp://polar.ncep.noaa.gov/pub/history/waves/>. The data are in the format of GRIB at three hour intervals, which can be read by the software of GrADS. The spatial resolution of WWIII is 0.25° . Four sites on the WWIII grids near $100m$ isobath are chosen shown in Figure 3.1 as black points. Then, we find the points nearest to them in the SWAN model domain along $100m$ isobath. The corresponding points are shown in Figure 3.2 as black squares A , B , C and D . The seaward boundary is divided into three segments, BD , DC and CA , by point C and D . The wave spectrum on the seaward boundary could be calculated by the wave parameters of these points. One way is to interpolate the two end points on the segment. Another way is to set the whole segment value equal to the one end point.

For example, Figure 3.5 shows the significant wave height at points A , B , C and D from WWIII from Oct. 21 to Oct. 29, 2003. Figure 3.6 and Figure 3.7 show the peak period and peak direction at the same period, respectively. The seaward boundary is divided into three segments by the points of C and D . On each segment, the wave parameters on the boundary are interpolated by the wave parameters at the end points. Figure 3.8 shows H_s distribution in model domain by setting wave parameters on the boundary. H_s , T_p and θ_p are obtained from Figure 3.5, Figure 3.6 and Figure 3.7 at 00:00 Oct. 21. H_s is smoothed on the boundary. Since the θ_p at this time is around 120° (CCW) and the upper boundary is set to be zero, Delaware Bay is in the shadow of the upper boundary.

3.5 Wind Data from Lighthouse

Fourteen Ft. Bank Lighthouse (Figure 3.9) is named for the 14 feet of water that cover this shoal bank. It is used as a platform for the Delaware Bay Observing System (DBOS).

DBOS has oceanographic and meteorological instrumentation to measure the dynamic coupling between the atmospheric and ocean variability in the bay. It is

used to statistically determine the transfer functions between wind speed, direction, sea level, and current profile. This will help in the development of nowcast and forecast models to determine the wind-induced sea level and current variability based on the integrated database. The skill of the statistical model can be evaluated based on the real-time observations from DBOS (DBOS Fourteen Ft. Bank Lighthouse Station website <http://www.udel.edu/dbos/system.htm>). The location of the DBOS (i.e. Fourteen Ft. Bank Lighthouse) is shown in Figure 3.10 as a red cross (Badiey et al., 2002).

The wind speed and direction measured on the lighthouse are adapted to construct the wind field for a SWAN run. The equipment records the wind speed in knots ($1knot = 0.51444m/s$) and wind direction in degrees counterclockwise (CCW) from North every 6 minutes. For example, a value of 45° means the wind is coming from the Northwest.

The wind is measured $18m$ above the mean sea surface. Since the wind speed specified at the standard elevation of $10m$ above the mean sea surface is needed in SWAN, it is necessary to adjust the wind speed from a given elevation to the standard elevation. Johnson (1999) found the $1/7$ power expression of SPM84 (U.S. Army Corps of Engineers, 1984) is identical (within $\pm 3\%$) to solving the logarithmic profile for $z \leq 20m$ as recommended in SPM84. The $1/7$ power expression is:

$$\frac{U_{10}}{U_z} = \left(\frac{10}{z}\right)^{1/7} \quad (3.3)$$

in which U_{10} is the wind speed $10m$ above the mean sea surface, z is the elevation where the wind speed is measured, U_z is the wind speed at the elevation of z m .

In the upper panel of Figure 3.11, the black line stands for the original wind speed from DBOS equipment during Oct.21 and Oct.29, 2003, which is recorded every $6min$. The red line is the wind speed averaged from every $6min$ to $1hr$. Being adjusted by Eq. (3.3), wind speed is reduced approximately by 8% shown as blue

line. The lower panel shows the original wind direction at every $6min$ (black line) and averaged direction for every $1hr$ (red line).

3.6 Currents

A simple case is presented here to show the influence of the current on the waves in SWAN. Suppose the wind of $10m/s$ blows up from west to east on the even bottom with $10m$ water depth. The fetch is $20km$ in west-east direction. The spacing resolution is uniform in both directions with a spacing of $200m$. SWAN is run in the stationary mode. The solid line shown in Figure 3.12 is the significant wave height (H_s) along x -axis from west to east calculated without currents. It is increasing gradually in space within the fetch region. Next, the windward and leeward current effects on H_s are shown. The windward current of $0.5m/s$ increases H_s (dash line). The leeward current of $0.5m/s$ decreases H_s (dot line). The opposing current increases relative wind velocity and steepens waves, while the following current decreases relative wind velocity and reduces the wave steepness. This effects get larger with increasing current in each direction by comparing $1.0m/s$ leeward current (cross line) and $0.5m/s$ leeward current (dot line), and comparing $1.0m/s$ windward current (dot-dash line) and $0.5m/s$ windward current (dash line).

Some complicated real-time current fields in Delaware Bay and adjacent ocean region will be simulated by the Regional Ocean Model System (ROMS) in the next chapter. They will be applied in SWAN simulation.

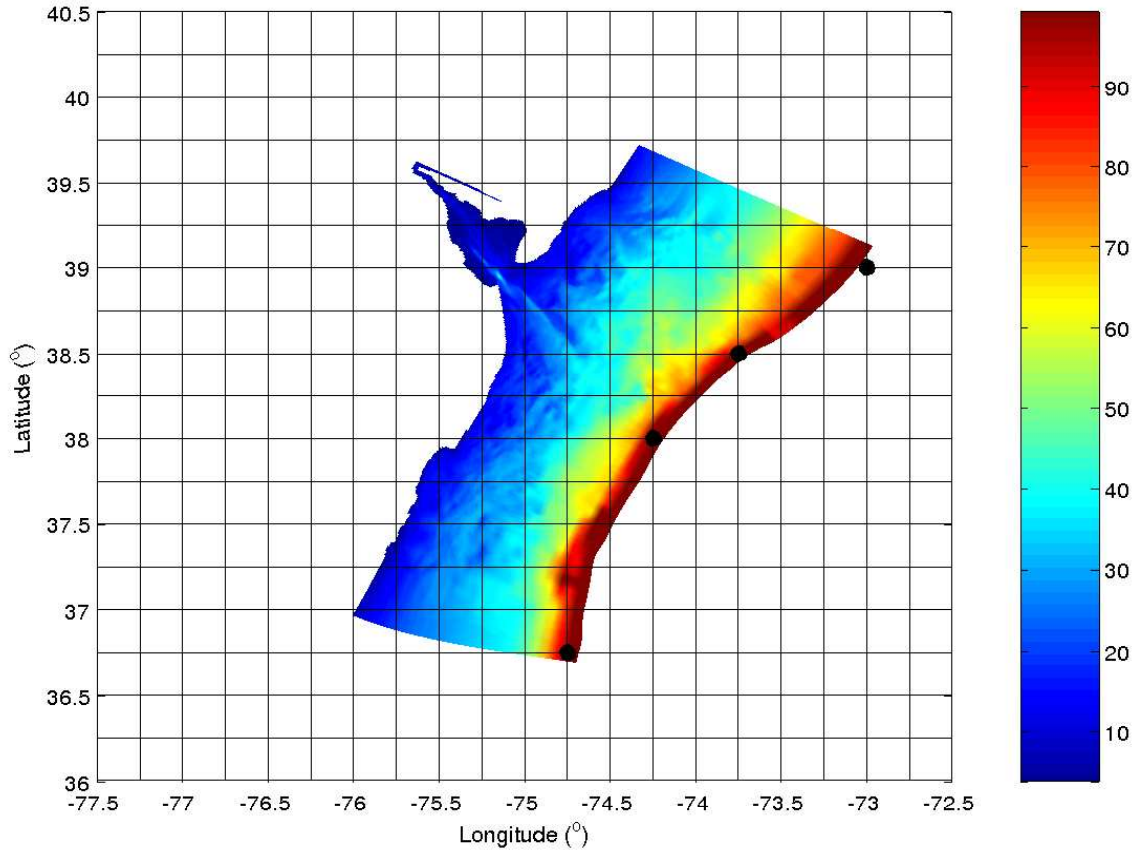


Figure 3.1: Bathymetry in simulation. The large scale mesh represents the grid system used in WWIII model around the area of SWAN model domain. The wave parameters calculated by WWIII are chosen at the black points which are set at the seaward boundary (approximately along 100m isobath) in SWAN simulation. (Unit in color bar is *m*)

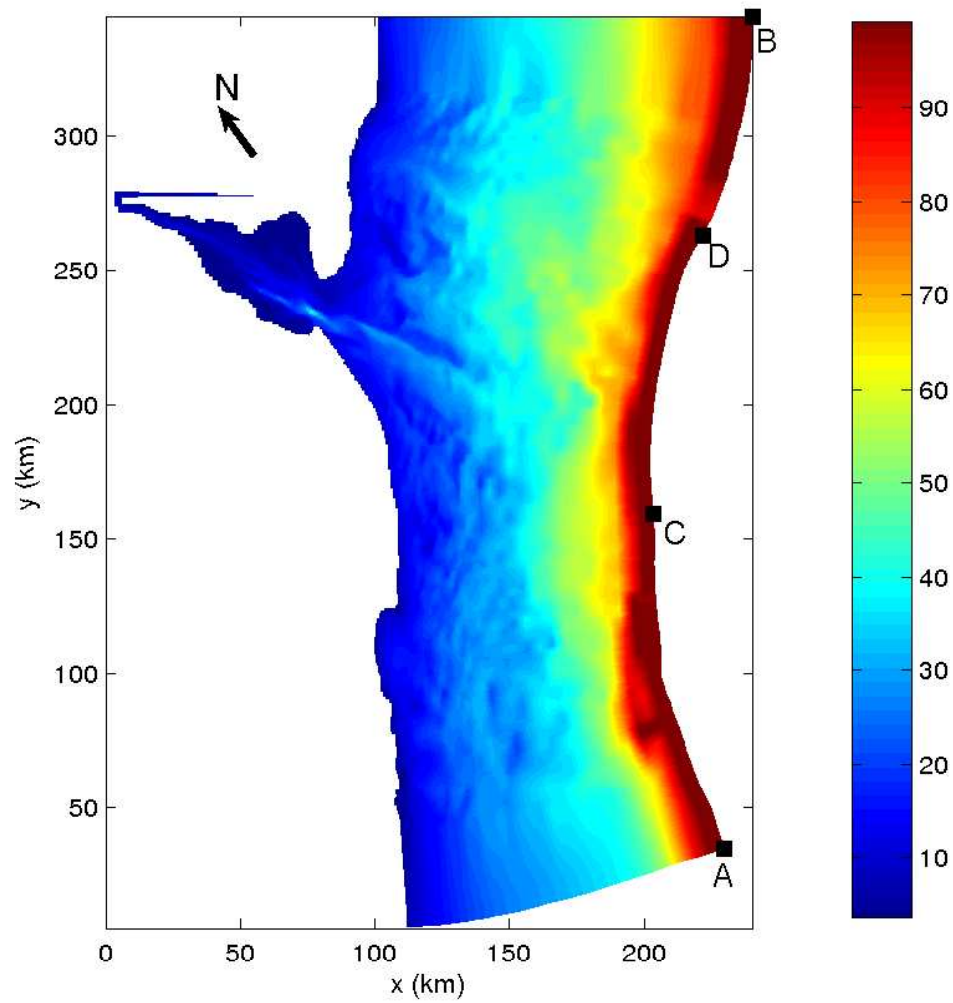


Figure 3.2: Bathymetry in the simulation coordination. Black squares *A*, *B*, *C* and *D* are the points nearest to the black points in Figure 3.1 along 100m isobath. (Unit in color bar is *m*)

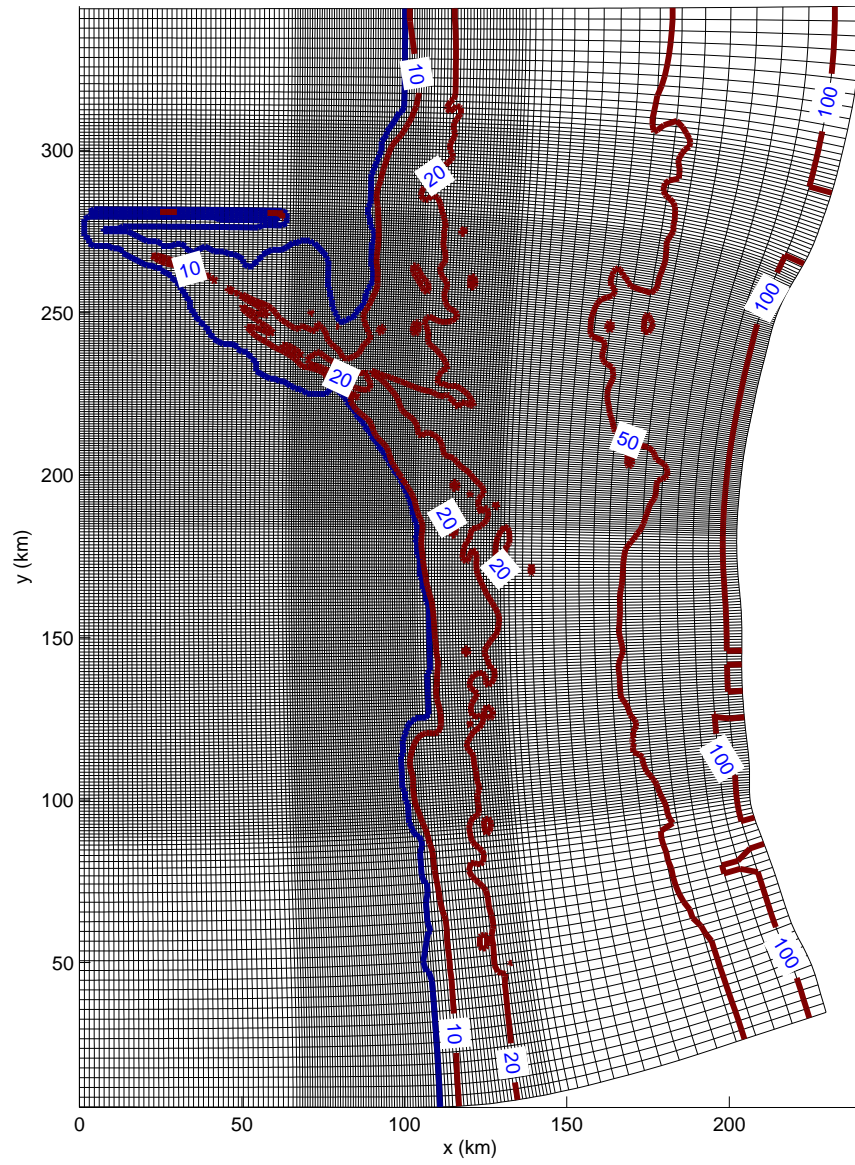


Figure 3.3: Grid cells in the model domain with 0m (blue line), 10m, 20m, 50m, 100m (red lines) isobaths

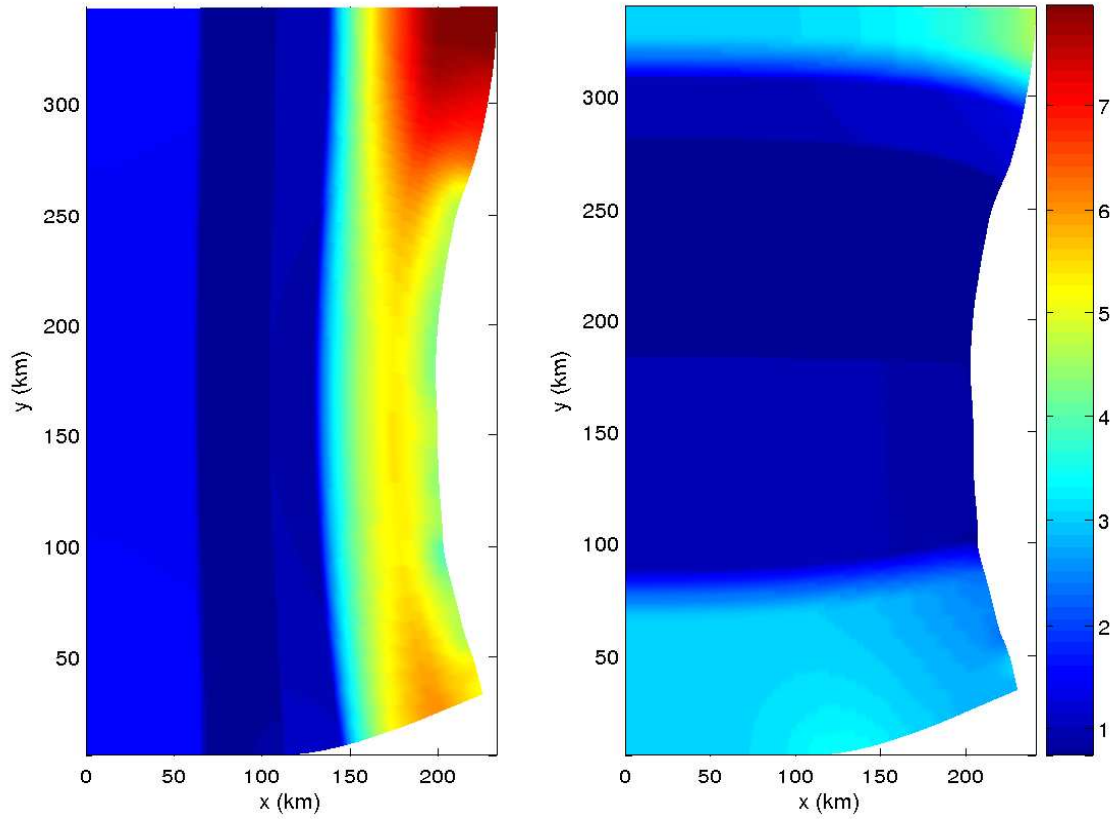


Figure 3.4: Grid cell size in x -direction (left panel) and y -direction (right panel)
(Unit in color bar is km)

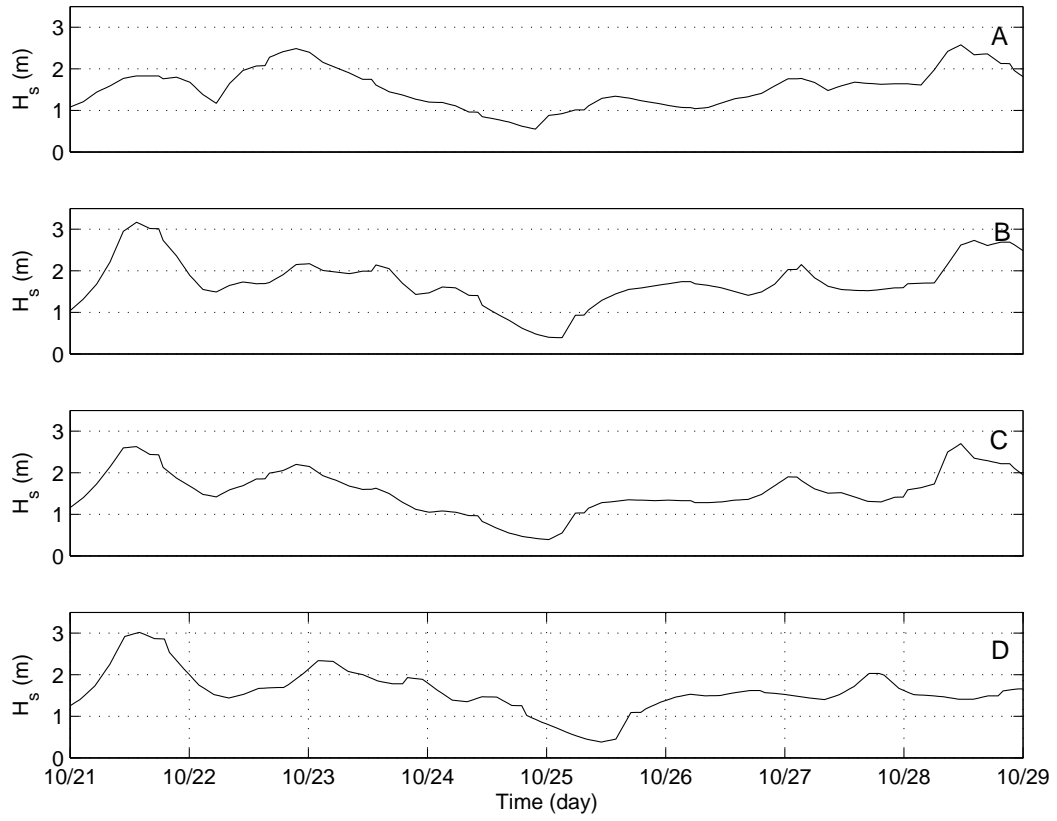


Figure 3.5: Significant wave height at points *A*, *B*, *C* and *D* at seaward boundary from WWIII in 2003

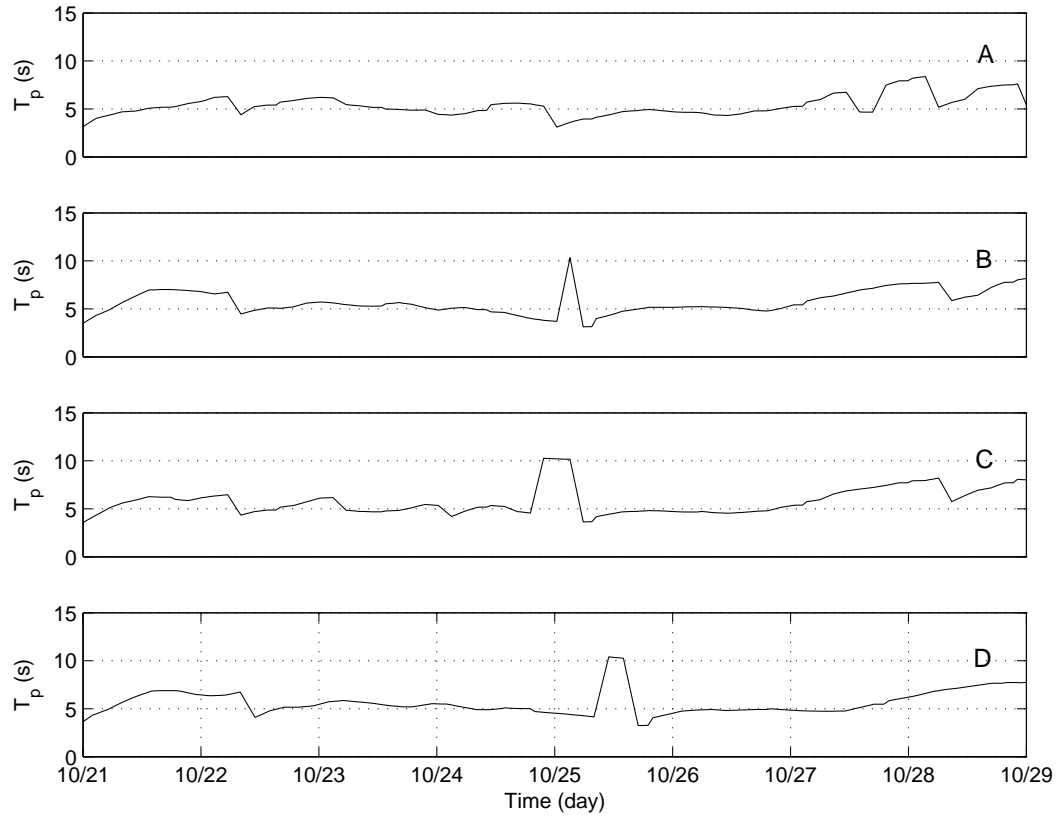


Figure 3.6: Peak period at points *A*, *B*, *C* and *D* at seaward boundary from WWIII in 2003

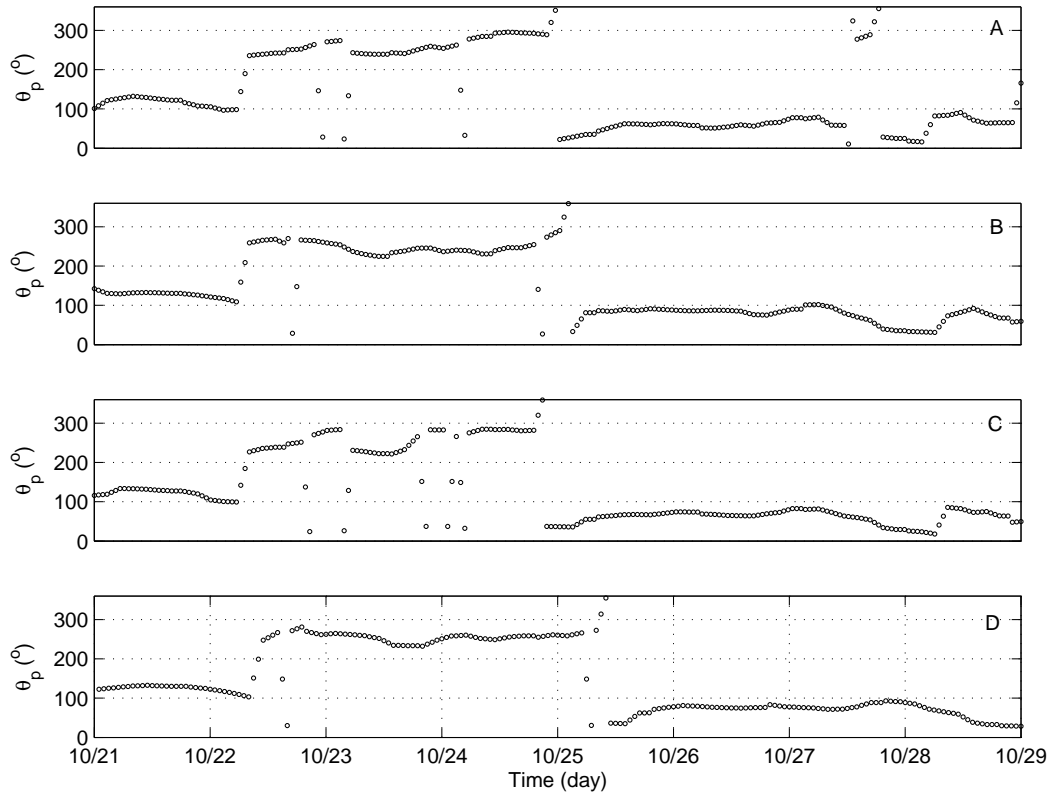


Figure 3.7: Peak direction (CCW) at points *A*, *B*, *C* and *D* at seaward boundary from WWIII in 2003

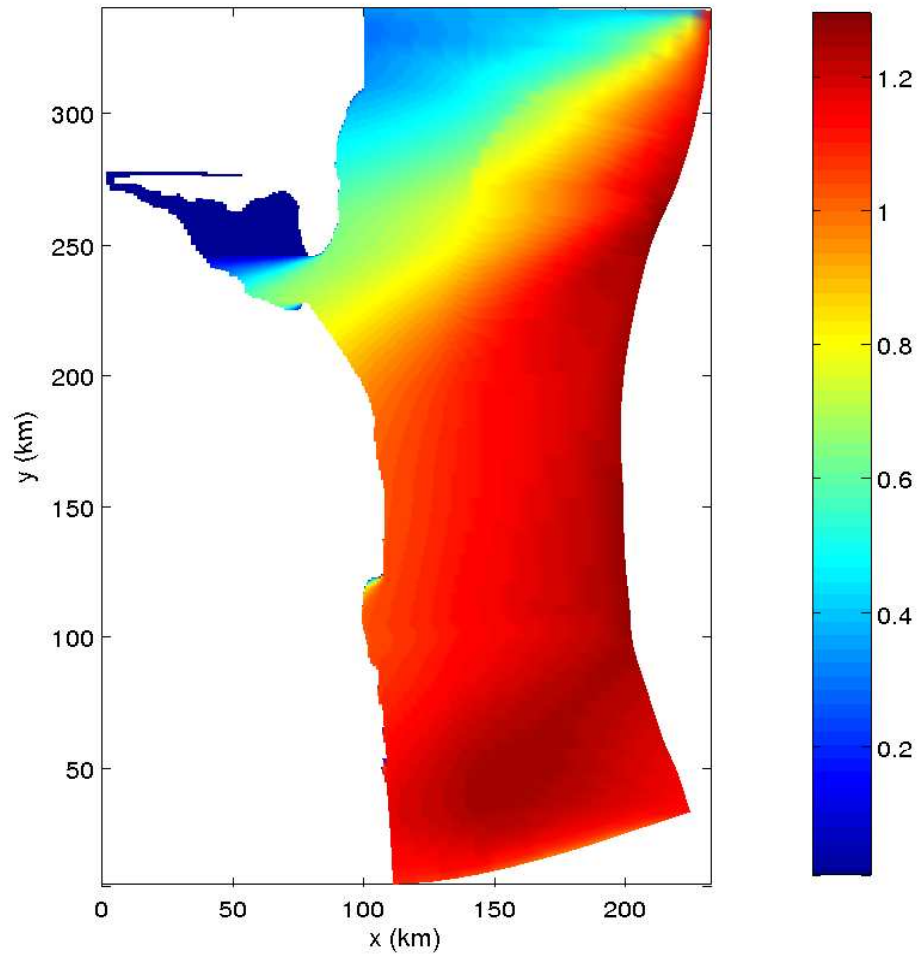


Figure 3.8: H_s distribution driven by boundary condition from WWIII at 00:00 Oct. 21, in 2003



Figure 3.9: Fourteen Ft. Bank Lighthouse in Delaware Bay



Figure 3.10: Location of DBOS on Fourteen Ft. Bank Lighthouse (Red cross, $75^{\circ}11'W, 39^{\circ}01'N$) in Delaware Bay (Badiey et al., 2002)

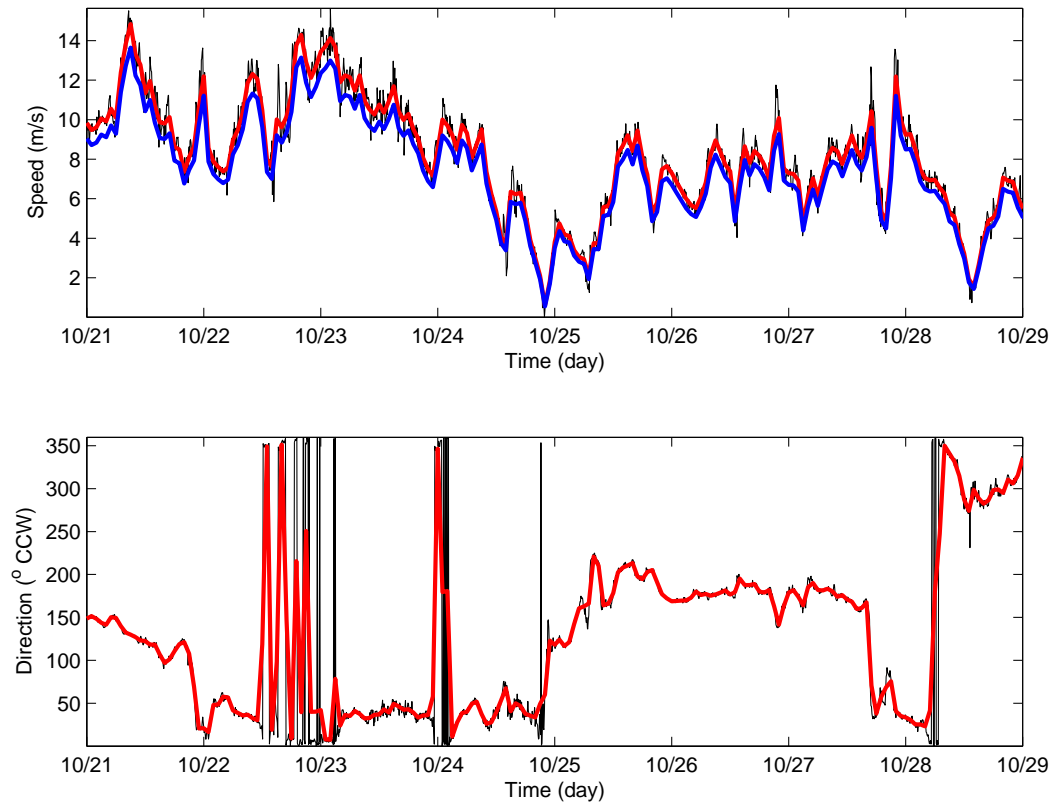


Figure 3.11: Wind speed and direction from Fourteen Ft. Bank Lighthouse in 2003. In the upper panel, the black line is the wind speed from DBOS record for every $6min$, the red line is the averaged wind speed for every $1hr$, the blue line is the adjusted wind speed from $18m$ to $10m$ above the sea surface. In the lower panel, the black line is the wind direction from DBOS record for every $6min$, the red line is the averaged wind direction for every $1hr$

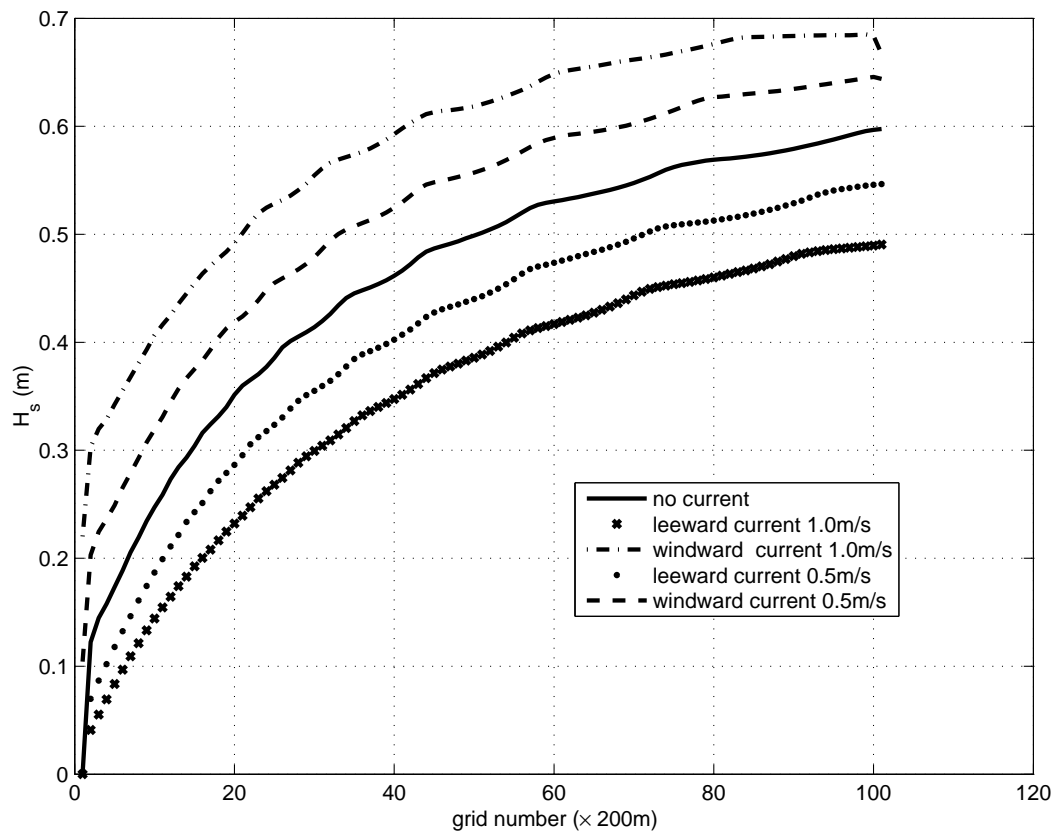


Figure 3.12: Significant wave height along wind blowing up direction with different uniform currents on even bottom with 10m water depth

Chapter 4

MODEL SENSITIVITY

SWAN is sensitive to the input parameters, such as wind growth model, tidal current, boundary condition and dissipation. Gorman and Neilson (1999) have shown that SWAN is sensitive to spatial variability in wind conditions even on the scale of a small enclosed estuary or embayment. In this chapter, the spatially interpolated wind field will be used in the SWAN, which will be compared to the spatially constant wind field. Additionally, the influence of tidal currents is considered in SWAN by coupling Regional Ocean Modeling System (ROMS).

4.1 Spatially Interpolated Wind

The Physical Oceanographic Real-Time System (PORTS) is a program of the National Ocean Service that supports safe and cost-efficient navigation by providing ship masters and pilots with accurate real-time information required to avoid groundings and collisions. The PORTS database has data since 2000, including air temperature, barometric pressure, salinity, water current, water level, water temperature and winds. There are several stations distributed in Delaware Bay. Among them, the stations of Delaware City, Ship John Shoal Light, Brandywine Shoals Light and Lewes are chosen in this study (Red points in Figure 4.1). Additionally, the wind speed and direction of National Data Buoy Center (NDBC) buoy station 44009 (hereafter NDBC 44009) are obtained on the website of http://www.ndbc.noaa.gov/station_page.php?station=44009. NDBC 44009 is located southeast of Cape May, NJ, at $38^{\circ}27.6'N$, $74^{\circ}42'W$, which is near the $28.0m$ isobath. The anemometer

height is $5m$ above the site elevation. Lewes is at $38^{\circ}46.9'N$, $75^{\circ}7.2'W$. Brandywine Shoals Light is at $38^{\circ}59.2'N$, $75^{\circ}6.8'W$. Ship John Shoal Light is at $39^{\circ}18.3'N$, $75^{\circ}22.5'W$. Delaware City is at $39^{\circ}34.9'N$, $75^{\circ}35.3'W$.

In Figure 4.2, wind speed and direction measured at six different stations throughout Delaware Bay during October 27 through 29, 2003 are presented. All of the wind speeds are converted to the speed at $10m$ above the surface elevation. As the upper panel of Figure 4.2 shows, the wind speed at Delaware City is weaker than other stations, because it is near the northern end of the bay and wind was measured on land. The wind speed measured at Lewes is small too when the wind blows from south to north on October 27. The wind speed and direction are very close at the Brandywine Shoals Light (magenta diamond), Ship John Shoal Light (red diamond) and Fourteen Ft. Bank Lighthouse (blue circle), which are in mid Bay. The wind information from NDBC 44009 were not available at some time intervals, such as during 9am through 12pm on October 29, and is replaced by a linear interpolation. If we neglect the missing information in the measured data, most of the wind direction data have similar trends throughout the whole bay in the lower panel of Figure 4.2.

In this model domain, there is no wind information at the offshore boundary along the $100m$ isobath. The wind information measured at NDBC 44009 is used at this boundary. Other stations, Fourteen Ft. Bank Lighthouse and Delaware City, are chosen to construct the spatially variable wind by interpolating these three value along the x -direction. The wind is assumed to be uniform in the y -direction. Several cases were picked to examine the effect of the wind field distribution. Table 4.1 lists the wind speed and direction of these stations at some times. The direction is counterclockwise (CCW) to the true north. While the wind vectors shown in the following figures are relative to the y -axis of the frame coordinate. In this study, this y -axis deviates -28.28° from true north in counterclockwise.

Table 4.1: Wind speed and direction at three stations

	Delaware City		Lighthouse		NOAA buoy	
	speed(<i>m/s</i>)	dir($^{\circ}$)	speed(<i>m/s</i>)	dir($^{\circ}$)	speed(<i>m/s</i>)	dir($^{\circ}$)
13:00 Oct. 27	1.879	210	7.969	176	6.9558	184
20:00 Oct. 27	4.179	86	8.022	169	11.262	179
03:00 Oct. 28	3.013	60	9.189	36	12.035	38
00:00 Oct. 29	2.041	289	6.712	295	9.385	299
12:00 Oct. 29	3.985	65	10.138	49	14.353	67

First, the wind speed and direction at 13:00 October 27, 2003 is chosen. The wind vectors of Delaware City, Fourteen Ft. Bank Lighthouse and NDBC 44009 from left to right are shown in the right panel of Figure 4.3. The lower arrow in this panel is a reference vector. All of the wind directions are approximately from south to north. The wind speed at Delaware City is much smaller than the other two. The wind speed at NDBC 44009 is slightly smaller than the one at Fourteen Ft. Bank Lighthouse. Blue arrows in Figure 4.3 display a spatially uniform wind field based on values at Fourteen Ft. Bank Lighthouse. We interpolate the wind speeds and directions at three stations along x -direction as black arrows in the left panel of Figure 4.3. Thus the wind speed is smaller on both sides of the lighthouse in a spatially variable wind field than in a uniform wind field. Significant wave height (H_s) in the upper bay and Atlantic ocean shelf are smaller in the right panel of Figure 4.4 simulated by variable wind field than the ones shown in left panel simulated by uniform wind field. The % difference is shown in Figure 4.5. The effect of the wind variations ranges between 0% – 10% in the middle of the bay. As for the peak period (T_p) shown in Figure 4.6, there is not much difference both in the bay and on the ocean shelf, which is verified by the difference shown in Figure 4.7. H_s and T_p at the measuring station near Fourteen Ft. Bank Lighthouse are almost same for different wind fields (Figure 4.8) at 13:00 October 27. The blue circle is

the value calculated from uniform wind field and the red cross is from variable wind field. The black circle is the measured data by WSB.

Next, the wind speed and direction at 20:00 October 27, 2003 is chosen. In this case, the wind direction at Fourteen Ft. Bank Lighthouse and NOAA buoy station are almost the same as before, while the wind direction at Delaware City turns to west-east. After interpolating, the wind field distribution is much different from the uniform one between the area of Delaware City and Fourteen Ft. Bank Lighthouse, which causes a difference of H_s distribution in the upper bay. The wind speed at NDBC 44009 is larger than the one at Fourteen Ft. Bank Lighthouse, so the wind speed is larger at ocean shelf for variable wind field. It makes H_s increase at the ocean shelf. The % difference of the two in Figure 4.10 is shown in Figure 4.11. Again, there is not much change in the middle of the bay. The peak period (T_p), shown in Figure 4.12, is not much effected in the bay, but increases significantly on the ocean shelf. The % difference is shown in Figure 4.13. In Figure 4.8, both of H_s are over-predicted in comparison to the measured date. T_p 's are equal although wind distribution changes. Also T_p 's are underestimated over 30%.

Wind speeds and directions at 03:00 October 28, 2003 at three stations are shown in the right panel of Figure 4.14. The uniform and variable wind fields are shown in the left panel as blue arrows and black arrows, respectively. The wind blows offshore this time. It is clearly shown in Figure 4.15 that the H_s in the upper bay is smaller with variable wind field than with the uniform one. The difference is shown in Figure 4.16. As for the peak period (T_p) shown in Figure 4.17, there is a small decrease in the bay and a small increase on the ocean shelf. The percentage of the change is shown in Figure 4.18. In this case, compare to the measured date, variable wind field agrees better in H_s , while uniform wind field does in T_p in Figure 4.8.

Another time of 00:00 October 29, 2003 is chosen because the wind blows

from the north-east in the model domain. The interpolation decreases the wind speed in the upper bay and increases it on the ocean shelf (Figure 4.19). Figure 4.20 shows that H_s is increased on the ocean shelf, and is decreased a little in the upper bay. According to Figure 4.21, there is not much change in the middle of the bay, which is consistent with the H_s shown in the upper panel of Figure 4.8. As for the peak period (T_p) shown in Figure 4.22, there is a small increase nearshore in the mid bay and on the ocean shelf. The % difference is shown in Figure 4.23. Look at the lower panel of Figure 4.8, T_p at the measuring station is not effected by the change of the wind distribution at the measuring station, but is overestimated in the simulation.

Finally, the time of 12:00 October 29, 2003 is chosen. The wind blows approximately from north-west to south-east (Figure 4.24). The H_s at the upper bay is decreased due to the interpolation of wind field, and is increased on the ocean shelf, which is more clearly shown in Figure 4.26. At the measuring station, the H_s is closer to the measured data with variable wind field than the one with uniform wind field in the upper panel of Figure 4.8. As for the peak period (T_p) shown in Figure 4.27, the variable wind field makes the T_p decreases in the bay, but increases on the ocean shelf. The % difference is shown in Figure 4.28. The T_p at the measuring station deviates more away from the measured data shown in the lower panel of Figure 4.8.

4.2 Influence of Tidal Currents

In some coastal areas, the hydrodynamic conditions involving wave-current interaction are extremely complex. Strong tidal currents affect wave transformation. Normally, tidal and wind-driven circulation and wind wave generation and transformation are modeled in separate process models. The independent modeling of wave transformation and circulation can not predict the complicated coastal process very well in lack of considering the interaction between the two processes. In order to

take into account the interaction between the waves and currents, the coupling of ROMS and SWAN models is developed.

4.2.1 Shelf Circulation Model ROMS

The Regional Ocean Model System (ROMS) is a three-dimensional numerical ocean model, which simulates currents, ecosystems, biogeochemical cycles and sediment movement in various coastal regions. ROMS solves the primitive equations in an Earth-centered rotating environment with the Boussinesq approximation and hydrostatic vertical momentum balance. It uses stretched, terrain-following coordinates in the vertical and orthogonal curvilinear coordinates in the horizontal. Initially, the S-coordinate Rutgers University Model (SCRUM) was developed by Song and Haidvogel (1994). Later, ROMS was completely rewritten to include high-order advection schemes, accurate pressure gradient algorithms, several subgrid-scale parameterizations, atmospheric, oceanic, and benthic boundary layers, biological modules, radiation boundary conditions and data assimilation (Shchepetkin and McWilliams, 2005).

In the model domain of Delaware Bay and its adjacent ocean region, ROMS is driven by M2, N2, S2, K2, O1, K1 and Q1 tides at the offshore boundary (Personal communication with Long Xu). The solid line in Figure 4.29 shows water depth-averaged tidal current velocities calculated by ROMS in east-west and north-south components at the measuring station during October 27 through October 29, 2003, which is compared to the measured data from ADCP (circles). The simulated results agree well with the measured data except a little overestimation in east-west component. Since the M2 tide dominates in this process, the period of the current velocity is about twelve hours.

4.2.2 Coupling the Model Systems

In this study, the traditional file *I/O* method is used to couple ROMS and SWAN. First, ROMS is driven by the tide at the offshore boundary. The water depth-averaged current velocities calculated by ROMS are stored in files for the desired periods, which are used as input files for SWAN.

The tidal current at 20:00 October 27 in the whole model domain is shown in the right panel of Figure 4.30. This current field is applied to SWAN simulation. The left panel of Figure 4.30 is the spatially variable wind field at this time. Figure 4.31 shows the H_s with (right panel) and without (left panel) currents based on this wind field. Since the current is very small on the ocean shelf, it does not affect H_s much. In the upper bay, current and wind are almost perpendicular each other, so there is not much change due to the current. In the middle of the bay, the current has the similar direction as wind, which makes the H_s decrease in the bay. The % difference in Figure 4.32 also shows this trend. The T_p distributions in the model domain with and without current field are presented in Figure 4.33. According to the % difference shown in Figure 4.34, the current affects the T_p much near shore. In Figure 4.35, blue diamond stands for the results with tidal current field on spatially variable wind field, and the red cross stands for the ones without current field. The data measured by waverider buoy at the measuring station is represented by black circle. Both of the H_s and T_p decrease due to the current. H_s with current is closer to the measurement, but T_p deviates more.

Another current field at 03:00 October 28 is presented at the right panel of Figure 4.36. The current is still small on the ocean shelf. At the mouth of the bay, the current is bigger and opposite to wind, which increases H_s . In the upper and middle of the bay, the current has the same direction as the wind, which makes H_s decrease. The details of the change of H_s between the left panel and right panel in Figure 4.37 is shown in Figure 4.38. As for the results of T_p , the distributions

are presented in Figure 4.39 and the % difference is shown in Figure 4.40. As for the measuring station in Figure 4.35, H_s does not change and matches well with the measurement. While the T_p with current deviates more than the one without current.

Finally, the current field at 00:00 October 29 is chosen in the right panel of Figure 4.41. Most of the currents are offshore. Again, the currents on ocean shelf are too small to affect the wind-generated waves much. In Figure 4.43, the % difference of the two distributions in Figure 4.42 shows H_s increases much in the middle and the mouth of the bay due to the current existence. T_p only changes a little on the boundary in the middle of the bay as shown in Figure 4.44 and Figure 4.45. These trends are also shown in Figure 4.35.

4.3 Conclusion

SWAN simulation is sensitive to the wind field distribution. However, for the particular measurement location at Fourteen Ft. Bank Lighthouse, the difference between uniform and variable wind fields does not change H_s and T_p significantly, because wind field in the mid of the bay does not change as much as it does in the upper bay and ocean shelf after interpolation.

Since the current on the ocean shelf is small, it almost does not affect H_s and T_p . While in the bay, the current affects the wave propagation, especially in the upper bay and the mouth of the bay.

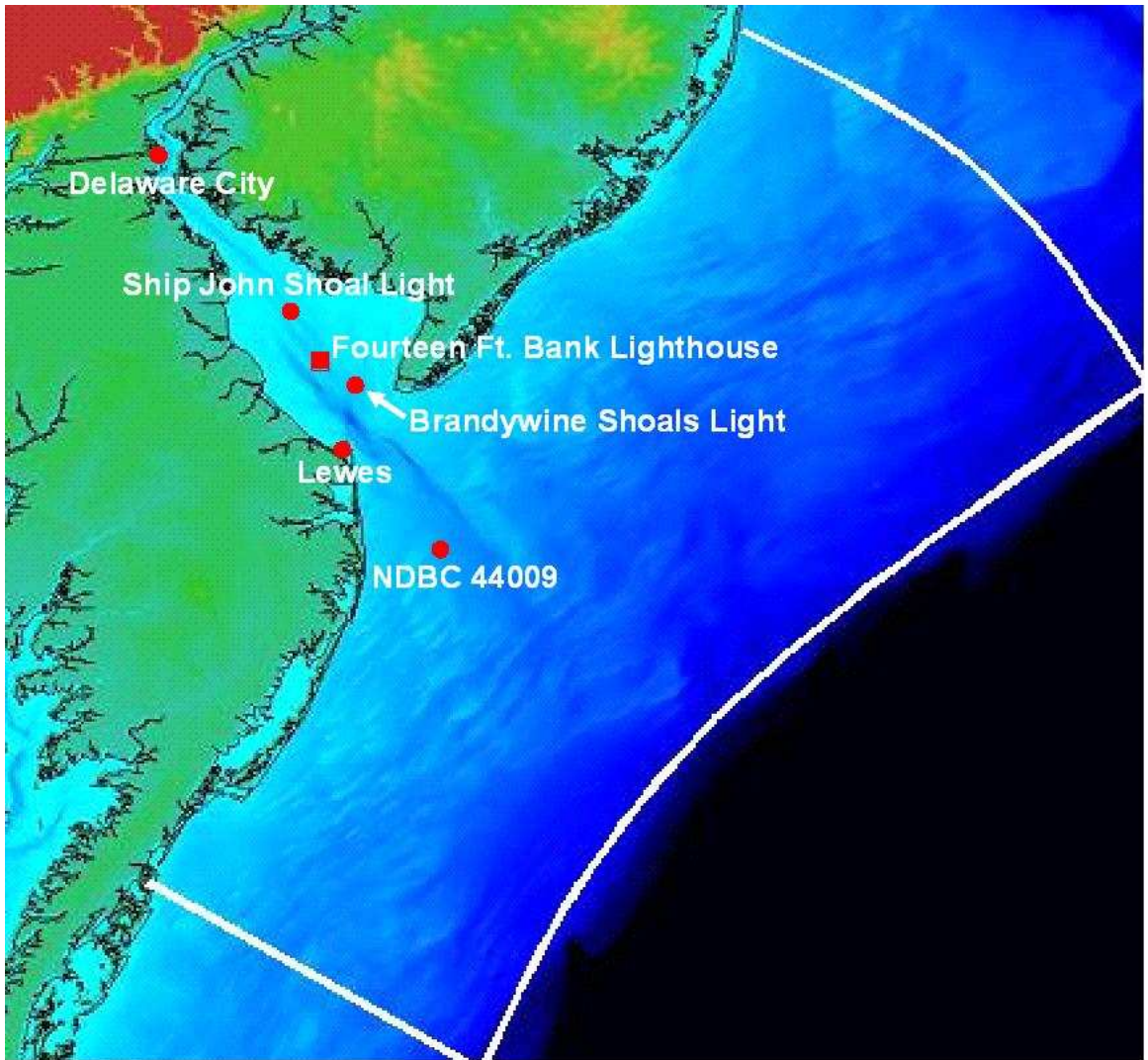


Figure 4.1: PORTS Stations and NDBC 44009 (red circle), Fourteen Ft. Bank Lighthouse (red square) in Delaware Bay (Whitney, 2003)

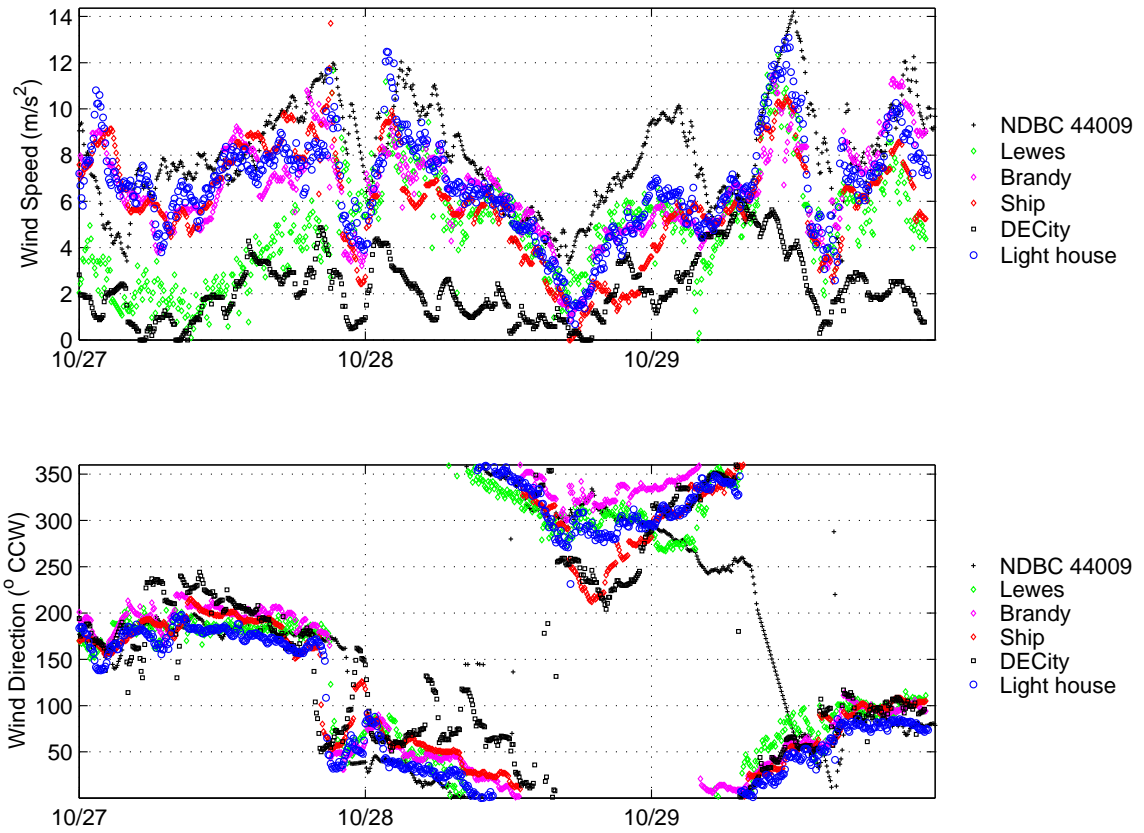


Figure 4.2: Wind speed and direction (CCW) measured at different stations during October 27 through 29, 2003. Black filled diamond: NDBC 44009; Green diamond: Lewes; Magenta diamond: Brandywine Shoals Light; Red diamond: Ship John Shoal Light; Black square: Delaware City; Blue circle: Fourteen Foot Bank Lighthouse

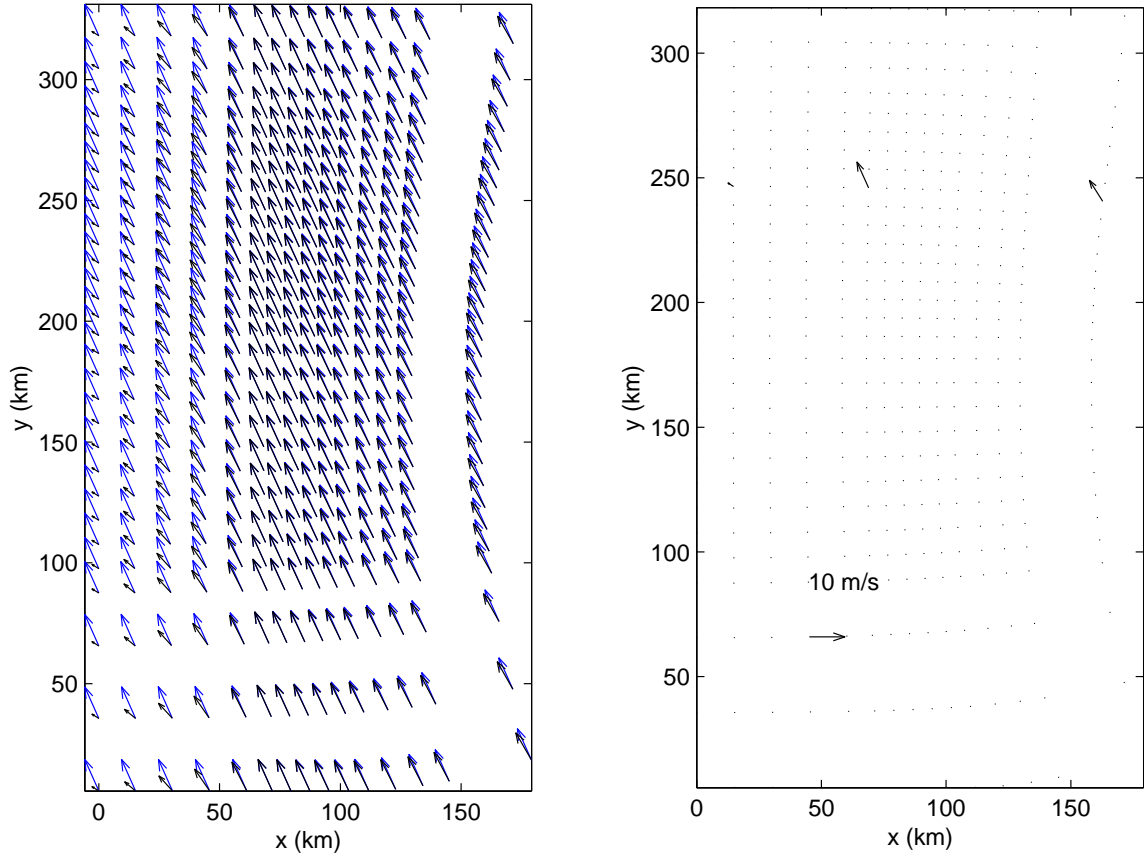


Figure 4.3: Spatially constant wind field (blue arrow) and interpolated wind field (black arrow) in model domain in the left panel; Right panel shows the three wind vectors used in interpolation and a reference vector at 13:00 October 27, 2003

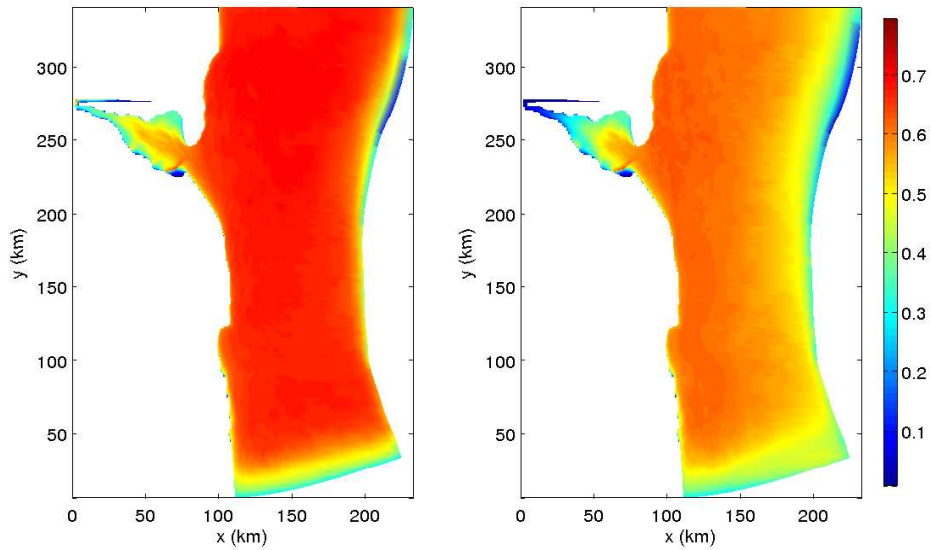


Figure 4.4: Significant wave height with spatially constant wind field (left panel) and interpolated wind field (right panel) in model domain at 13:00 October 27, 2003 (Unit in color bar is m)

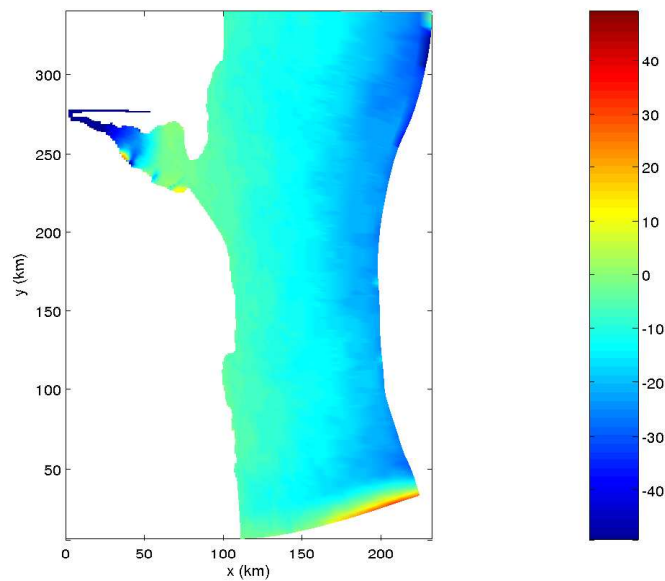


Figure 4.5: Difference of significant wave height with spatially constant wind field and interpolated wind field in model domain at 13:00 October 27, 2003 (Unit in color bar is percentage)

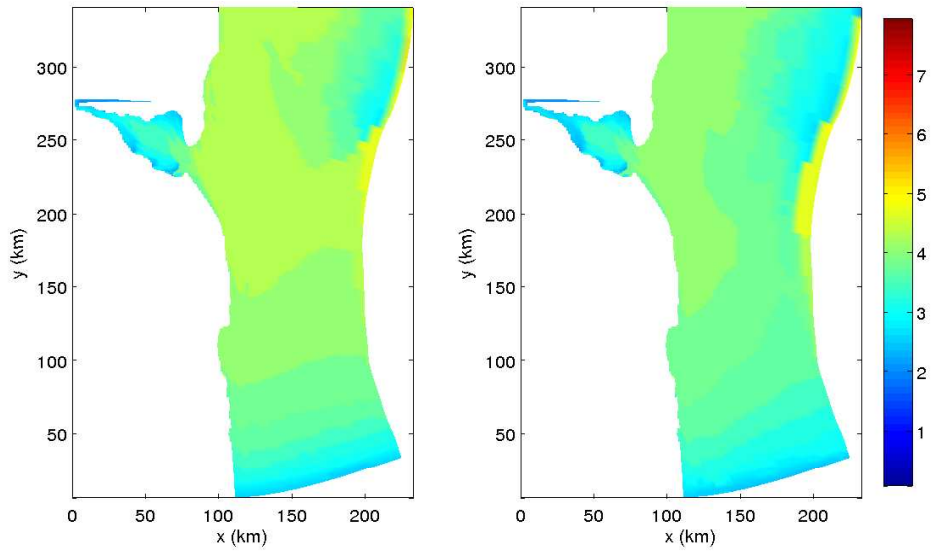


Figure 4.6: Peak period with spatially constant wind field (left panel) and interpolated wind field (right panel) in model domain at 13:00 October 27, 2003 (Unit in color bar is s)

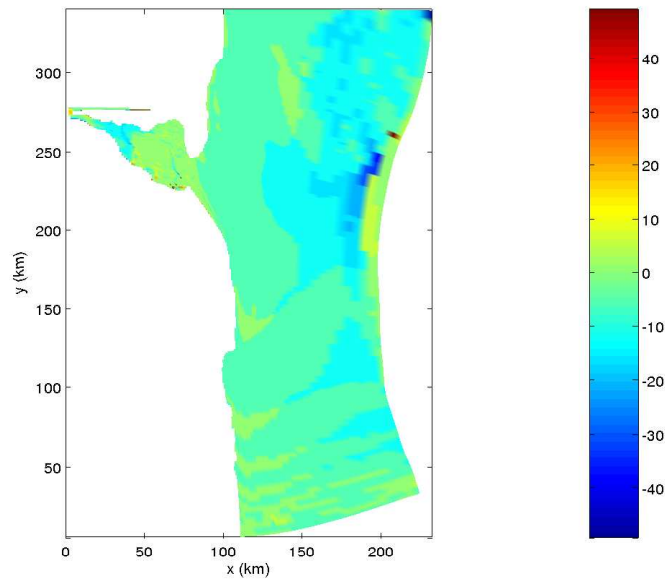


Figure 4.7: Difference of peak period with spatially constant wind field and interpolated wind field in model domain at 13:00 October 27, 2003 (Unit in color bar is percentage)

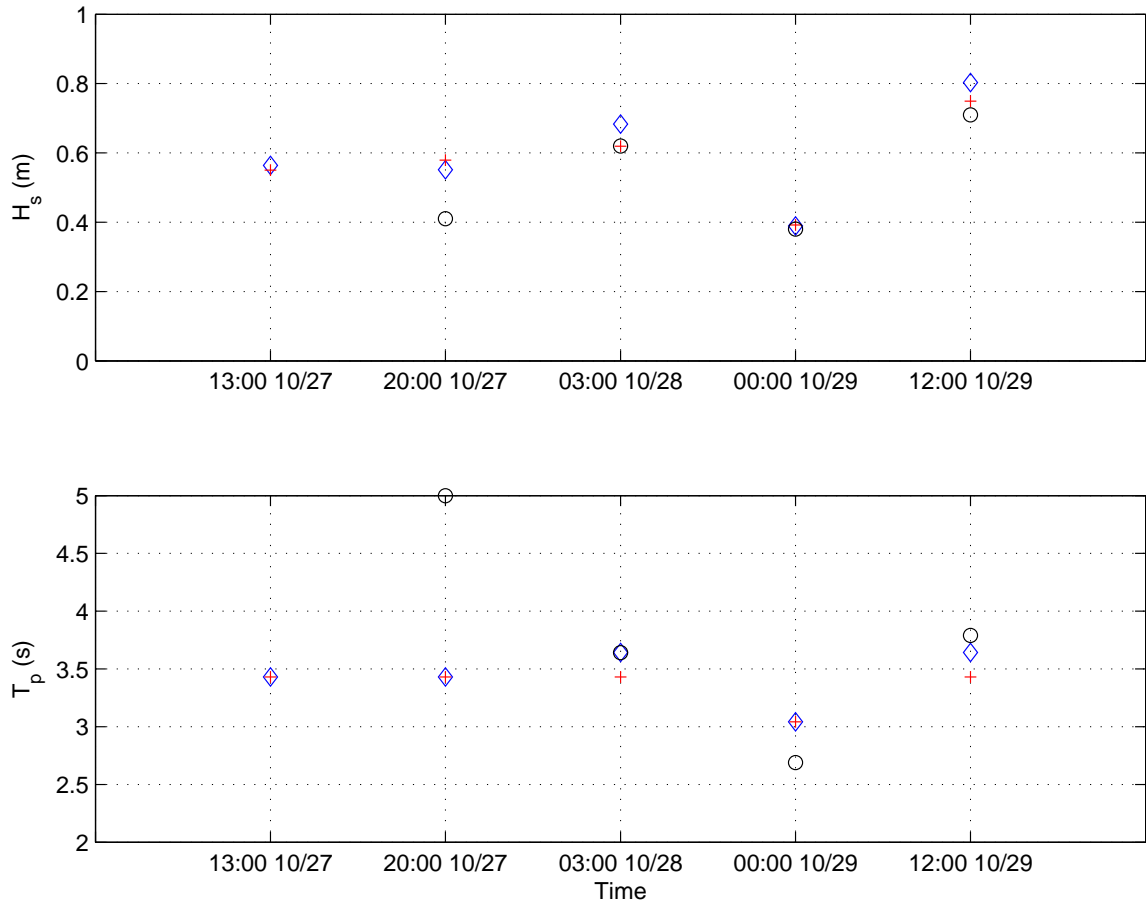


Figure 4.8: Comparison of Significant wave height (H_s), Peak period (T_p) near Fourteen Ft. Bank Lighthouse between spatially constant wind field (blue diamond), interpolated wind field (red cross) and measured by WSB (black circle) at some time in 2003

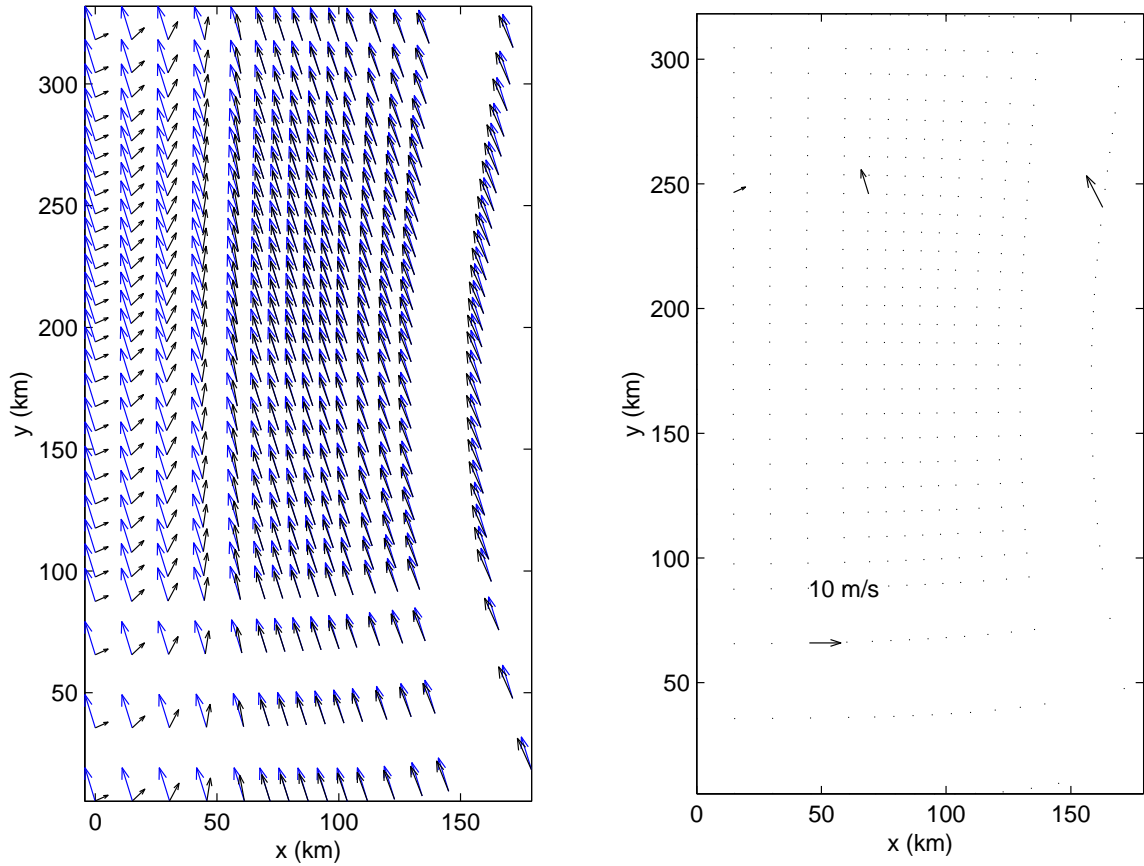


Figure 4.9: Spatially constant wind field (blue arrow) and interpolated wind field (black arrow) in model domain in the left panel; Right panel shows the three wind vectors used in interpolation and a reference vector at 20:00 October 27, 2003

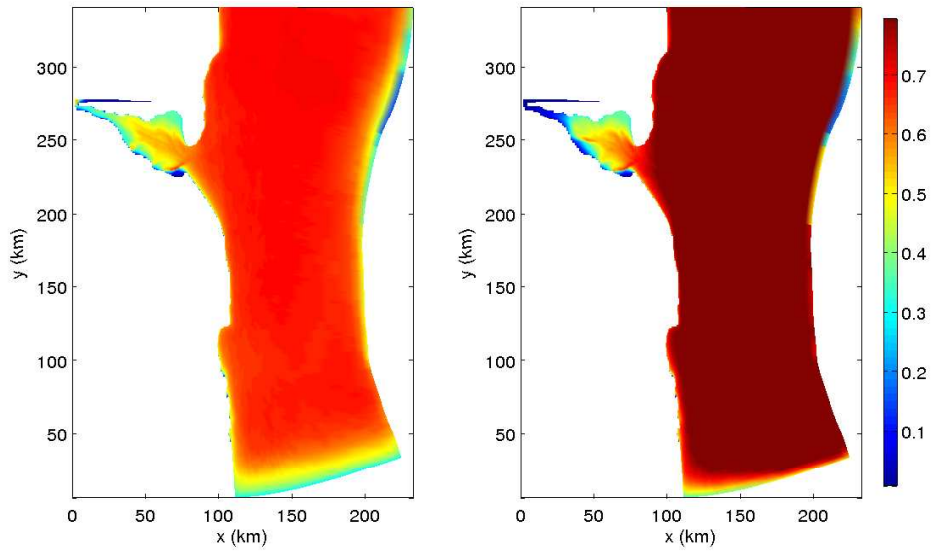


Figure 4.10: Significant wave height with spatially constant wind field (left panel) and interpolated wind field (right panel) in model domain at 20:00 October 27, 2003 (Unit in color bar is m)

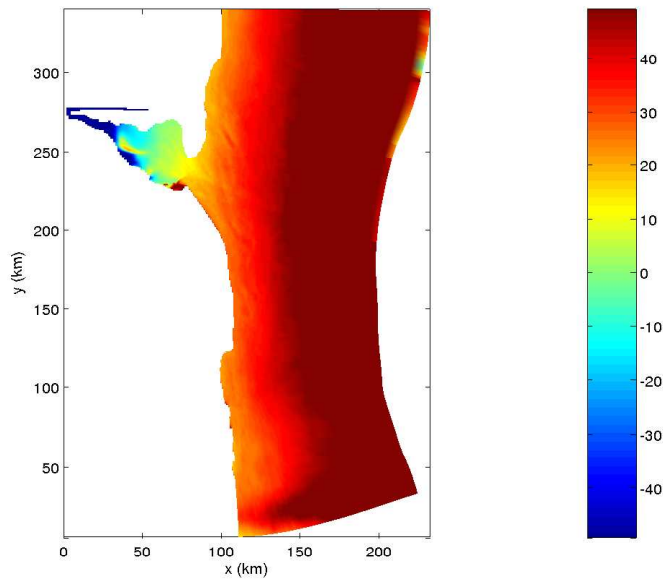


Figure 4.11: Difference of significant wave height with spatially constant wind field and interpolated wind field in model domain at 20:00 October 27, 2003 (Unit in color bar is percentage)

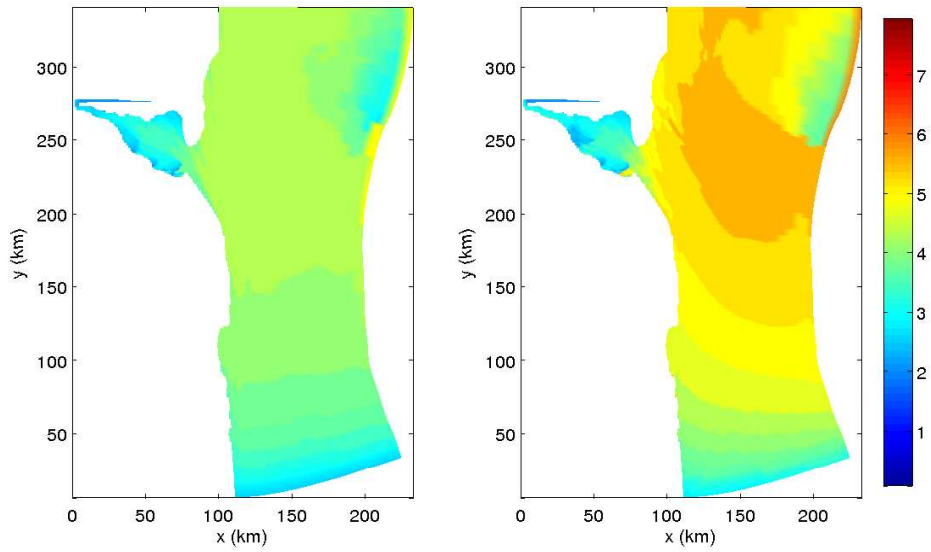


Figure 4.12: Peak period with spatially constant wind field (left panel) and interpolated wind field (right panel) in model domain at 20:00 October 27, 2003 (Unit in color bar is s)

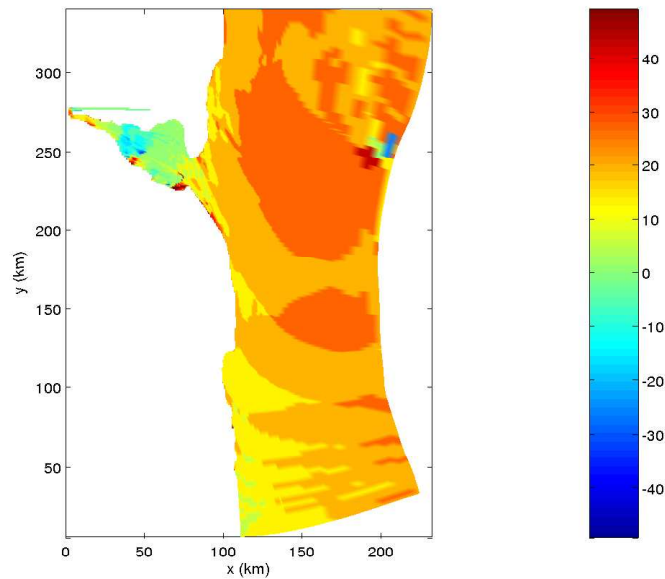


Figure 4.13: Difference of peak period with spatially constant wind field and interpolated wind field in model domain at 20:00 October 27, 2003 (Unit in color bar is percentage)

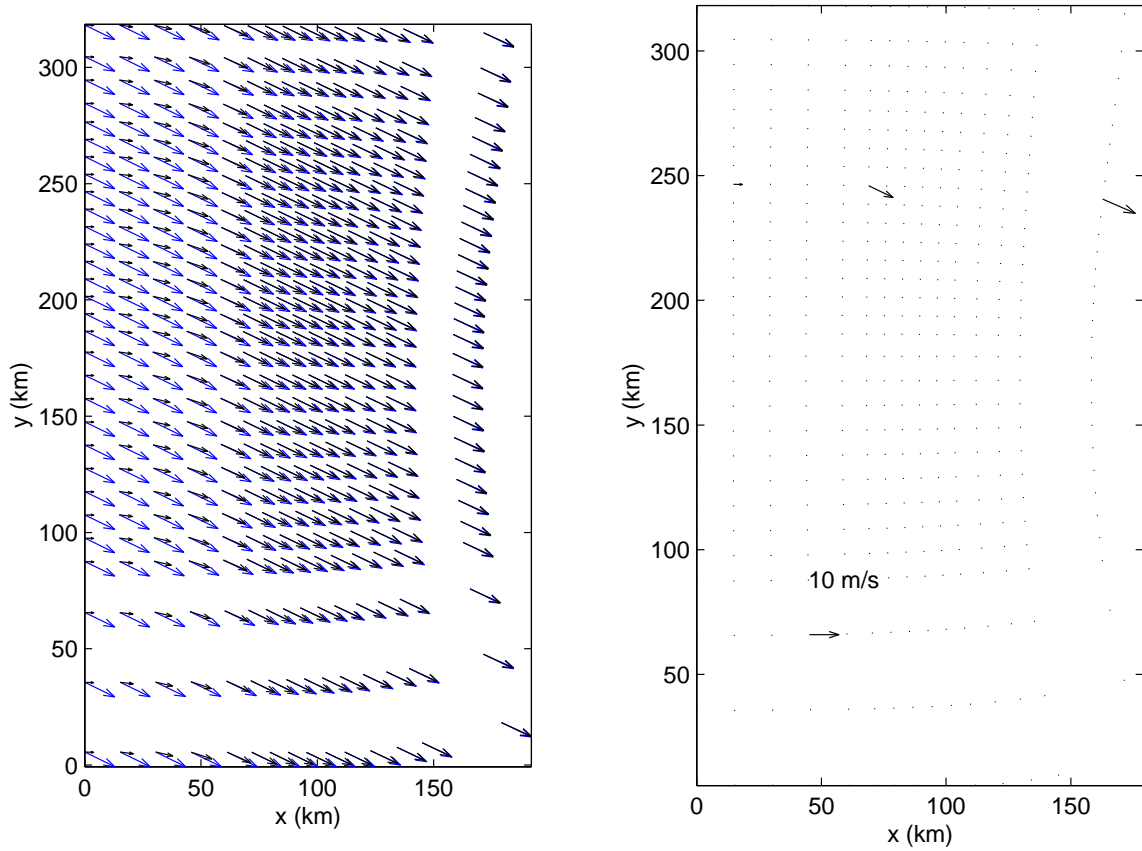


Figure 4.14: Spatially constant wind field (blue arrow) and interpolated wind field (black arrow) in model domain in the left panel; Right panel shows the three wind vectors used in interpolation and a reference vector at 03:00 October 28, 2003

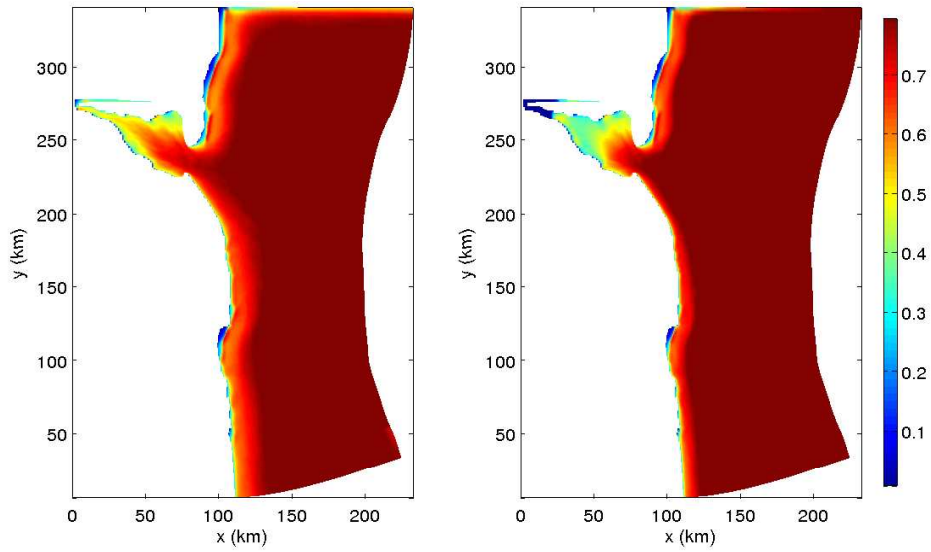


Figure 4.15: Significant wave height with spatially constant wind field (left panel) and interpolated wind field (right panel) in model domain at 03:00 October 28, 2003 (Unit in color bar is m)

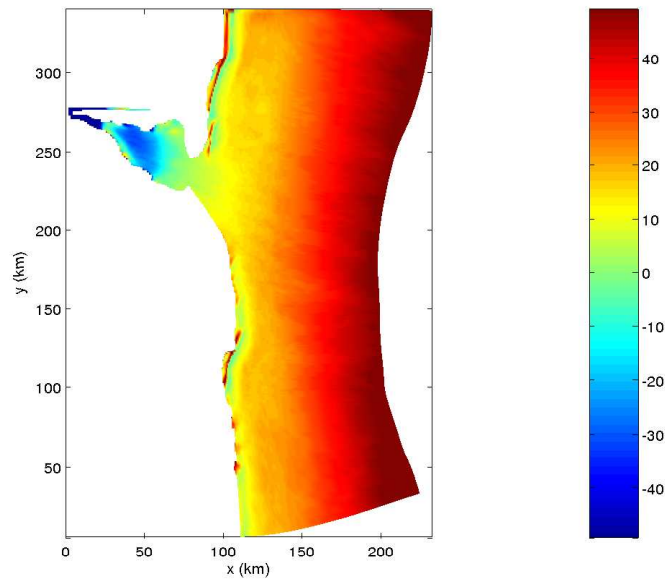


Figure 4.16: Difference of significant wave height with spatially constant wind field and interpolated wind field in model domain at 03:00 October 28, 2003 (Unit in color bar is percentage)

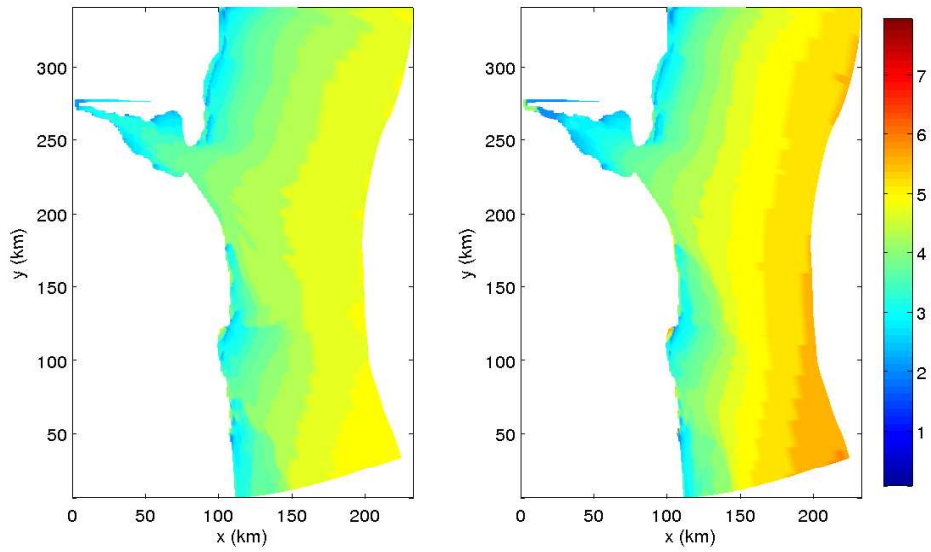


Figure 4.17: Peak period with spatially constant wind field (left panel) and interpolated wind field (right panel) in model domain at 03:00 October 28, 2003 (Unit in color bar is s)

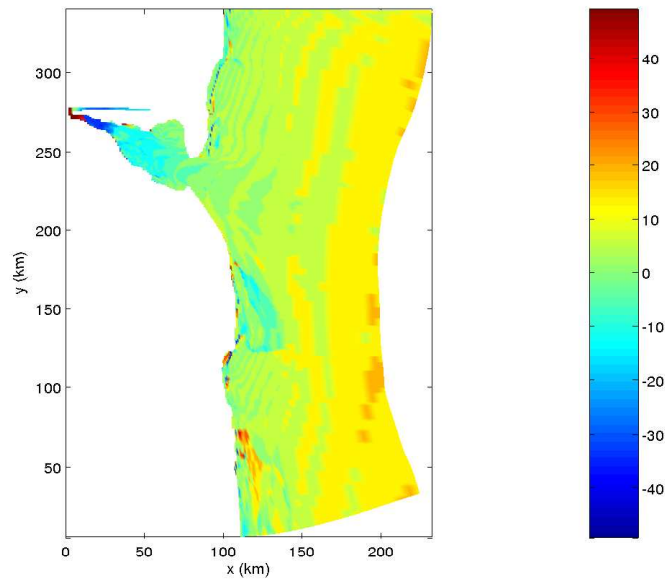


Figure 4.18: Difference of peak period with spatially constant wind field and interpolated wind field in model domain at 03:00 October 28, 2003 (Unit in color bar is percentage)

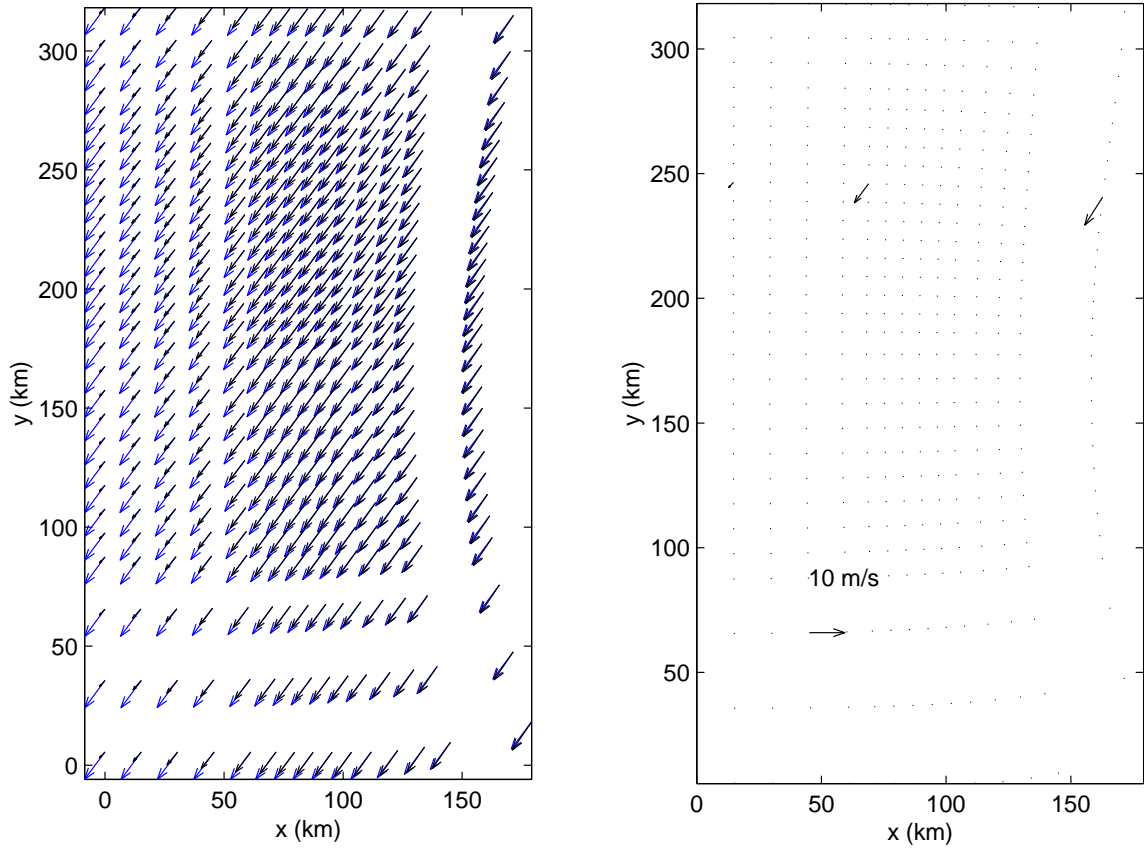


Figure 4.19: Spatially constant wind field (blue arrow) and interpolated wind field (black arrow) in model domain in the left panel; Right panel shows the three wind vectors used in interpolation and a reference vector at 00:00 October 29, 2003

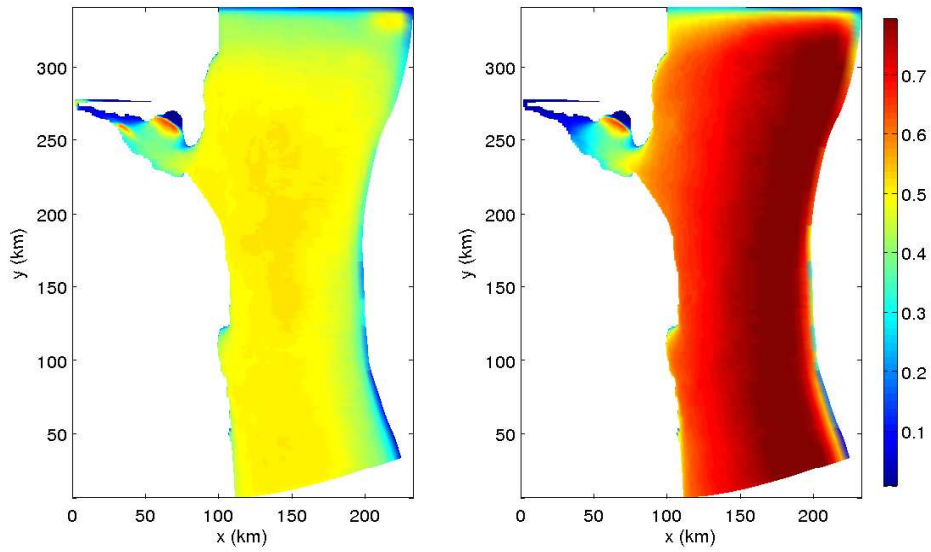


Figure 4.20: Significant wave height with spatially constant wind field (left panel) and interpolated wind field (right panel) in model domain at 00:00 October 29, 2003 (Unit in color bar is m)

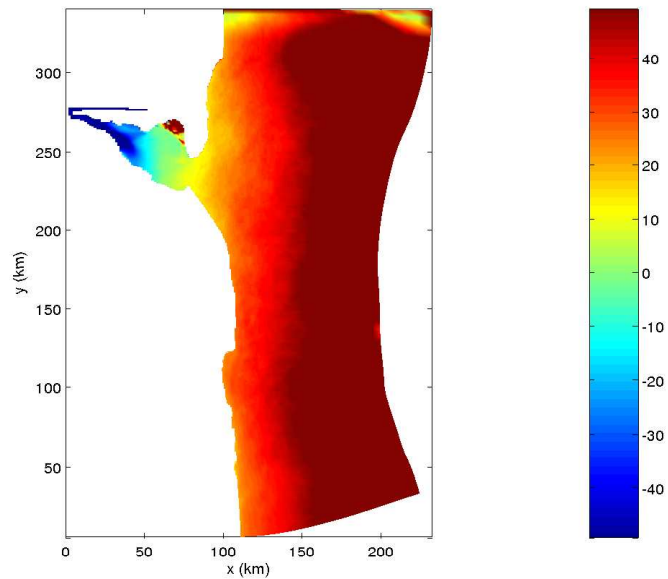


Figure 4.21: Difference of significant wave height with spatially constant wind field and interpolated wind field in model domain at 00:00 October 29, 2003 (Unit in color bar is percentage)

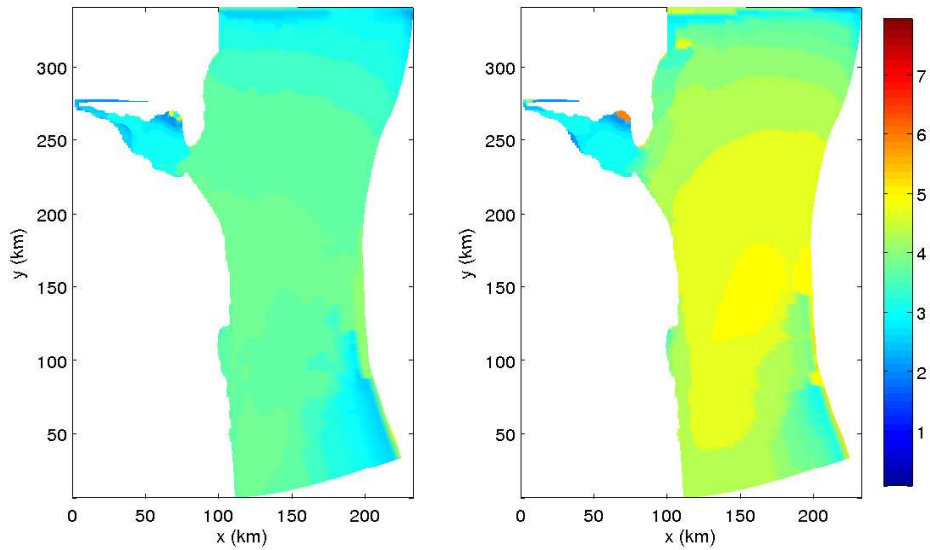


Figure 4.22: Peak period with spatially constant wind field (left panel) and interpolated wind field (right panel) in model domain at 00:00 October 29, 2003 (Unit in color bar is s)

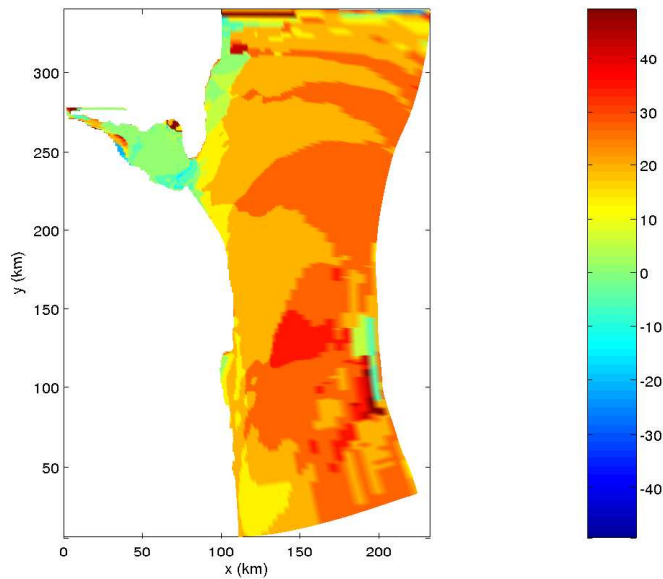


Figure 4.23: Difference of peak period with spatially constant wind field and interpolated wind field in model domain at 00:00 October 29, 2003 (Unit in color bar is percentage)

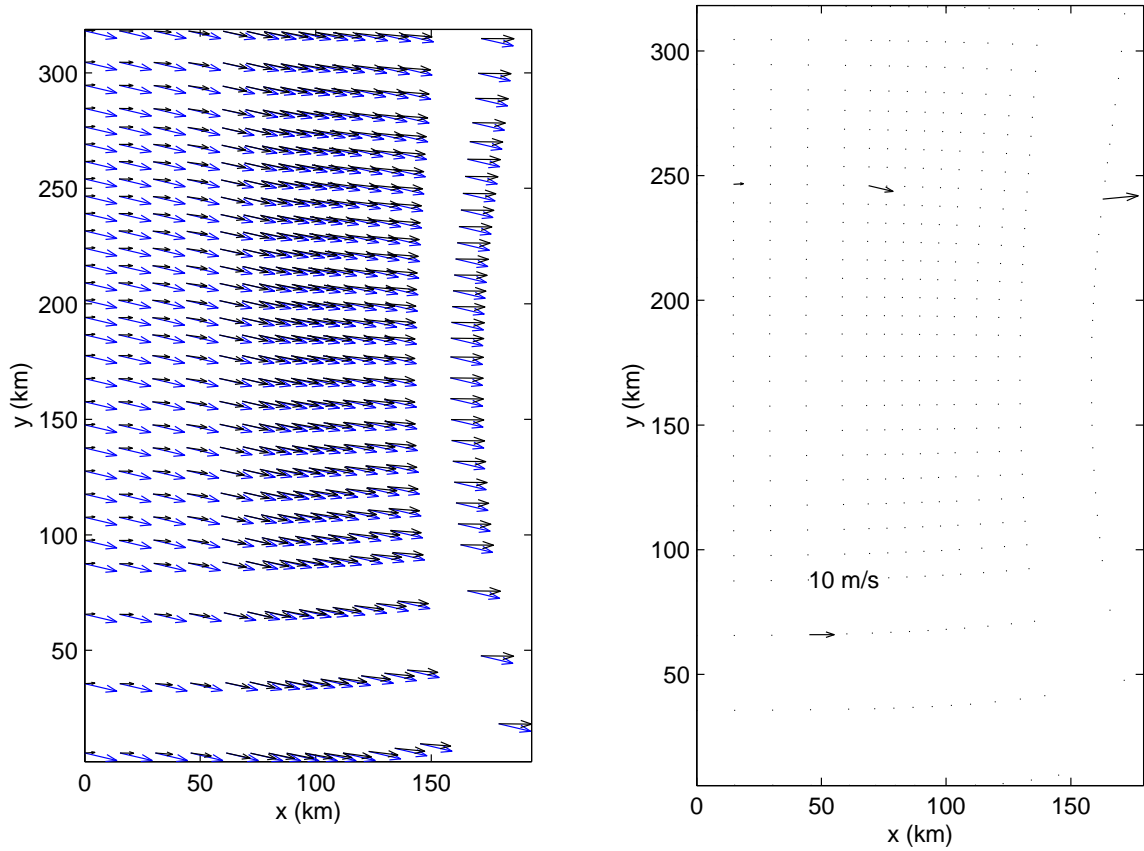


Figure 4.24: Spatially constant wind field (blue arrow) and interpolated wind field (black arrow) in model domain in the left panel; Right panel shows the three wind vectors used in interpolation and a reference vector at 12:00 October 29, 2003

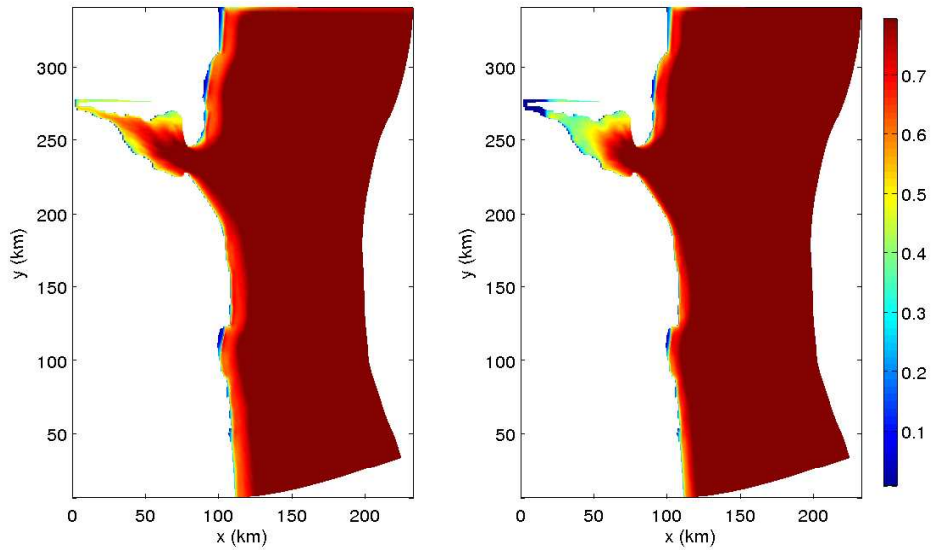


Figure 4.25: Significant wave height with spatially constant wind field (left panel) and interpolated wind field (right panel) in model domain at 12:00 October 29, 2003 (Unit in color bar is m)

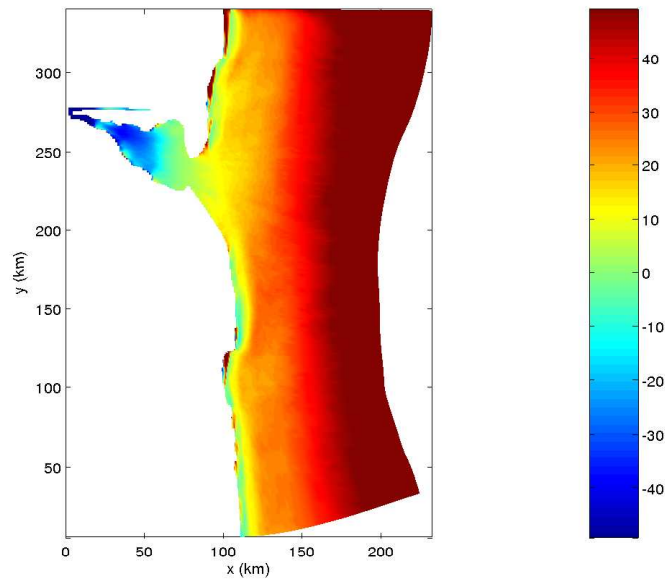


Figure 4.26: Difference of significant wave height with spatially constant wind field and interpolated wind field in model domain at 12:00 October 29, 2003 (Unit in color bar is percentage)

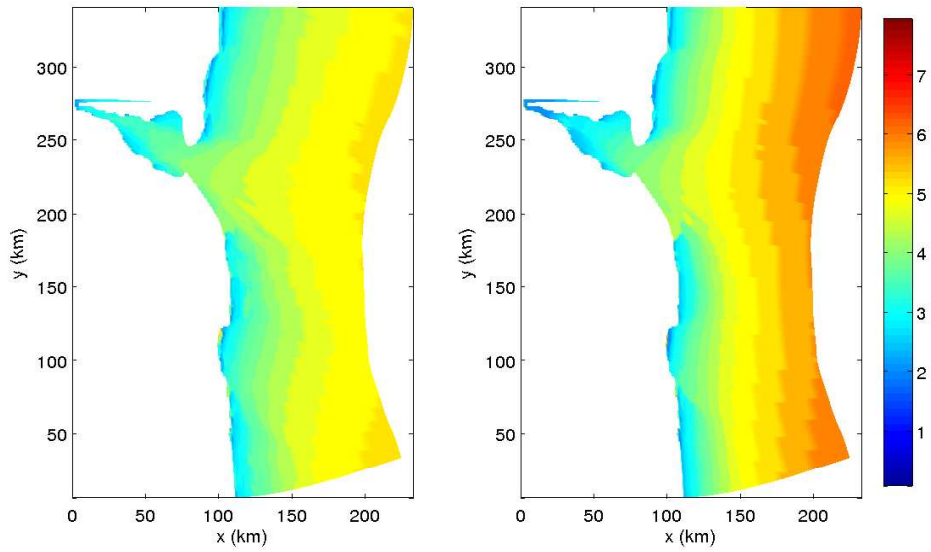


Figure 4.27: Peak period with spatially constant wind field (left panel) and interpolated wind field (right panel) in model domain at 12:00 October 29, 2003 (Unit in color bar is s)

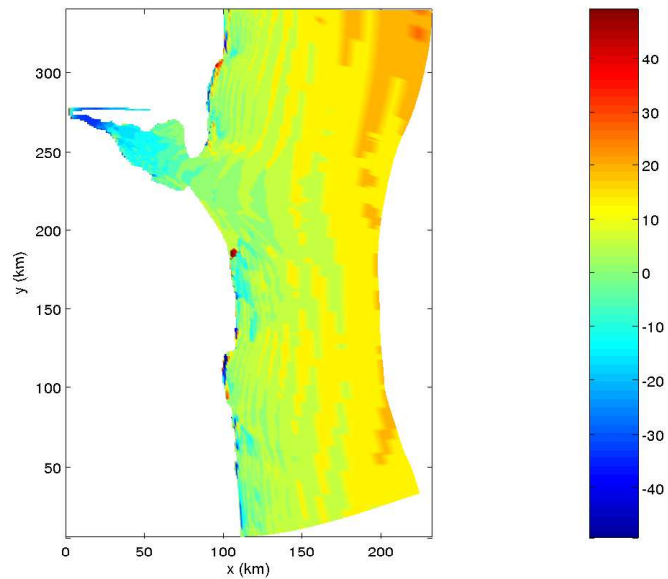


Figure 4.28: Difference of peak period with spatially constant wind field and interpolated wind field in model domain at 12:00 October 29, 2003 (Unit in color bar is percentage)

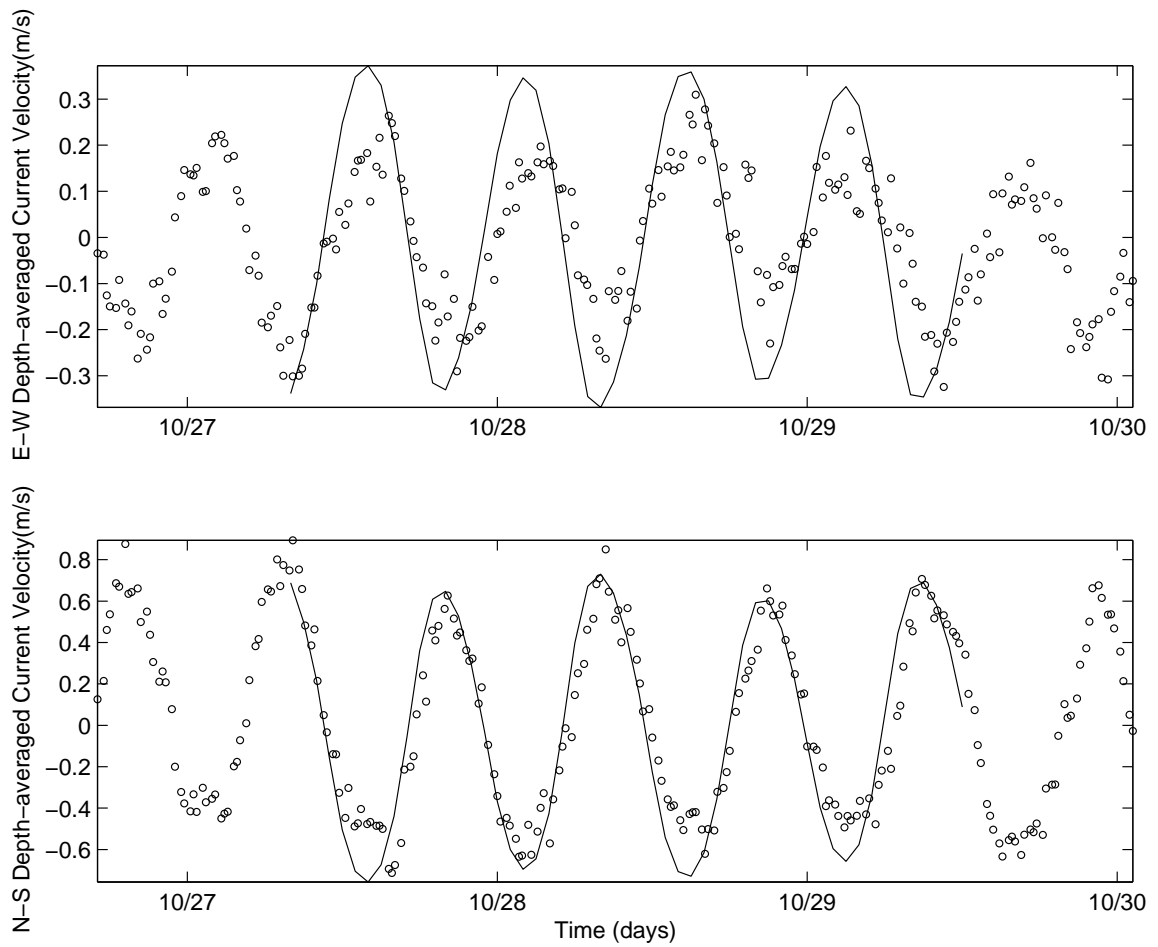


Figure 4.29: Comparison of depth-averaged current velocity between measurement of ADCP (circle) and ROMS (solid line) at measuring station in October, 2003. Positive values point to east and north.

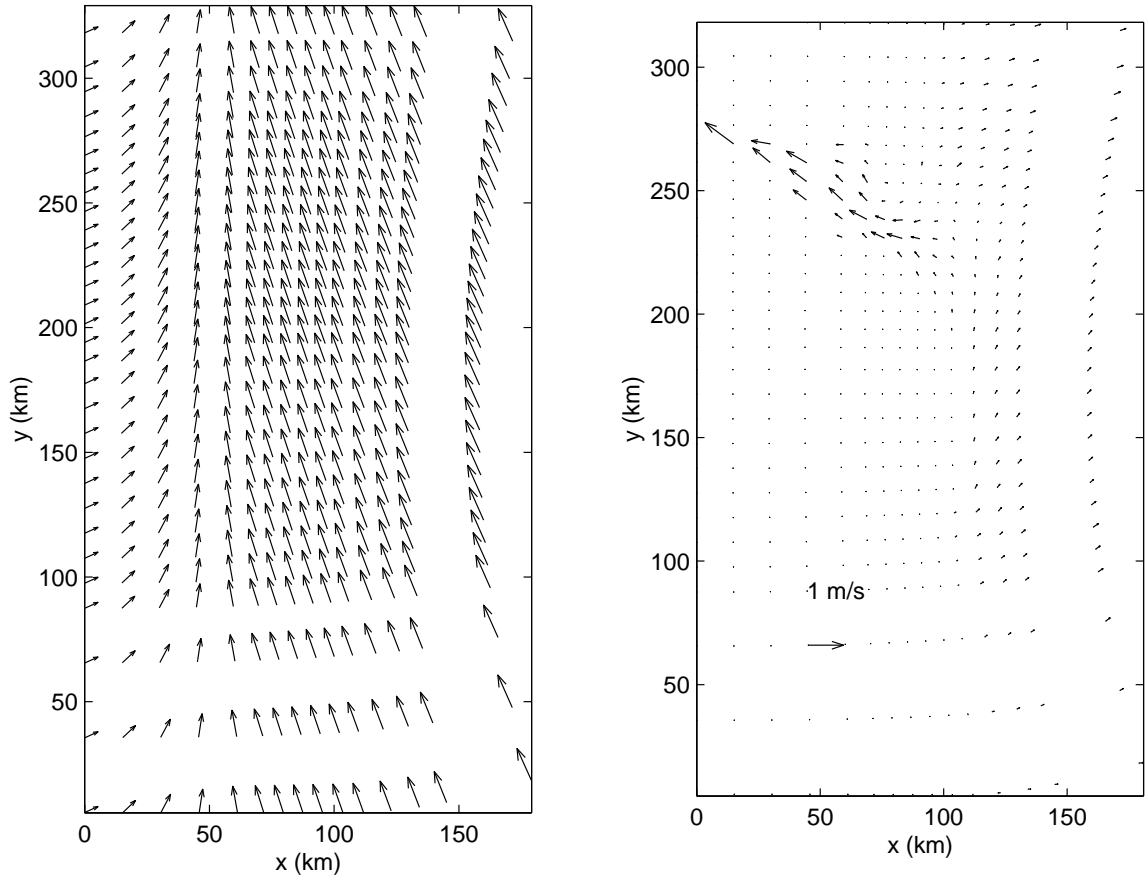


Figure 4.30: Spatially variable wind field (left panel) and tidal current field (right panel) in model domain at 20:00 October 27, 2003

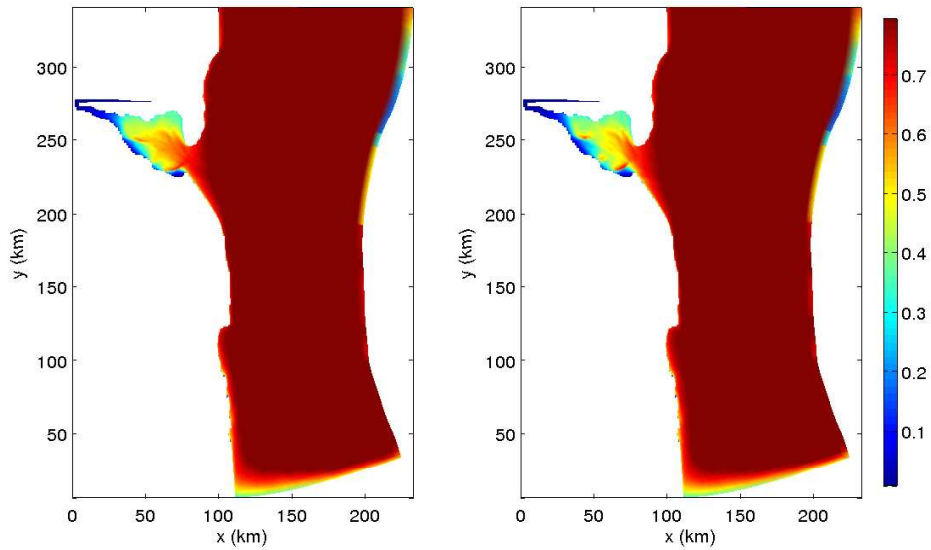


Figure 4.31: Significant wave height without (left panel) and with (right panel) tidal current field on spatially variable wind field in model domain at 20:00 October 27, 2003 (Unit in color bar is m)

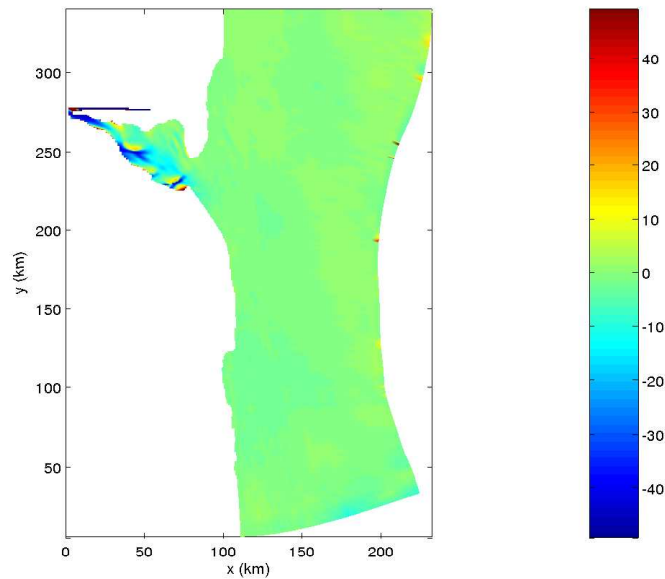


Figure 4.32: Difference of significant wave height with and without current field in spatially interpolated wind field in model domain at 20:00 October 27, 2003 (Unit in color bar is percentage)

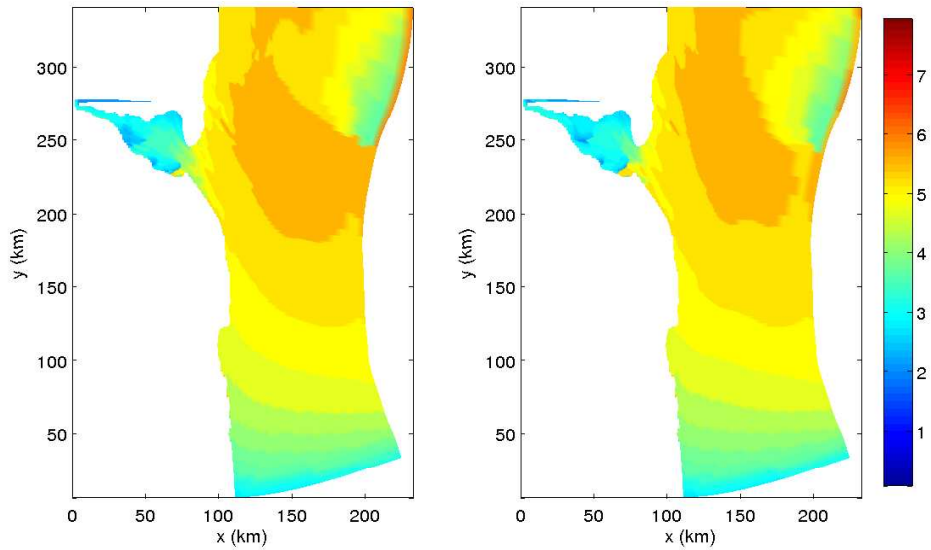


Figure 4.33: Peak period without (left panel) and with (right panel) tidal current field on spatially variable wind field in model domain at 20:00 October 27, 2003 (Unit in color bar is s)

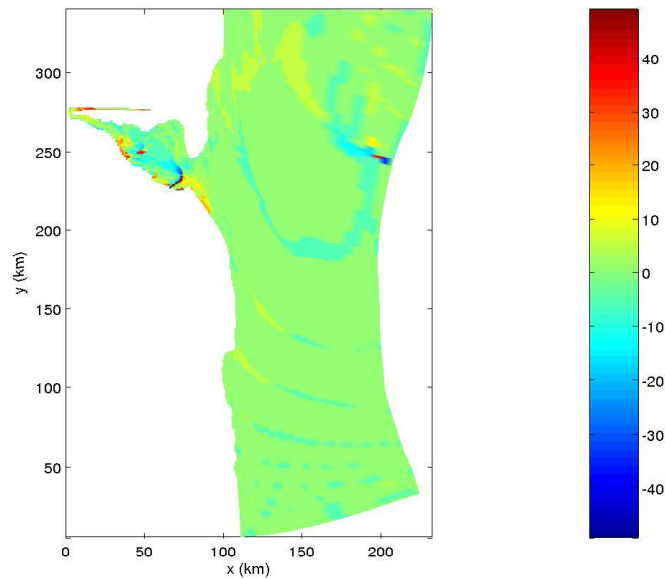


Figure 4.34: Difference of peak period with and without current field in spatially interpolated wind field in model domain at 20:00 October 27, 2003 (Unit in color bar is percentage)

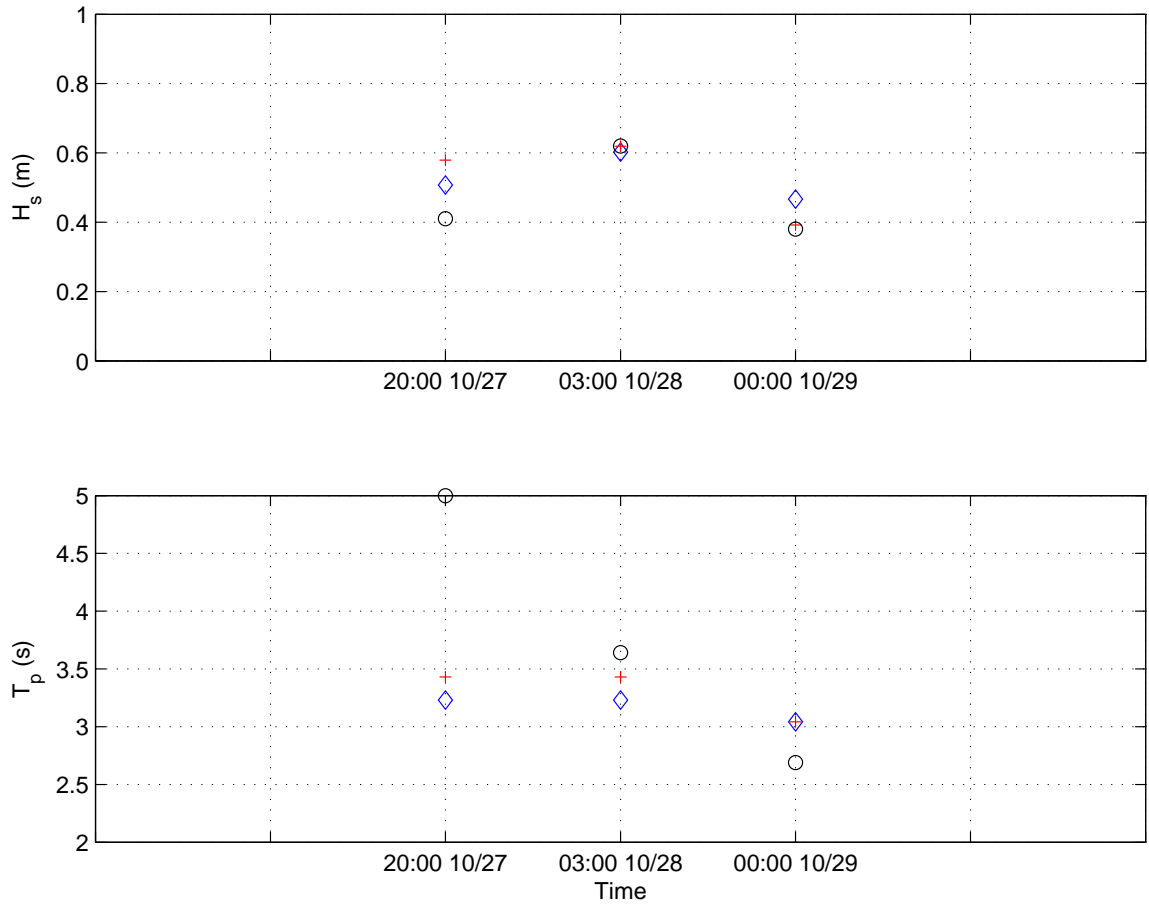


Figure 4.35: Comparison of Significant wave height (H_s), Peak period (T_p) near Fourteen Ft. Bank Lighthouse without (red cross) and with (blue diamond) tidal current field on spatially variable wind field and measured data by WSB (black circle) at some time in 2003

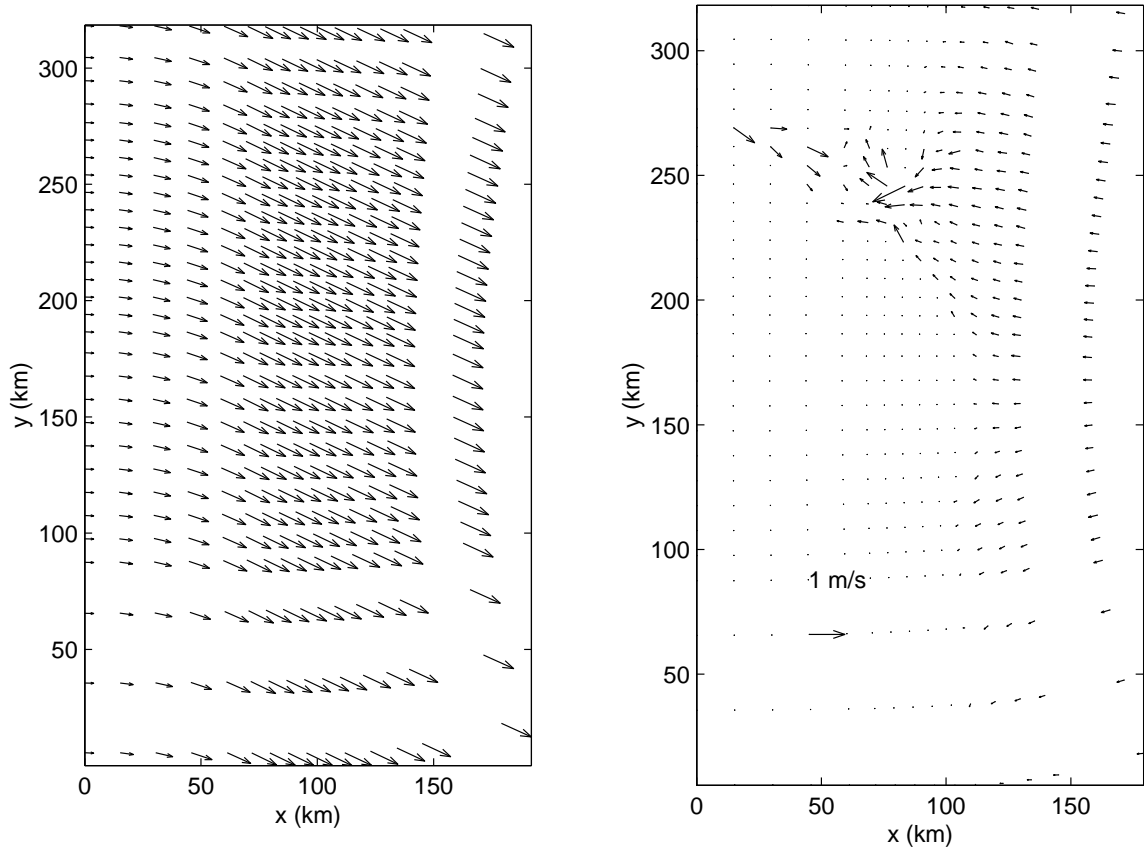


Figure 4.36: Spatially variable wind field (left panel) and tidal current field (right panel) in model domain at 03:00 October 28, 2003

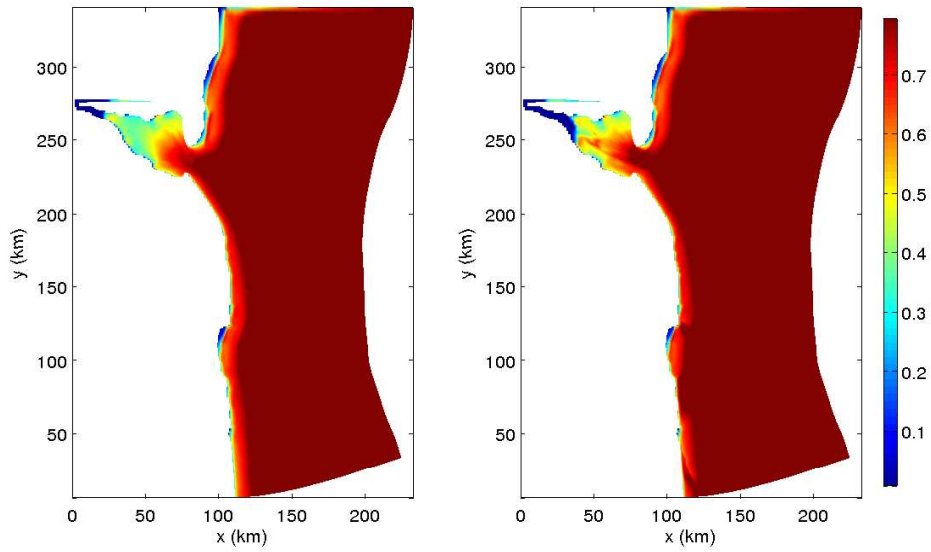


Figure 4.37: Significant wave height without (left panel) and with (right panel) tidal current field on spatially variable wind field in model domain at 03:00 October 28, 2003 (Unit in color bar is m)

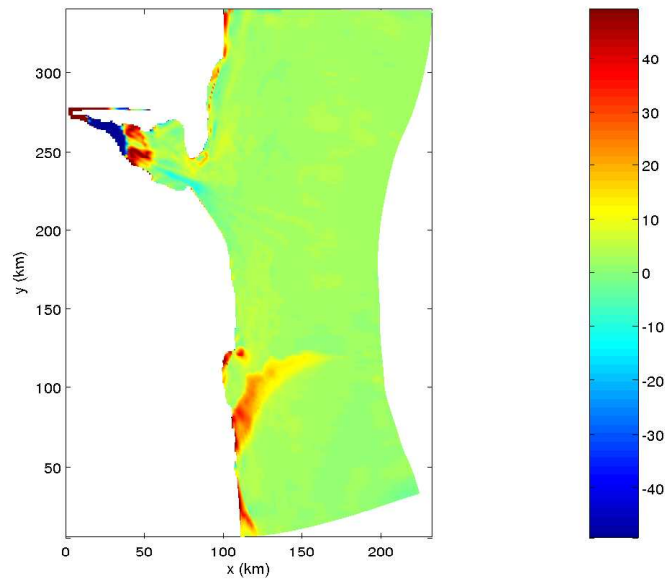


Figure 4.38: Difference of significant wave height with and without current field in spatially interpolated wind field in model domain at 03:00 October 28, 2003 (Unit in color bar is percentage)

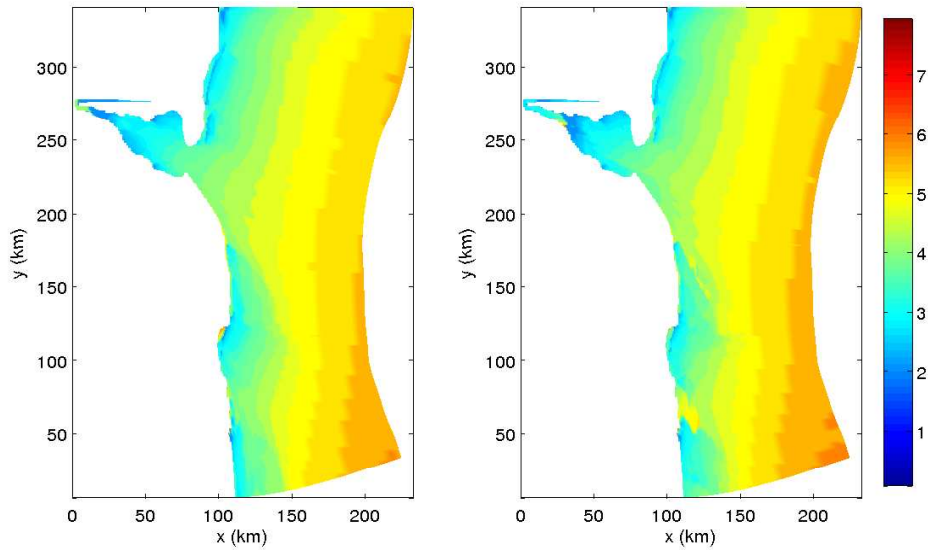


Figure 4.39: Peak period without (left panel) and with (right panel) tidal current field on spatially variable wind field in model domain at 03:00 October 28, 2003 (Unit in color bar is s)

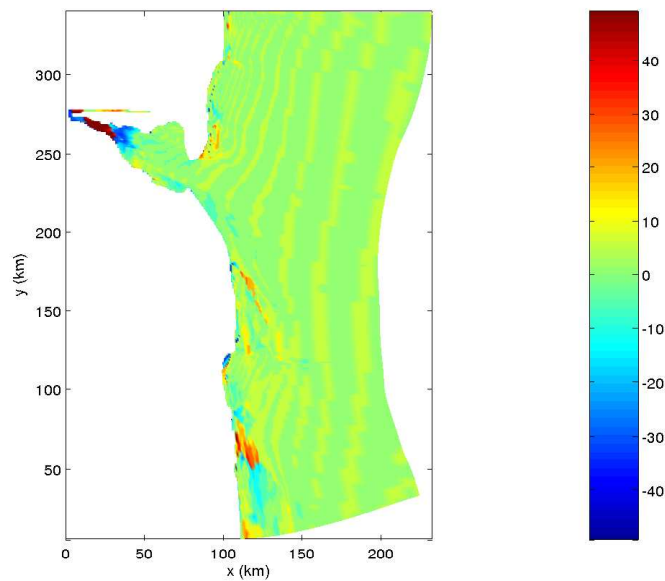


Figure 4.40: Difference of peak period with and without current field in spatially interpolated wind field in model domain at 03:00 October 28, 2003 (Unit in color bar is percentage)

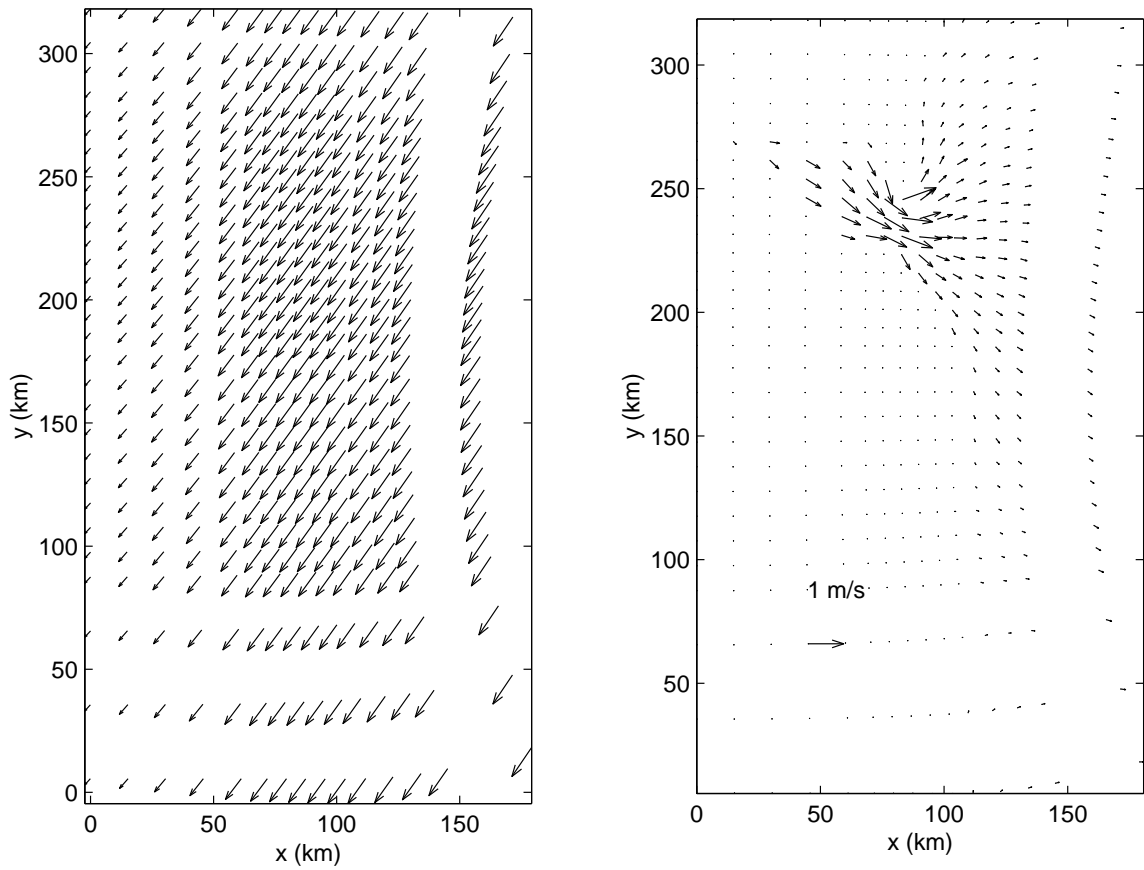


Figure 4.41: Spatially variable wind field (left panel) and tidal current field (right panel) in model domain at 00:00 October 29, 2003

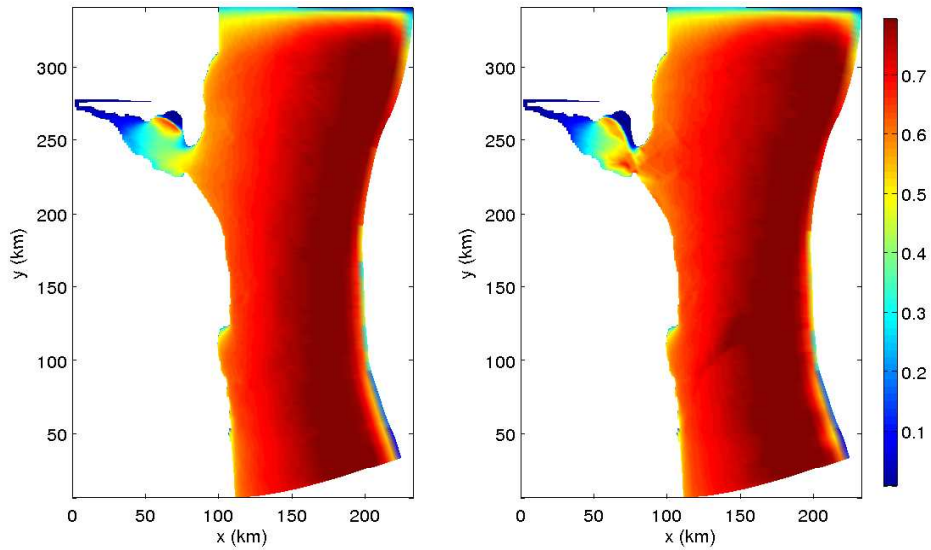


Figure 4.42: Significant wave height without (left panel) and with (right panel) tidal current field on spatially variable wind field in model domain at 00:00 October 29, 2003 (Unit in color bar is m)

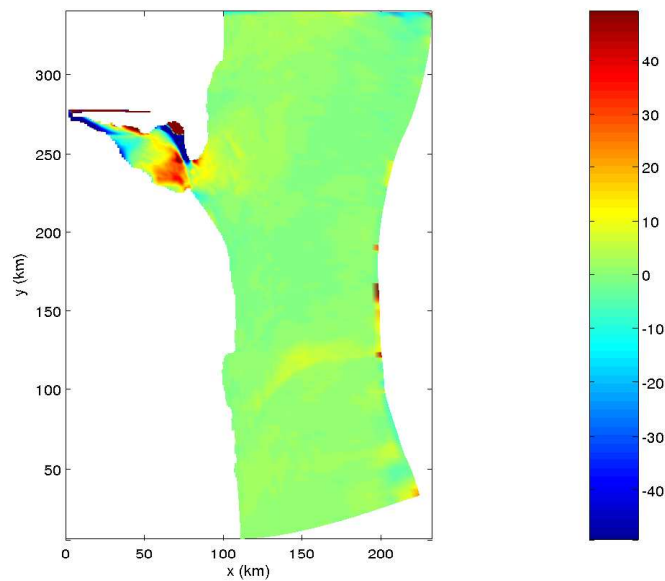


Figure 4.43: Difference of significant wave height with and without current field in spatially interpolated wind field in model domain at 00:00 October 29, 2003 (Unit in color bar is percentage)

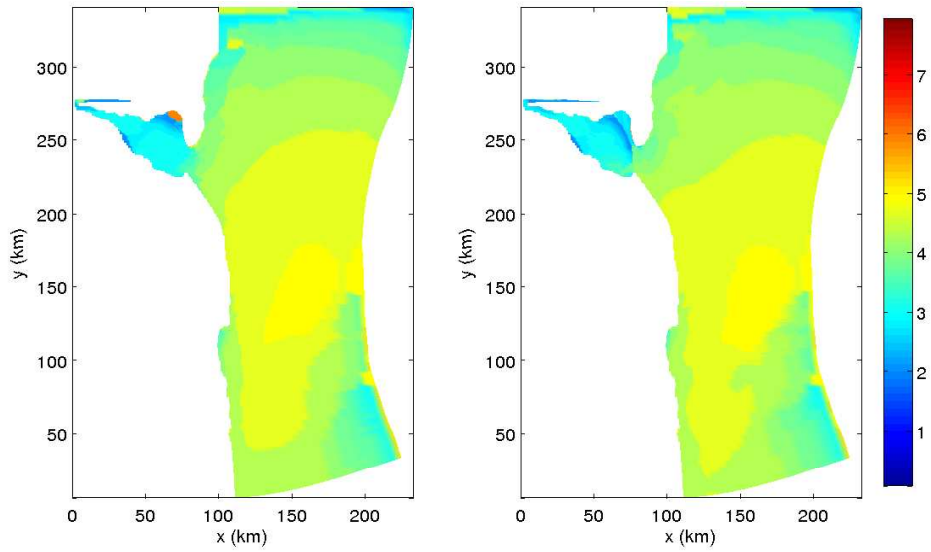


Figure 4.44: Peak period without (left panel) and with (right panel) tidal current field on spatially variable wind field in model domain at 00:00 October 29, 2003 (Unit in color bar is s)

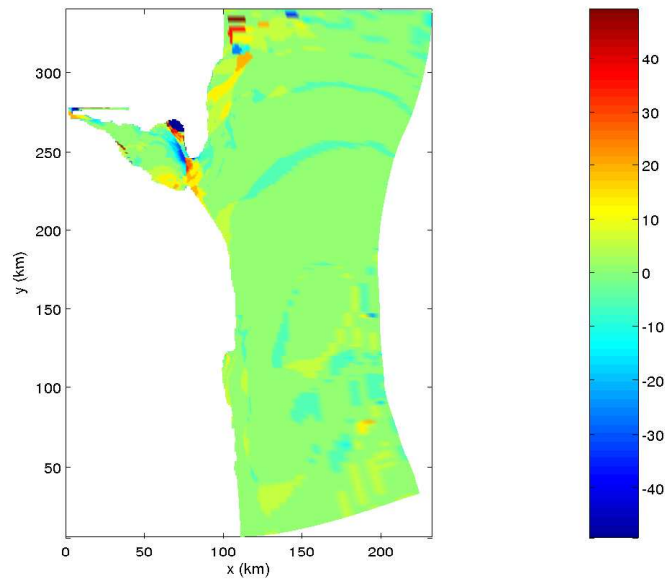


Figure 4.45: Difference of peak period with and without current field in spatially interpolated wind field in model domain at 00:00 October 29, 2003 (Unit in color bar is percentage)

Chapter 5

MODEL-DATA COMPARISON

In this chapter, simulations of wave condition in Delaware Bay are compared to in situ measurements. One set of observation data is from the high-frequency broad-band acoustic propagation experiment in September 1997 (HFA97) (Lenain, 2002). Another sets of observation data are from Wave Sentry Buoy (WSB) in October 2003 and May 2005 respectively. SWAN and ROMS are run in these time periods, and the results are compared with the measured data.

5.1 HFA97 Experiment

HFA97 was conducted in September at the site of $75^{\circ}11'W$, $39^{\circ}01'N$ in the Delaware Bay. The purpose of the experiments was to relate acoustic fluctuations to environmental parameters. However, several oceanographic and meteorological measurements, including tide height, surface wave spectra, current profiles, sound speed profiles, air temperature, wind speed, and wind direction were made coincident with the acoustic measurements. The environmental conditions for the experiment are reported in Lenain (2002). Although there was no sea surface condition available directly, an acoustic technique has been used to estimate sea surface frequency spectra at different transmission times (Heitsenrether, 2004). Heitsenrether (2004) compared measured sea surface against the result from the ocean surface model based on JONSWAP spectrum. Here it will be compared to SWAN results.

The wind speed and direction (CCW) measured at Fourteen Ft. Bank Lighthouse during 8:13 Sept. 26 through 18:23 Sept. 29, 1997 are shown in the first

two panels in Figure 5.1. The time interval is $10mins$. Wind speed ranges from 1 to 15 meters per second during the experiment period, and sea surface conditions varied significantly. The wind field used in SWAN is assumed to be uniform and given by the values recorded at Fourteen Ft. Bank Lighthouse. The bathymetry shown in Figure 3.2 is used in simulation. The JONSWAP spectrum and directional spreading with a \cos^2 power function and $\gamma = 3.3$ are set at the seaward boundary. Current fields are obtained by running ROMS driven by M2, N2, S2, K2, O1, K1 and Q1 tides at the seaward boundary per 10 $mins$ during 8:13 Sept. 26 through 18:23 Sept. 29. The current vectors at the site where HFA97 was conducted are shown in the third panel of Figure 5.1. The velocities in east-west and north-south components are shown in the first panel of Figure 5.2. The E-W velocity and N-S velocity are out of phase. N-S velocity is almost double of E-W velocity. The second panel shows the comparison of current velocity between the measured data from ADCP (blue circle) and ROMS (solid line) in east-west. The simulated velocities are underestimated at the maximum of the west component.

SWAN is run for two cases. One is driven by a uniform wind field, which is constructed by using the lighthouse wind speed and velocity throughout the model domain. Another case is driven by a uniform wind field with current fields obtained from ROMS simulation. The fourth and fifth panels in Figure 5.1 indicate the H_s and θ_p at the same site of HFA97 calculated in these cases. H_s is presented as a black line for the first case and as a red line for the second case in the fourth panel. Both of them have the same trend as the wind speed shown in the first panel, which also agrees well with measured H_s (black circles). H_s is overestimated when the wind blows over the shorter fetch. Additionally, θ_p is presented as black diamonds for the first case and as red crosses for the second case. Comparing θ_p shown in the fifth panel with the wind direction shown in the second panel, the peak direction of the waves is close to the wind direction, which indicates the model result is dominated

by the wind input in Delaware Bay.

A comparison between SWAN spectrum and HFA spectrum is shown in Figure 5.3 without current fields and Figure 5.4 with current fields. The left panel in the figures is the wind speed and direction (CCW) measured at Fourteen Ft. Bank Lighthouse. The middle panel shows the frequency spectrum from the acoustic experiment. The frequency spectrum calculated by SWAN is shown in the right panel. The pattern of spectrum changes due to the tidal current. Frequency spectra at 01:00 Sept. 28 and 13:00 Sept. 28 are shown in Figure 5.5. $S(f)$ calculated by spatially uniform wind fields without current fields is presented as black line. Blue line states those calculated by spatially uniform wind fields with current fields. Black circles are measured data. The simulated results underestimate the peak spectra. At 01:00 Sept. 28, the current makes the peak spectrum reduced. There is no big difference between the current and no-current cases at 13:00 Sept. 28, because the current is small at that time.

5.2 2003 Experiment

In 2003, Wave Sentry Buoy (WSB) was deployed near Fourteen Ft. Bank Lighthouse at around $75^{\circ}11'W$, $39^{\circ}01'N$, where the HFA was conducted in 1997. WSB measures directional waves and monitors sea-states in real time. The raw data measured by the wave sensors in WSB are accelerations in bow, stbd and mast, magnetic field bow, magnetic field stbd and magnetic field mast, which are processed to provide directional and nondirectional spectra. The significant wave height and nondirectional frequency spectrum are compared between SWAN results and WSB's. In this experiment, WSB collected the data during 11:00 October 27 through 10:00 October 29.

Both a uniform wind field and a spatially variable wind field were used in SWAN. As we did in Chapter 3, the uniform wind field was constructed by using the wind speed and direction at lighthouse throughout the model domain. The spatially

variable wind field is constructed by interpolating the wind speed and direction at Delaware City, Lighthouse and NDBC 44009. The recorded wind speeds and directions at Delaware City, Fourteen Ft. Bank Lighthouse and NDBC 44009 are presented in Figure 5.6. The time interval of the wind data is $1hr$. All of the wind speeds are adjusted to $10m$ above the sea surface. The wind speed at Delaware City (diamond) is much smaller. Those measured at Lighthouse and NDBC 44009 are close to each other. The wind directions measured at three stations shown in the lower panel (CCW) have the same trends. Hence, the wind speeds at the upper bay will be smaller in uniform wind field than those in variable wind field.

The wave information at the seaward boundary is based on stored results from WWIII. The H_s , T_p and θ_p at the boundary points A , B , C and D are shown in Figure 3.5, Figure 3.6 and Figure 3.7 respectively. The time interval in WWIII archive is $3hrs$. The wave parameters are interpolated into $1hr$ as boundary condition in SWAN simulation.

The current field is obtained by ROMS simulation with seven tidal components M2, N2, S2, K2, O1, K1 and Q1 at the seaward boundary. It is updated every hour. The depth-averaged current velocity at the position of WSB is shown in Figure 4.29. Compare to ADCP data, the simulation results agree well with the experimental data in north-south, but have a little overestimation in east-west. The period of the current is dominated by the M2 tide.

SWAN is run using the different wind fields and current fields to check the effect of the wind distribution and current. The frequency spectrum in time series is compared to those obtained from WSB at the same location. First, the uniform wind field is applied without current field. The spectrum is shown in the right panel of Figure 5.7. Second, the uniform wind field is applied with current field. The spectrum is in the right panel of Figure 5.8. Finally, the spectrum simulated by the spatially variable wind and current field is shown in the right panel of Figure

5.9. Compared to the experiment data in the middle panel, all of these SWAN results overestimate the spectrum. Compare the simulated spectrum in Figure 5.7 and Figure 5.8, the waves are modulated by the tidal current in Figure 5.8. This trend is similar to what was found in the experimental data. Additionally, if the wind blows from upper bay, the spectra are much smaller in Figure 5.9 than those in Figure 5.8, because the wind speed at the upper bay is smaller in spatially variable wind field than in the uniform wind field. The left panel in these figures are the wind speed and direction recorded at Fourteen Ft. Bank Lighthouse during 11:00 Oct. 27 through 10:00 Oct. 29.

Frequency spectra at 13:00 Oct. 27, 10:00 Oct. 28, 00:00 Oct. 29 and 05:00 Oct. 29 are shown in Figure 5.10. $S(f)$ calculated by spatially uniform wind fields without current fields is presented as black line. Blue line states those calculated by spatially uniform wind fields with current fields. Red line states those calculated by spatially variable wind fields with current fields. Black circles are measured data by WSB. In most times, the simulated results overestimate the spectra.

Finally, Figure 5.11 shows H_s and θ_p at the measuring station. The first panel is the wind speed recorded at Fourteen Ft. Bank Lighthouse. The second panel shows the vector of the wind. In third panel, black solid line is H_s calculated only with uniform wind field, and blue solid line is H_s with uniform wind field and current field. Red dash line is with variable wind field and current field. The black circles are values measured by WSB. Fourth panel show the comparison of θ_p in these three cases. Although there is much difference in spectrum pattern due to current, H_s does not change much. Compare the black line with blue line, we find that H_s is increased sometime and reduced sometime due to the effect of the current. We also find some change of H_s due to the wind field distribution by comparing blue line and red line. The difference is larger when the fetch is shorter. Both H_s are overestimated. θ_p is very similar in simulation results.

5.3 2005 Experiment

WSB was deployed again during May 22 through May 27, 2005 in the same site as in 2003. The wind information at Fourteen Ft. Bank Lighthouse, Delaware City measuring station and NDBC 44009 are used. They are shown in Figure 5.12 in the period of 00:00 May 22 through 23:00 May 29. The time interval is $1hr$. The wind speed at Delaware City was still smaller than at other stations. Wind speed ranged from 0 to 13 meters per second. Most of the time, the three stations have same trend in wind direction. But some time, there are significant differences between the stations.

As we did in the 2003 case, the SWAN is run with uniform wind field and spatially variable wind field. The lighthouse wind speed and direction are set throughout the model domain in uniform wind field. The data at three stations are interpolated to be the spatially variable wind field.

The boundary condition at the seaward boundary is obtained from archived WWIII runs. The H_s , T_p and θ_p at the boundary points A , B , C and D are shown in Figure 5.13, Figure 5.14 and Figure 5.15 respectively. The time interval in WWIII archive is $3hrs$. The wave parameters are interpolated into $1hr$ as boundary condition in SWAN simulation.

The current field is obtained by ROMS simulation with seven tidal components M2, N2, S2, K2, O1, K1 and Q1 at the seaward boundary. It is updated every hour. The depth-averaged current velocity at the position of WSB is shown in Figure 5.16. The simulated results are compared to ADCP data. The north-south current velocity agrees well with the measured data. The east-west current velocity is overestimated as the comparison in 2003 experiment.

First, the uniform wind field is applied without current field. The spectrum is shown in the right panel of Figure 5.17. Second, the uniform wind field is applied with current field. The spectrum is in the right panel of Figure 5.18. Finally, the

spectrum simulated by the spatially variable wind and current field is shown in the right panel of Figure 5.19. Compared to the experiment data in the middle panel, all of these cases overestimate the spectrum. Compare the simulated spectrum in Figure 5.17 and Figure 5.18, we can see the waves modulated by the current obviously in Figure 5.18 as we have found in the experiment data. Again, these plots show similarities between the measured spectrum and SWAN spectrum when current effect are introduced to simulation. The spatially variable wind field reduces the wind speed in upper bay, so some spectra in Figure 5.19 are smaller than those in Figure 5.18. The left panel in these figures are the wind speed and direction recorded at Fourteen Ft. Bank Lighthouse during 13:00 May 22 through 15:00 May 27. The middle panel shows the frequency spectrum from WSB.

Frequency spectra at 10:00 May 25, 16:00 May 25, 22:00 May 25 and 04:00 May 26 are shown in Figure 5.20. $S(f)$ calculated by spatially uniform wind fields without current fields is presented as black line. Blue line states those calculated by spatially uniform wind fields with current fields. Red line states those calculated by spatially variable wind fields with current fields. Black circles are measured data by WSB. Although no simulated results can match the peak frequency exactly with the measured data, the results (red line) under variable wind fields with current fields are closer to the measured data than other two. When peak spectrum is less than 0.1 (at 16:00 May 25 and 04:00 May 26), simulated results are overestimated.

The comparisons of the H_s and θ_p in different cases are shown in Figure 5.21. The first two panels show the wind vector and current vector. In third panel, black solid line is H_s calculated only with unifom wind field, and blue solid line is H_s with uniform wind field and current field. Red dash line is with variable wind field and current field. The experiment data from WSB are presented as black circles. Fourth panel show the comparison of θ_p in these three cases. Although there is much difference in spectrum pattern due to current, H_s does not change much. Also

the wind field changes H_s slightly. θ_p is very similar in simulated results, which is dominated by the wind input.

Some statistical parameters are calculated for wave parameters, such as *Bias*, *RMSE*, *SI* and *IOA*. The definitions of these parameters (Padilla-Hernández et al., 2004) are given by:

1) *Bias*, the difference between X , the mean of observed data (x_i) and Y , the mean of model data (y_i):

$$Bias = X - Y \quad (5.1)$$

2) *RMSE*, the root mean square error is

$$RMSE = \left[\frac{1}{N} \sum_{i=1}^N (y_i - x_i)^2 \right]^{1/2} \quad (5.2)$$

3) *SI*, the scatter index:

$$SI = RMSE / (XY)^{1/2} \quad (5.3)$$

4) *IOA*, the index of agreement or relative error:

$$IOA = 1 - \frac{N \times RMSE^2}{PE} \quad (5.4)$$

with

$$PE = \sum_i [|y_i - Y| + |x_i - X|]^2 \quad (5.5)$$

PE is the potential variance. *IOA* reflects the degree to which observations and model results agree.

Based on the uniform wind field, Table 5.1 presents the comparison of current effect for H_s , T_p and θ_p . It seems that including the current field has only a small improvement in some of the parameters at the measuring station.

Table 5.2 presents the statistical parameters for H_s , T_p and θ_p , which compares the uniform wind field and variable wind field to the measured data. At this measuring station, although the uniform wind field has better agreement than the variable wind field in H_s and θ_p , the difference is small.

Table 5.1: Overall mean values of statistical parameters at the measuring station (with and without current field)

	H_s		T_p		θ_p	
	without	with	without	with	without	with
<i>Bias</i>	0.0795	0.0699	1.7575	1.6626	37.6805	49.4691
<i>RMSE</i>	0.1348	0.1289	3.8053	3.7137	112.4933	113.3257
<i>SI</i>	0.3690	0.3479	0.9164	0.8820	0.7893	0.8356
<i>IOA</i>	0.8939	0.9126	0.1405	0.2078	0.4874	0.4175

Table 5.2: Overall mean values of statistical parameters at the measuring station (uniform wind field and variable wind field)

	H_s		T_p		θ_p	
	uniform	variable	uniform	variable	uniform	variable
<i>Bias</i>	0.0699	0.0838	1.6626	1.6387	49.4691	50.0382
<i>RMSE</i>	0.1289	0.1378	3.7137	3.8030	113.3257	113.123
<i>SI</i>	0.3479	0.3798	0.8820	0.9001	0.8356	0.836
<i>IOA</i>	0.9126	0.8953	0.2078	0.2213	0.4175	0.4159

5.4 Conclusion

Both SWAN and ROMS simulations were compared with three sets of experimental data. The simulated current velocities at the measuring station were compared to ADCP data. The north-south current velocity agrees well with the measured data. The simulated east-west current velocity was underestimated in 1997 case, while it was overestimated in 2003 and 2005 cases. It is found that wind field distribution does not affect θ_p much, but affect the frequency spectrum at the measuring station. Both the uniform wind field and the spatially variable wind field overestimated the significant wave height at the Fourteen Ft. Bank Lighthouse measuring station in some period of 1997 case and 2003 case. But they underestimated slightly in 2005 case. H_s was affected by the change of the fetch due to the change of the wind distribution. The waves were modulated by currents obviously.

The pattern of the spectrum at the measuring station changes due to the effect of the current. So the coupling model of ROMS and SWAN helps in showing better comparison between the modeled and the measured data.

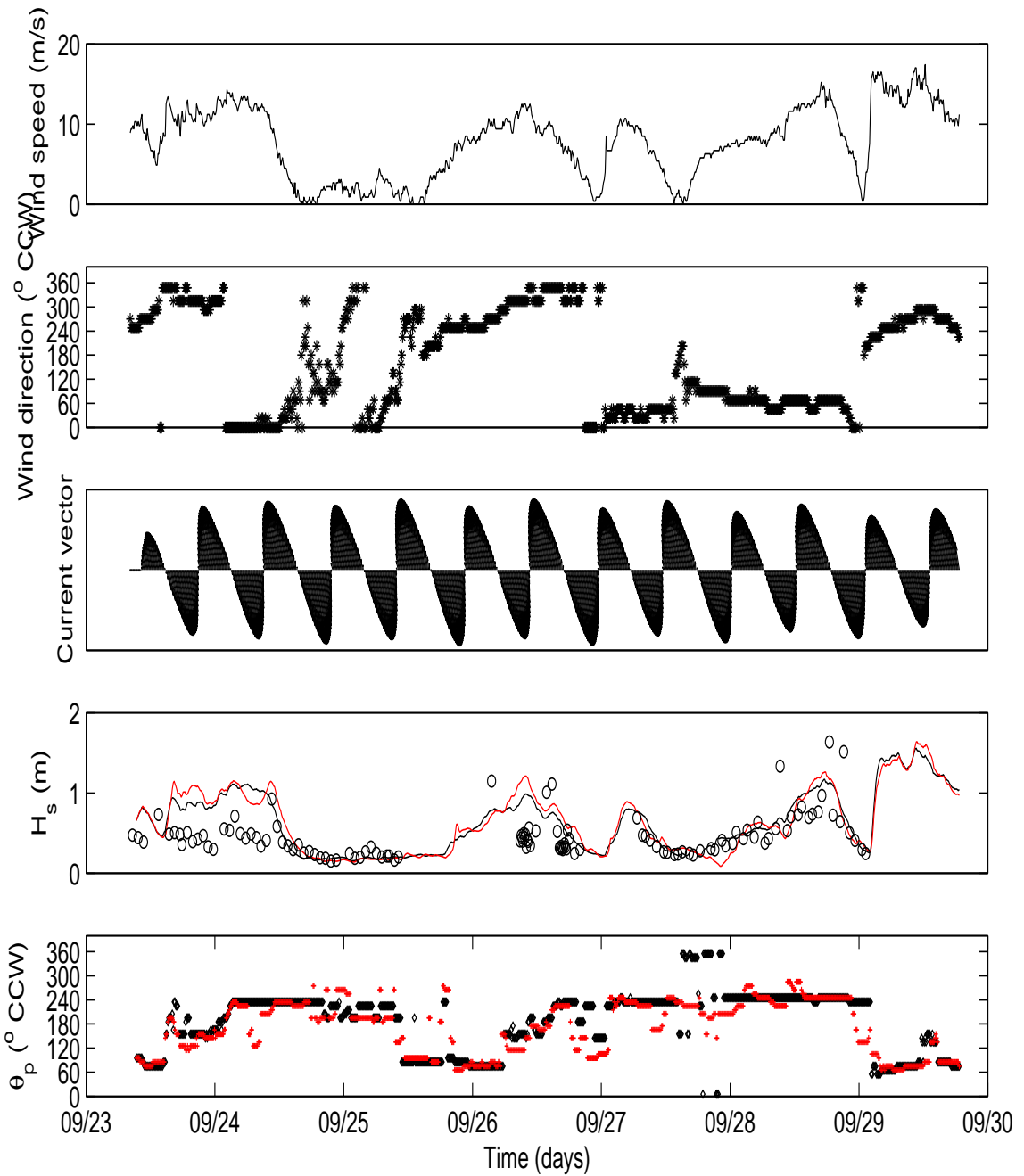


Figure 5.1: First two panels: measured wind speed, wind direction measured at DBOS from 08:13 Sept. 23 to 18:23 Sept. 29, 1997; Third panel: H_s calculated by SWAN with uniform wind field without (black line) and with (red line) current fields. Acoustic experiment data are black circles; Last panel: θ_p comparison between no-current (black diamonds) and current (red crosses)

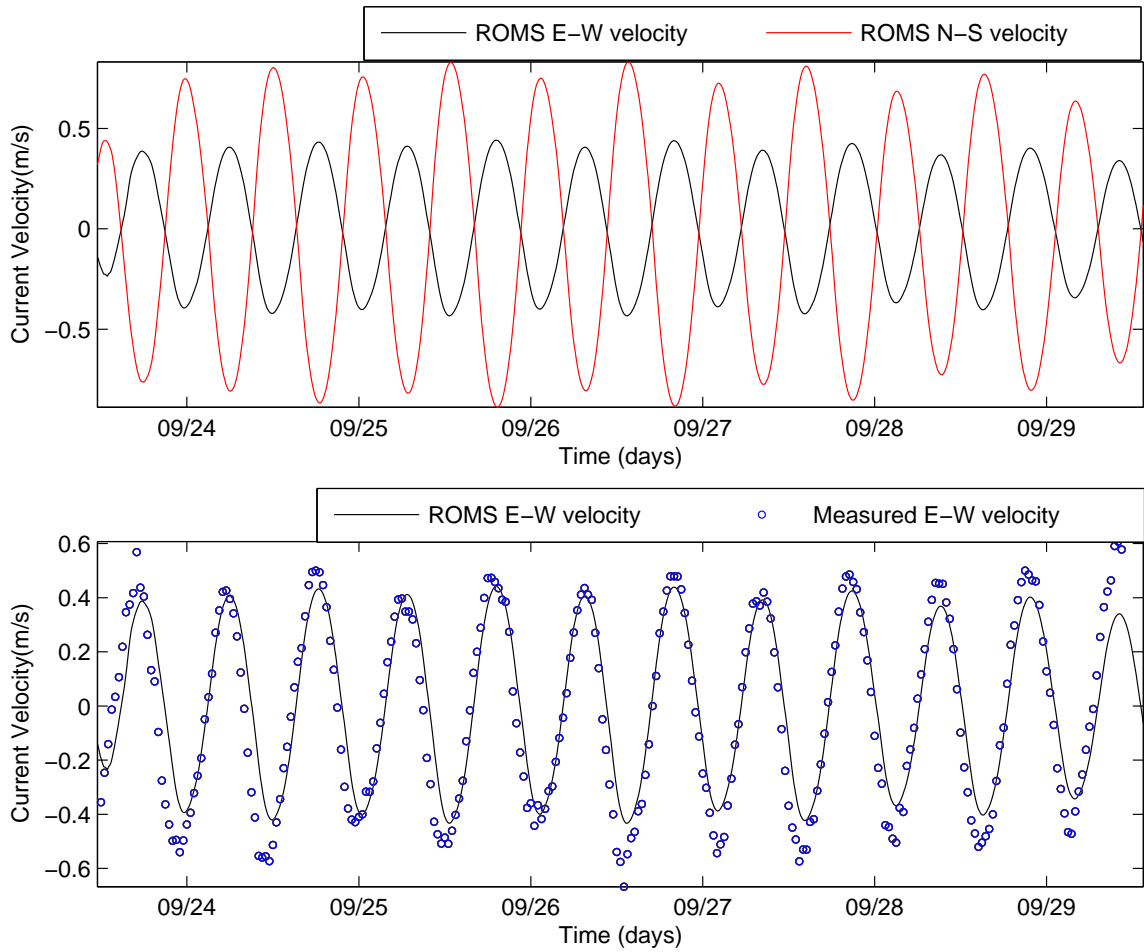


Figure 5.2: First panel: Simulated depth-averaged current velocity in east-west (black line) and north-south (red line) at HFA experiment site from 08:13 Sept. 23 to 18:23 Sept. 29, 1997. Second panel: Comparison of depth-averaged current velocity between measurement of ADCP (blue circle) and ROMS (black line) in east-west. Positive values point to east and north.

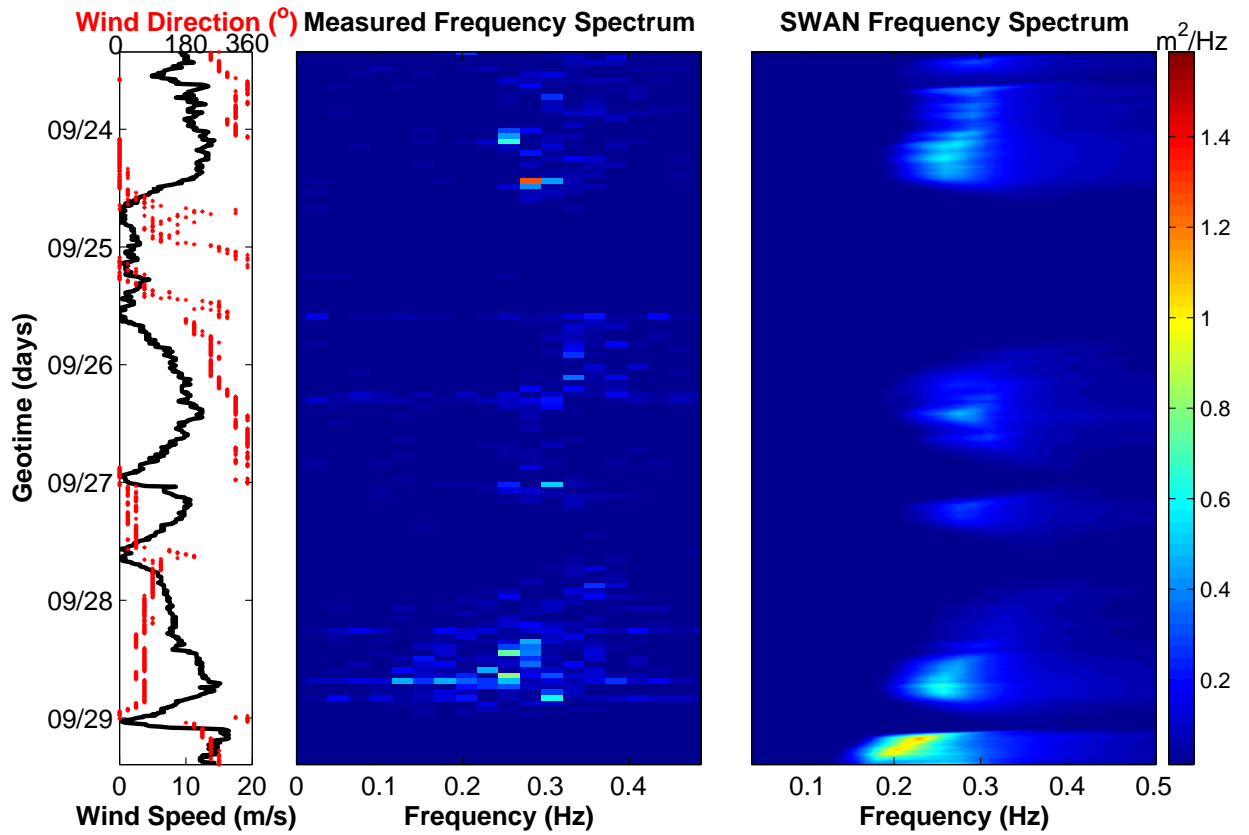


Figure 5.3: Left panel: Recorded wind speed (black solid line) and direction (red points, CCW) during 08:13 Sept. 23 through 18:23 Sept 29, 1997 at Fourteen Ft. Bank Lighthouse; Middle panel: Frequency spectrum from acoustic experiment; Right panel: Frequency spectrum from SWAN simulation with uniform wind field

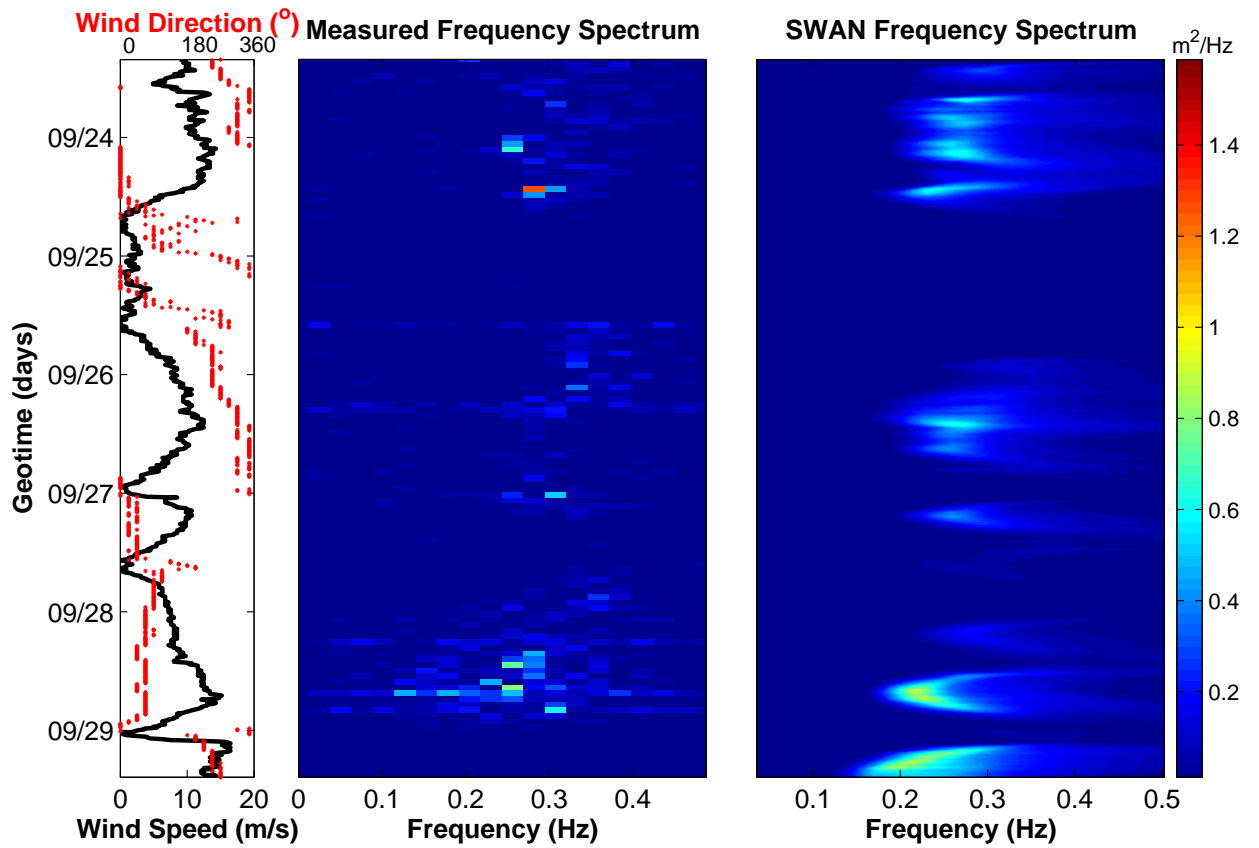


Figure 5.4: Left panel: Recorded wind speed (black solid line) and direction (red points, CCW) during 08:13 Sept. 23 through 18:23 Sept 29, 1997 at Fourteen Ft. Bank Lighthouse; Middle panel: Frequency spectrum from acoustic experiment; Right panel: Frequency spectrum from SWAN simulation with uniform wind field and current fields from ROMS

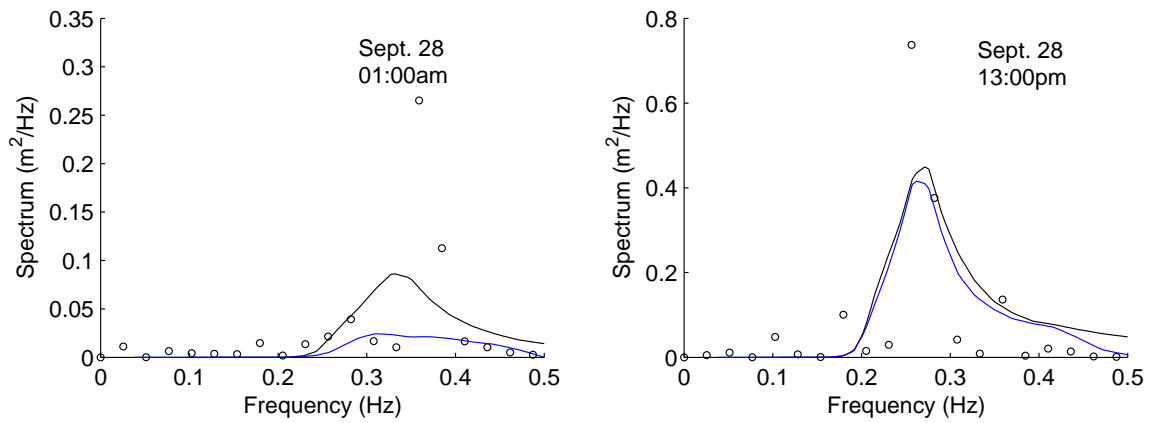


Figure 5.5: Frequency spectrum at different times in 1997. Black line: spatially uniform wind fields without current fields; Blue line: spatially uniform wind fields with current fields; Black circles: measured data

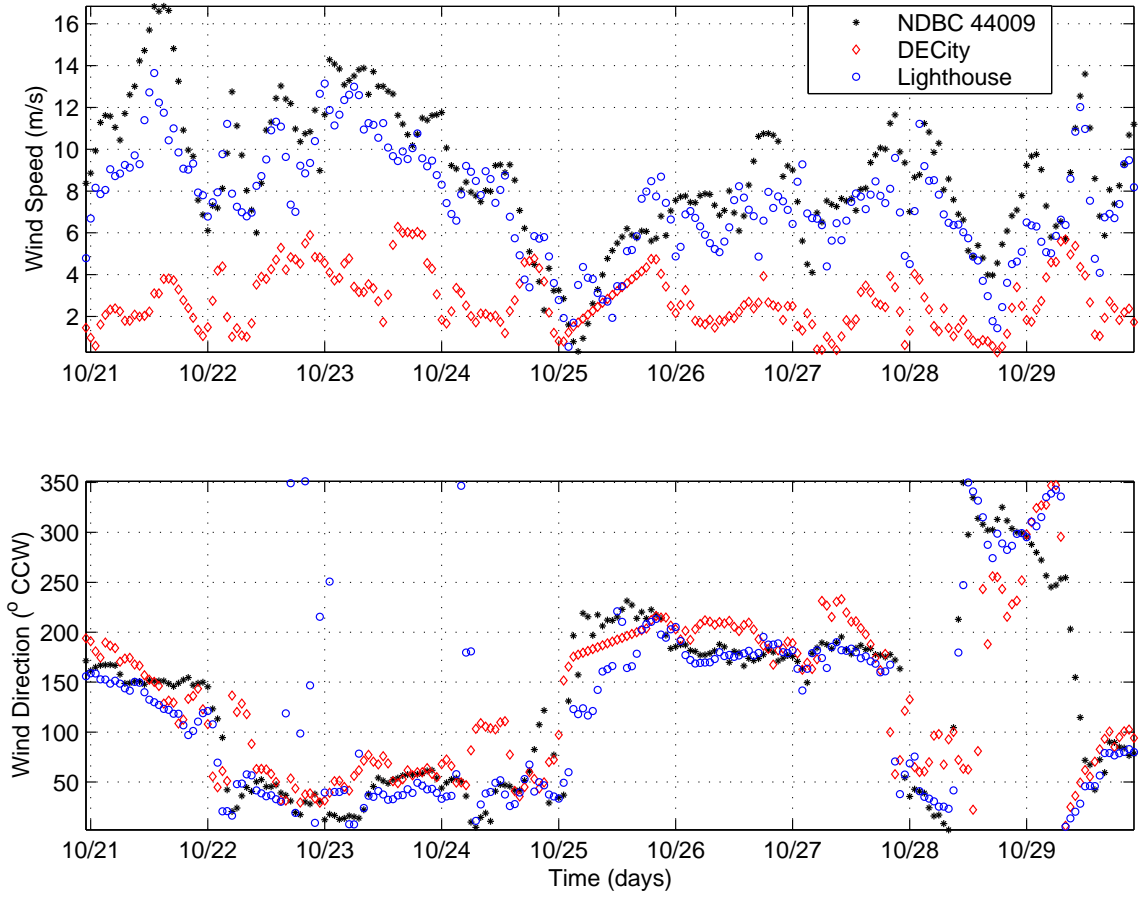


Figure 5.6: Recorded wind speed and direction at three locations: NOAA buoy station (black star); Delaware City (red diamond); Fourteen Ft. Bank Lighthouse (blue circle) during 23:00 October 20 through 22:00 October 29, 2003

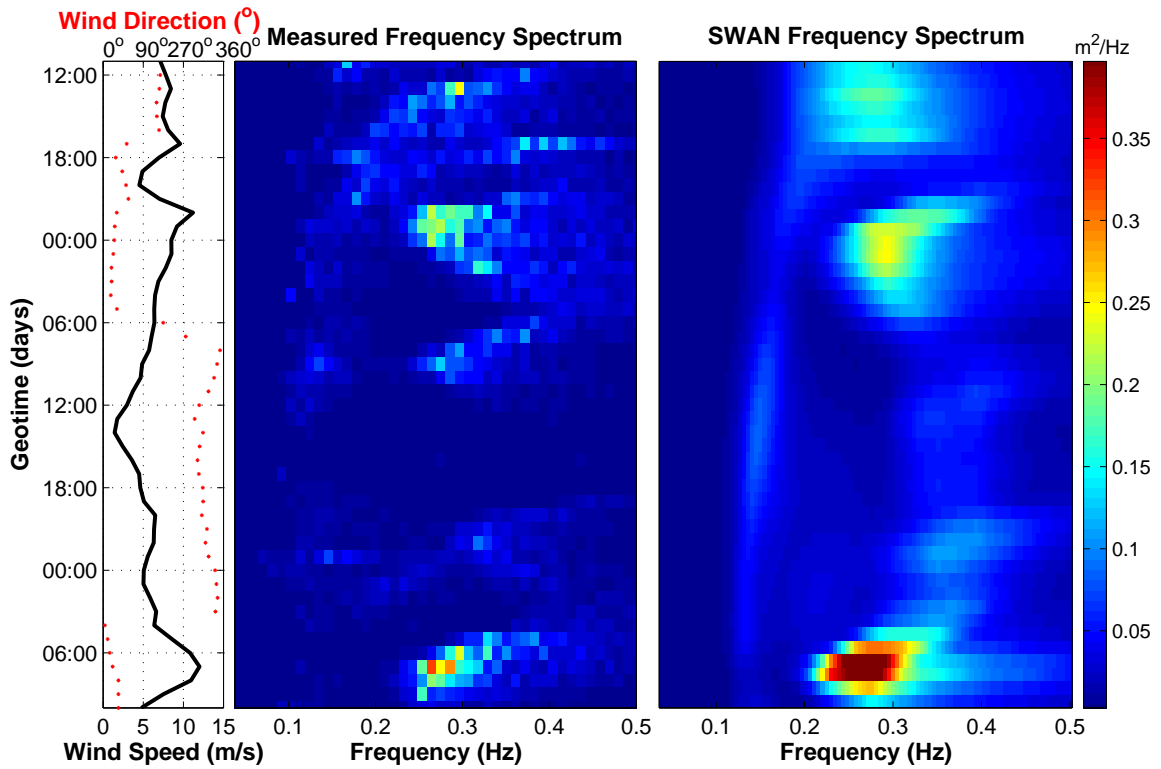


Figure 5.7: Left panel: Recorded wind speed (black solid line) and direction (red points, CCW) during 11:00 October 27 through 10:00 October 29, 2003 at Fourteen Ft. Bank Lighthouse; Middle panel: Frequency spectrum from WSB; Right panel: Frequency spectrum from SWAN simulation with uniform wind field

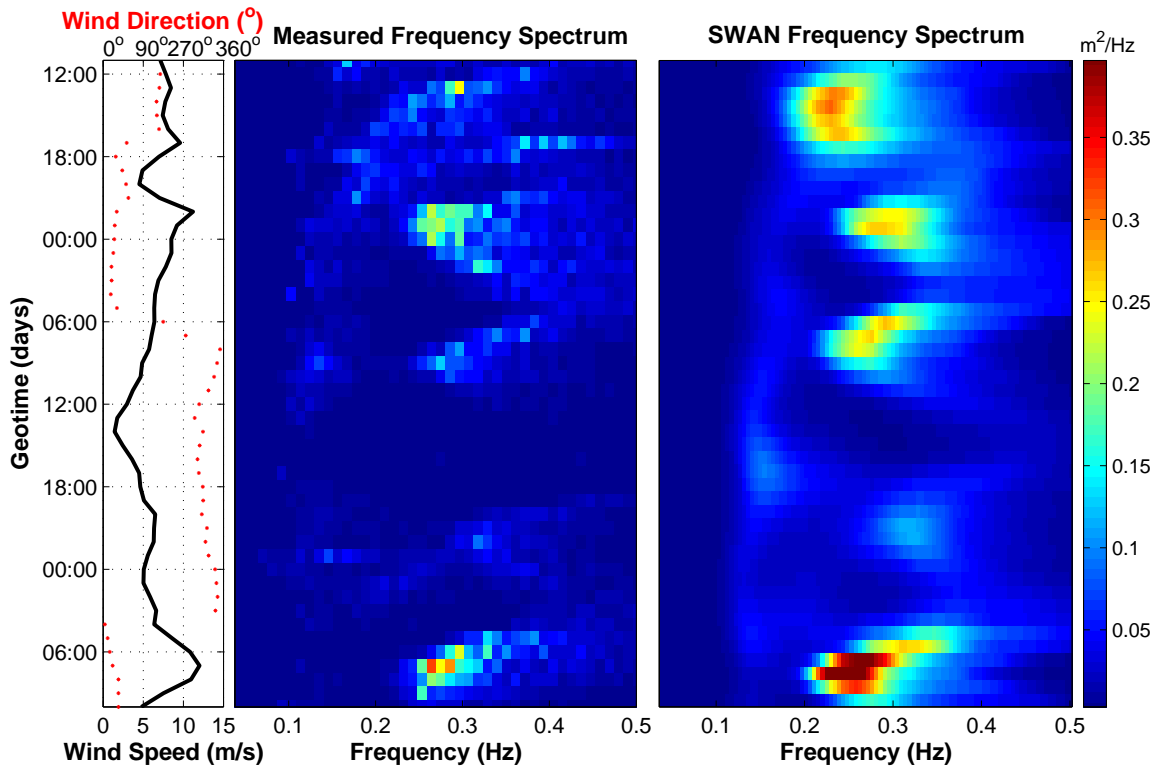


Figure 5.8: Left panel: Recorded wind speed (black solid line) and direction (red points, CCW) during 11:00 October 27 through 10:00 October 29, 2003 at Fourteen Ft. Bank Lighthouse; Middle panel: Frequency spectrum from WSB; Right panel: Frequency spectrum from SWAN simulation with uniform wind field and current fields from ROMS

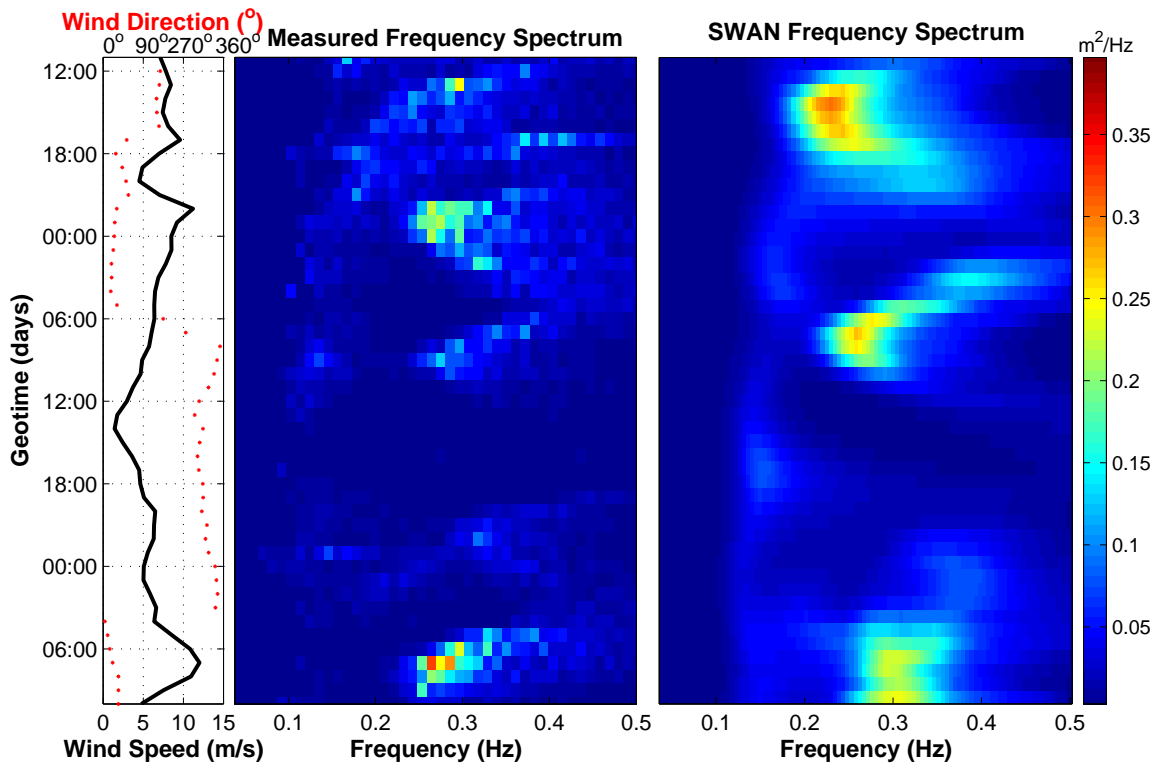


Figure 5.9: Left panel: Recorded wind speed (black solid line) and direction (red points, CCW) during 11:00 October 27 through 10:00 October 29, 2003 at Fourteen Ft. Bank Lighthouse; Middle panel: Frequency spectrum from WSB; Right panel: Frequency spectrum from SWAN simulation with variable wind field and current fields from ROMS

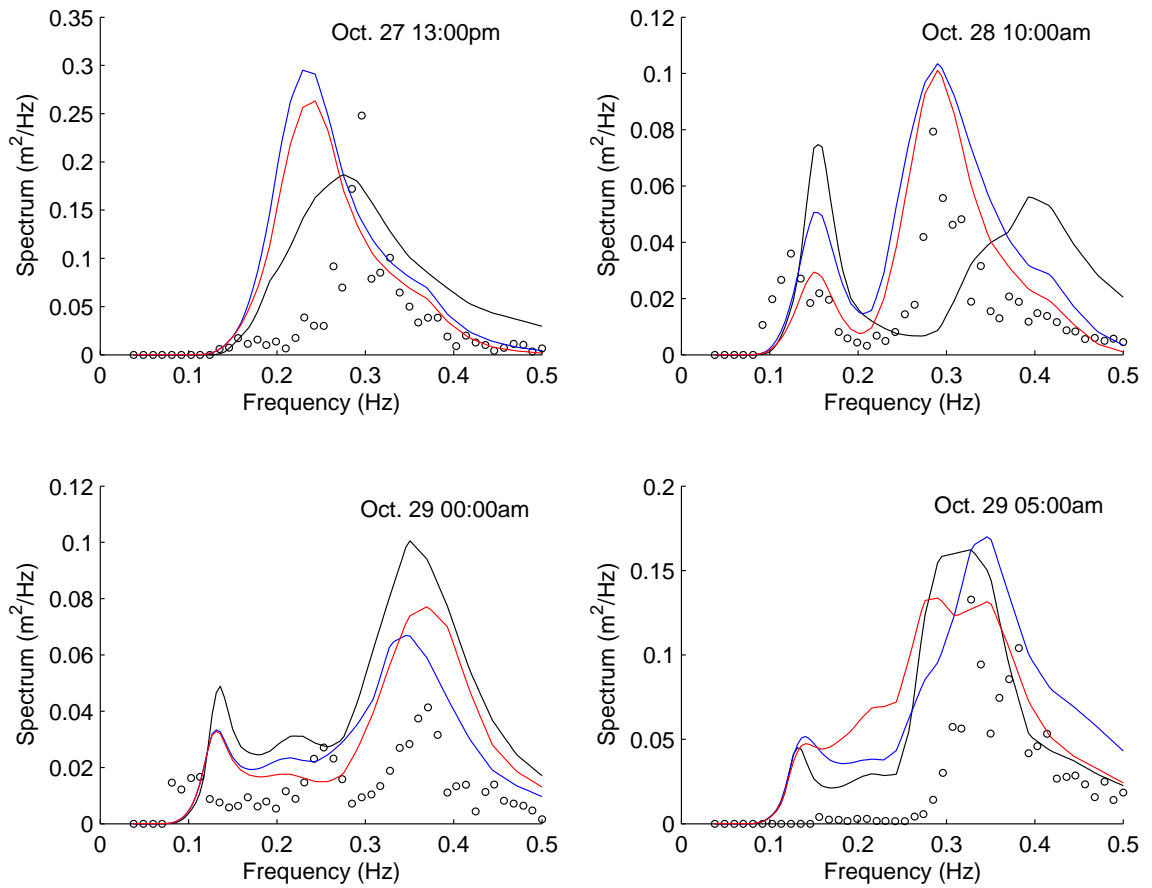


Figure 5.10: Frequency spectrum at different times in 2003. Black line: spatially uniform wind fields; Blue line: spatially uniform wind fields and current fields; Red line: spatially variable wind fields and current fields; Black circles: measured data by WSB

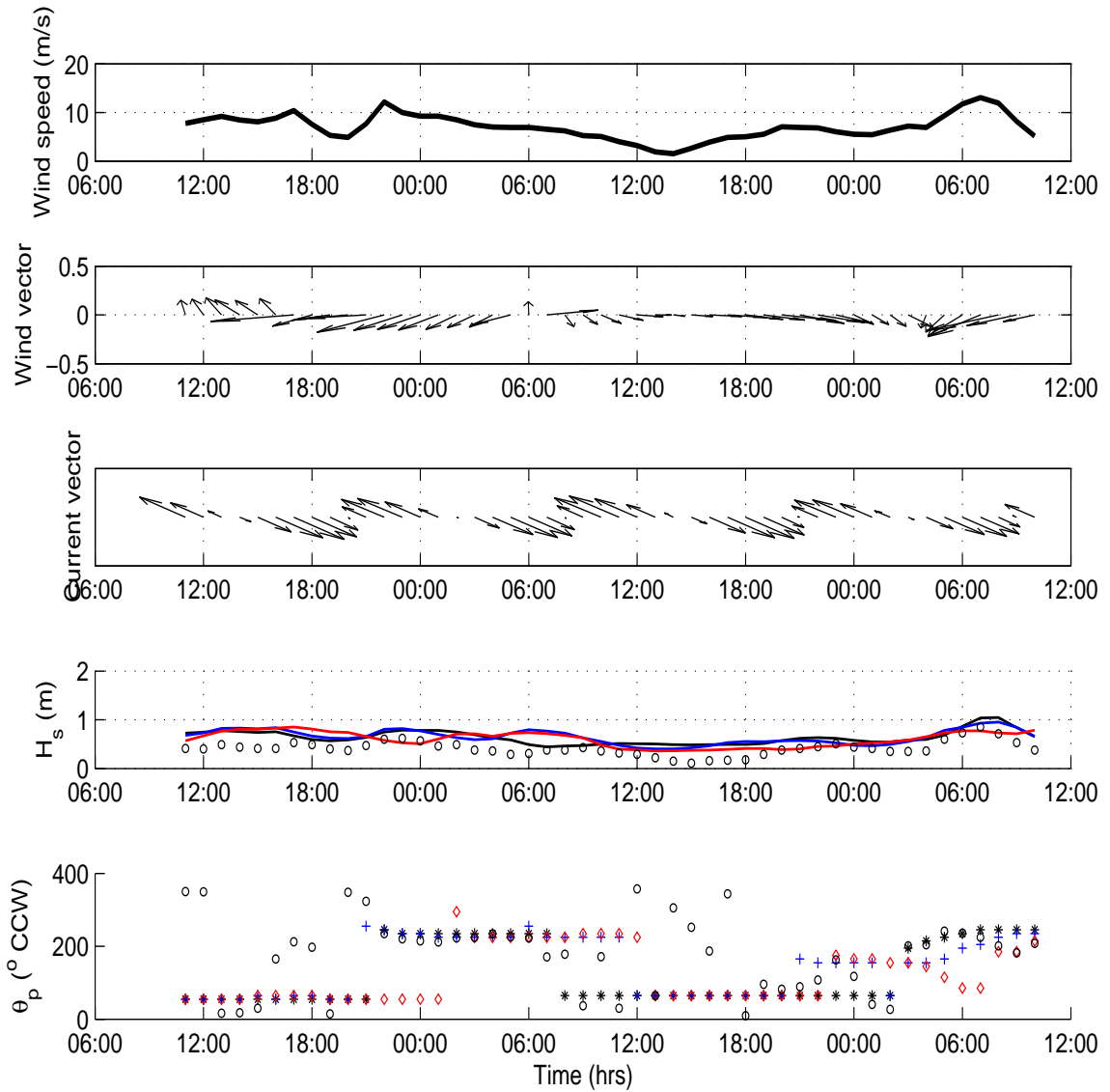


Figure 5.11: Comparison of H_s and θ_p with different wind fields and current fields during 11:00 October 27 through 10:00 October 29, 2003 at Fourteen Ft. Bank Lighthouse. First panel: wind speed; Second panel: wind vector; Third panel: current panel; Fourth panel: H_s with uniform wind field only (black line), with uniform wind field and current field (blue line) and with variable wind field and current field (red line); Fifth panel: θ_p with uniform wind field only (black stars), with uniform wind field and current field (blue crosses) and with variable wind field and current field (red diamonds). The black circles are the values measured by WSB.

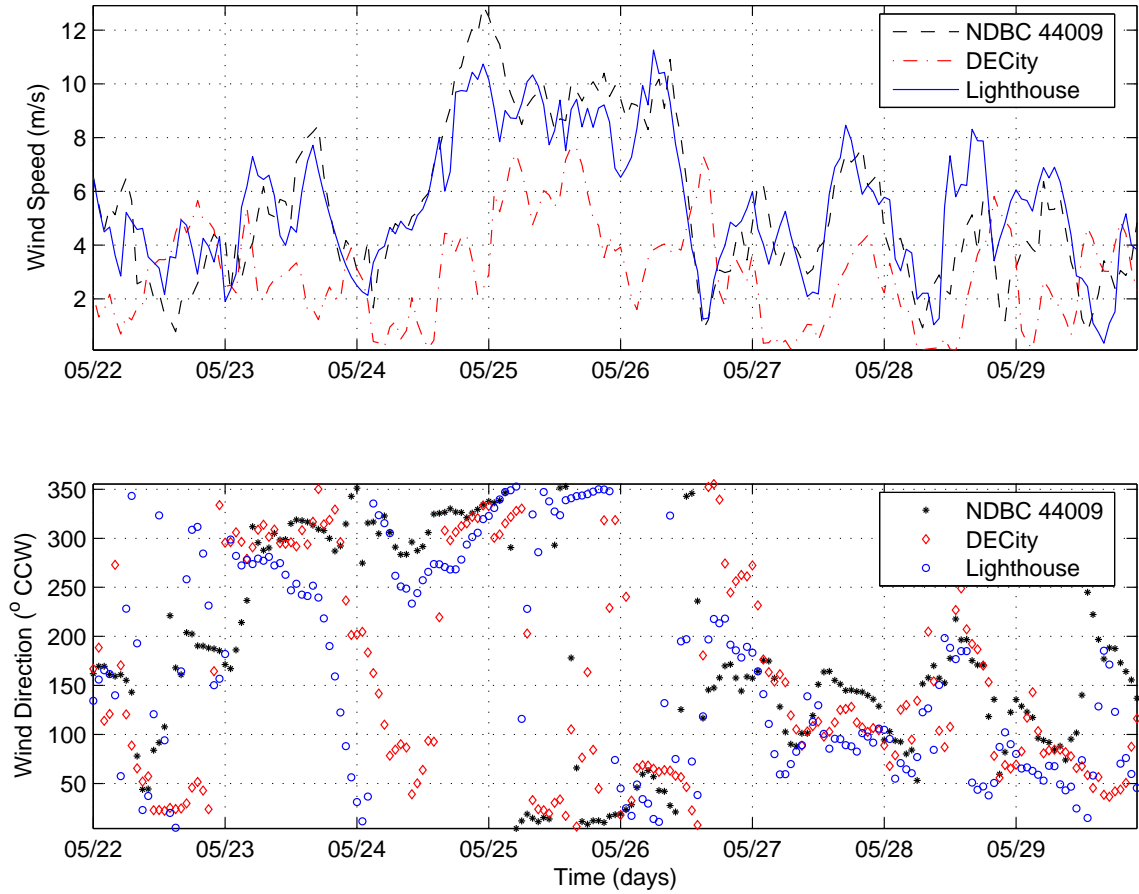


Figure 5.12: Recorded wind speed and direction at three stations: NDBC 44009 (black star); Delaware City (red diamond); Fourteen Ft. Bank Lighthouse (blue circle) during 00:00 May 22 through 23:00 May 29, 2005

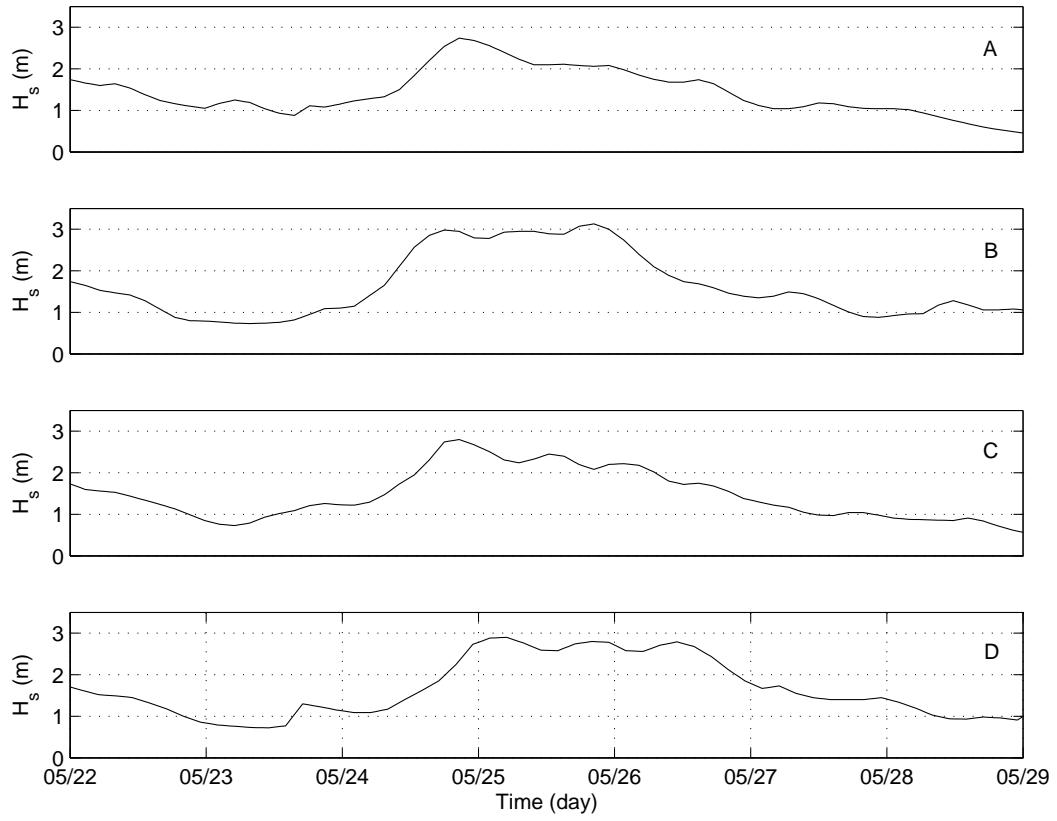


Figure 5.13: Significant wave height at points *A*, *B*, *C* and *D* at seaward boundary from WWII in 2005

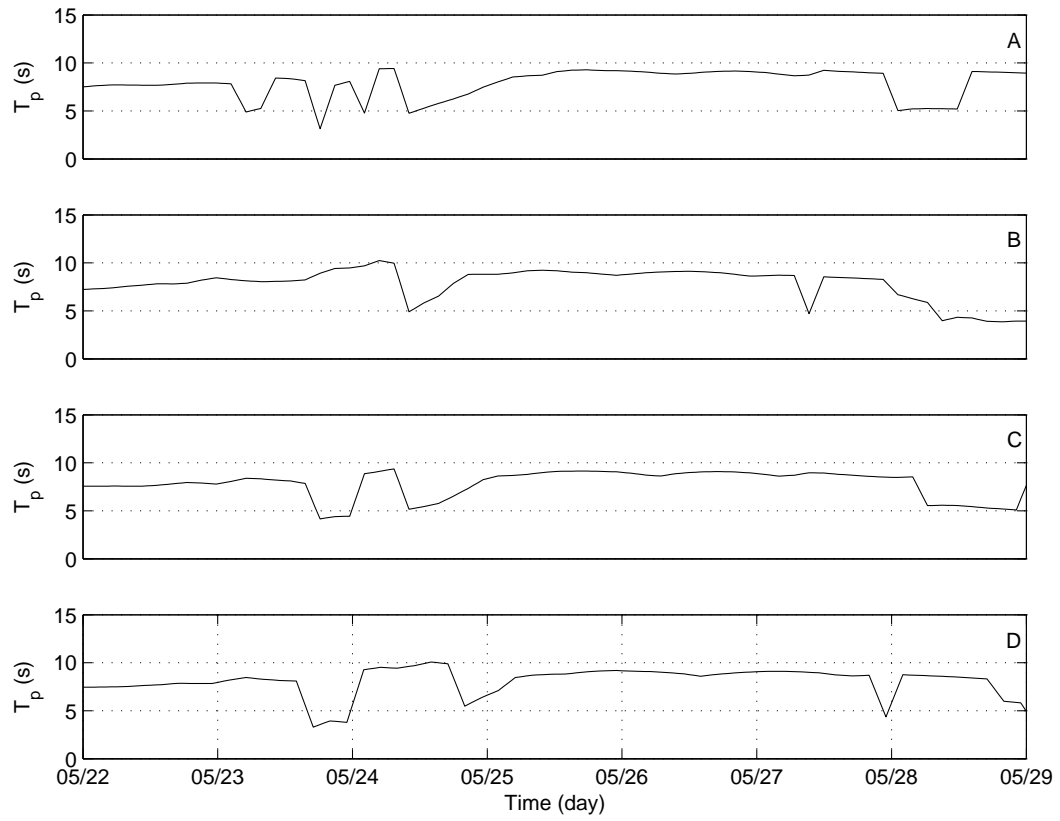


Figure 5.14: Peak period at points *A*, *B*, *C* and *D* at seaward boundary from WWIII in 2005

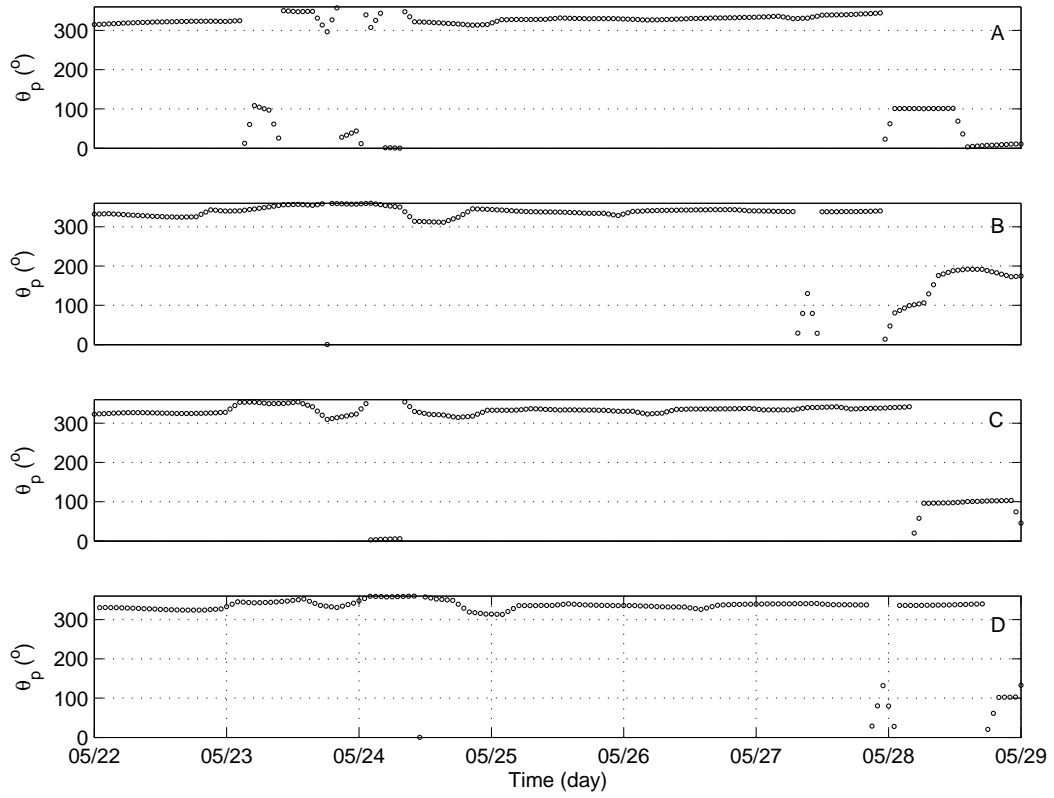


Figure 5.15: Peak direction (CCW) at points *A*, *B*, *C* and *D* at seaward boundary from WWIII in 2005

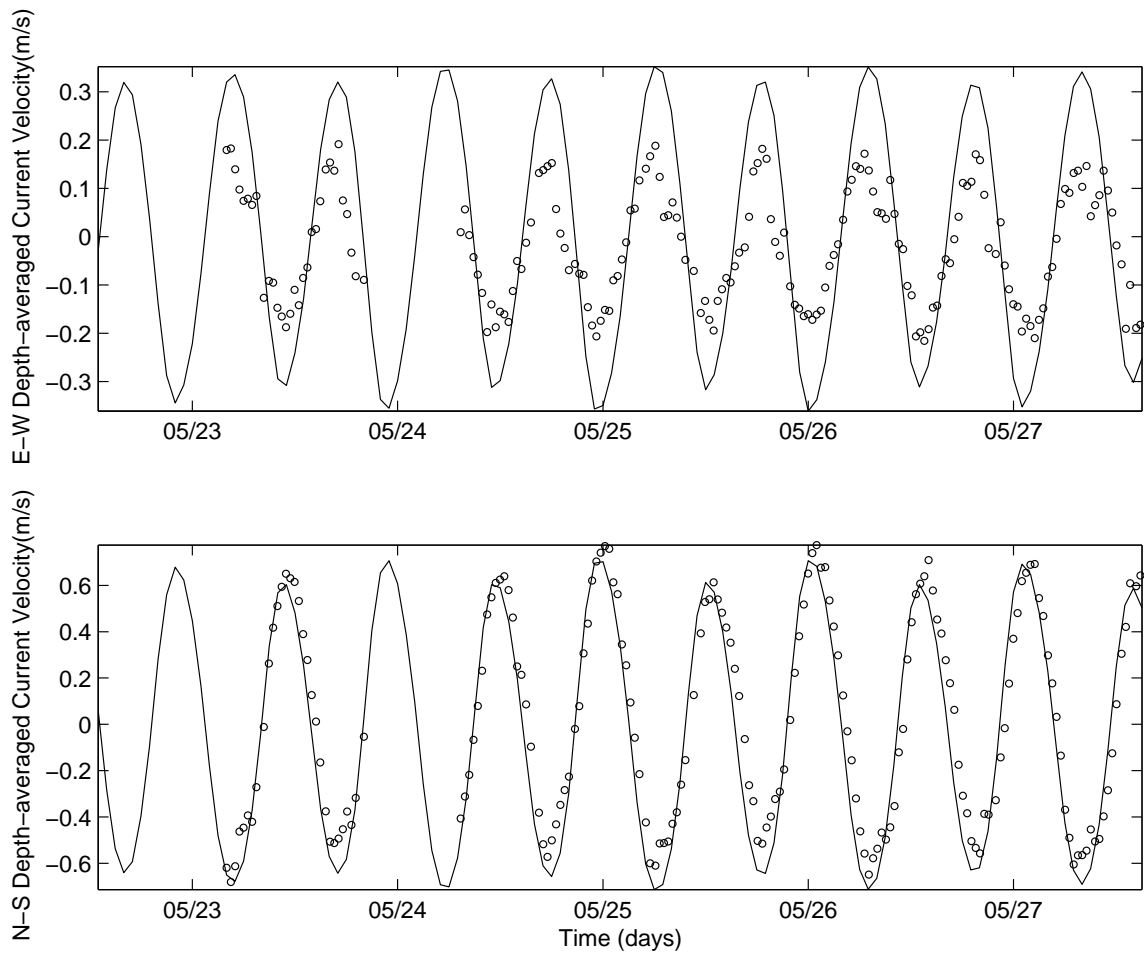


Figure 5.16: Comparison of depth-averaged current velocity between measurement of ADCP (circle) and ROMS (solid line) at measuring station in May, 2005. Positive values point to east and north.

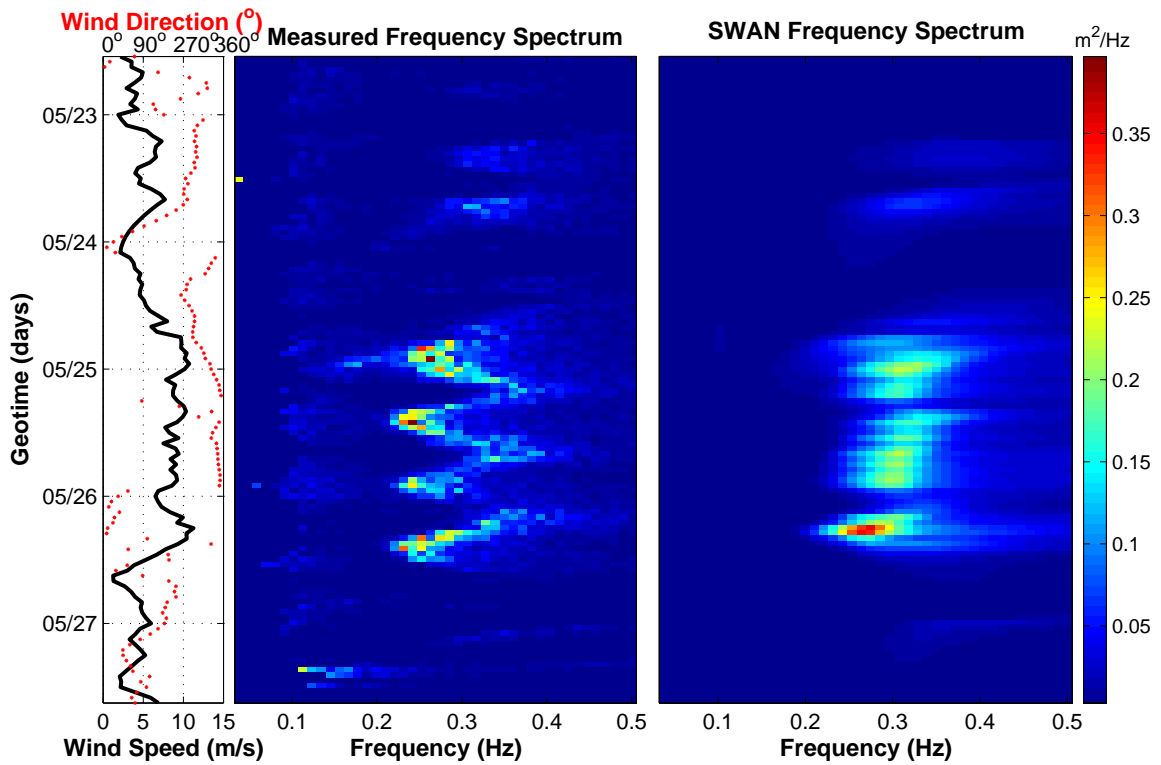


Figure 5.17: Left panel: Recorded wind speed (black solid line) and direction (red points, CCW) during 13:00 May 22 through 15:00 May 27, 2005 at Fourteen Ft. Bank Lighthouse; Middle panel: Frequency spectrum from WSB; Right panel: Frequency spectrum from SWAN simulation with uniform wind field

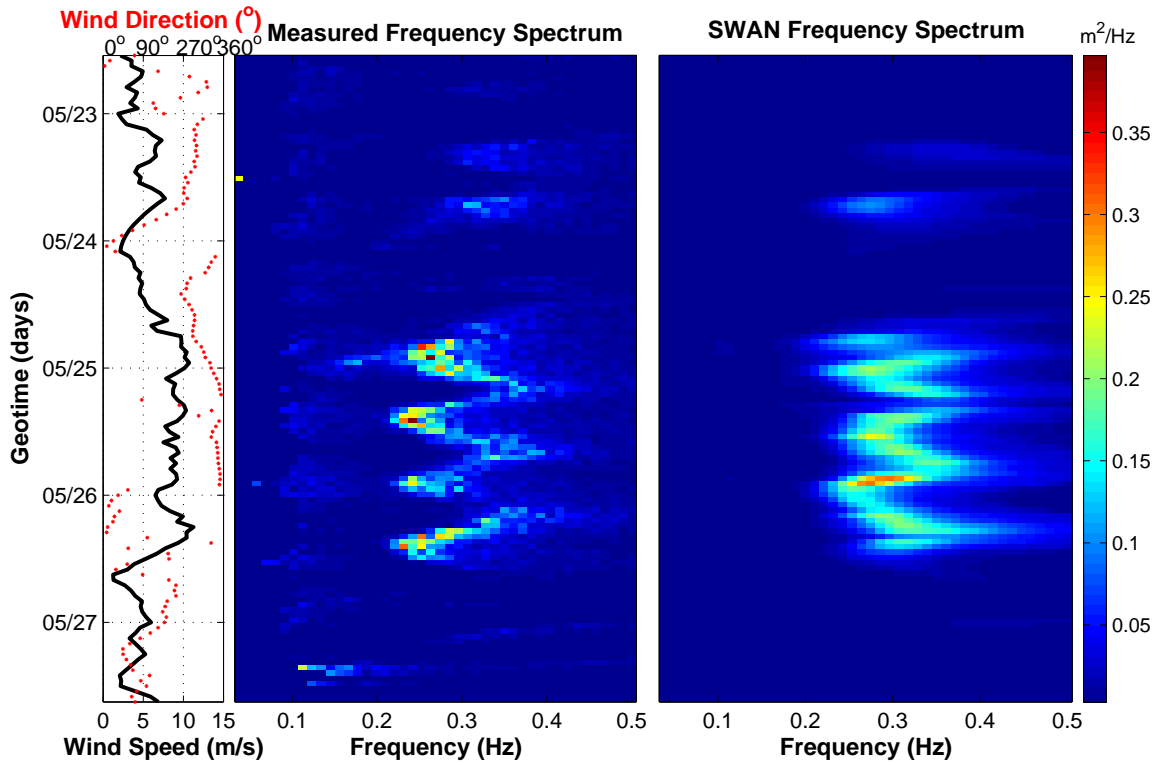


Figure 5.18: Left panel: Recorded wind speed (black solid line) and direction (red points, CCW) during 13:00 May 22 through 15:00 May 27, 2005 at Fourteen Ft. Bank Lighthouse; Middle panel: Frequency spectrum from WSB; Right panel: Frequency spectrum from SWAN simulation with uniform wind field and current fields from ROMS

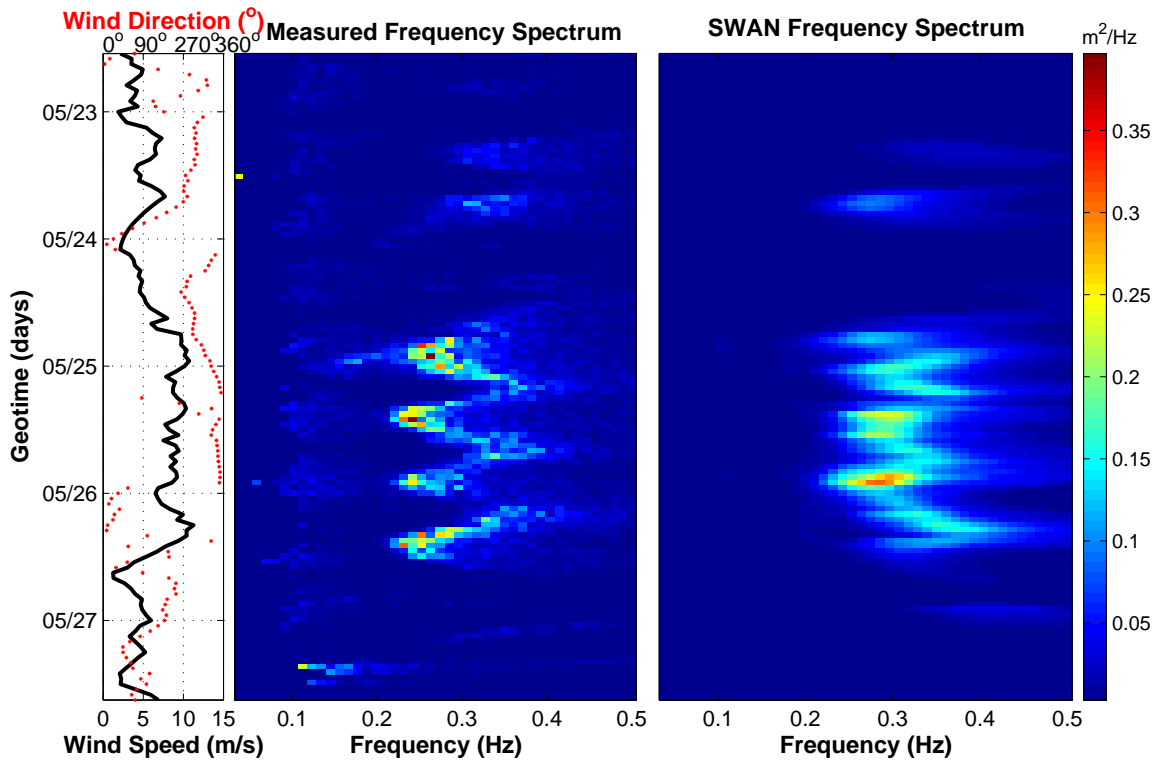


Figure 5.19: Left panel: Recorded wind speed (black solid line) and direction (red points, CCW) during 13:00 May 22 through 15:00 May 27, 2005 at Fourteen Ft. Bank Lighthouse; Middle panel: Frequency spectrum from WSB; Right panel: Frequency spectrum from SWAN simulation with variable wind field and current fields from ROMS

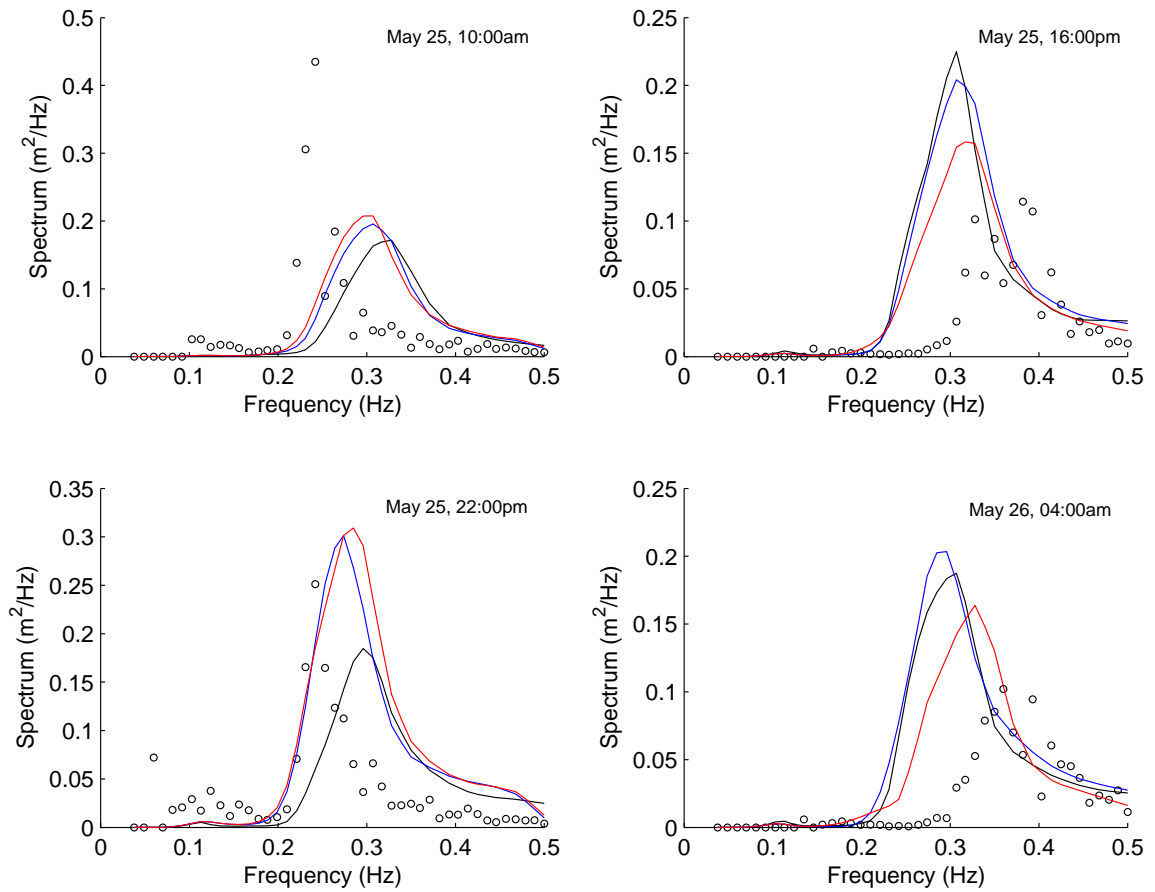


Figure 5.20: Frequency spectrum at different times in 2005. Black line: spatially uniform wind fields; Blue line: spatially uniform wind fields and current fields; Red line: spatially variable wind fields and current fields; Black circles: measured data by WSB

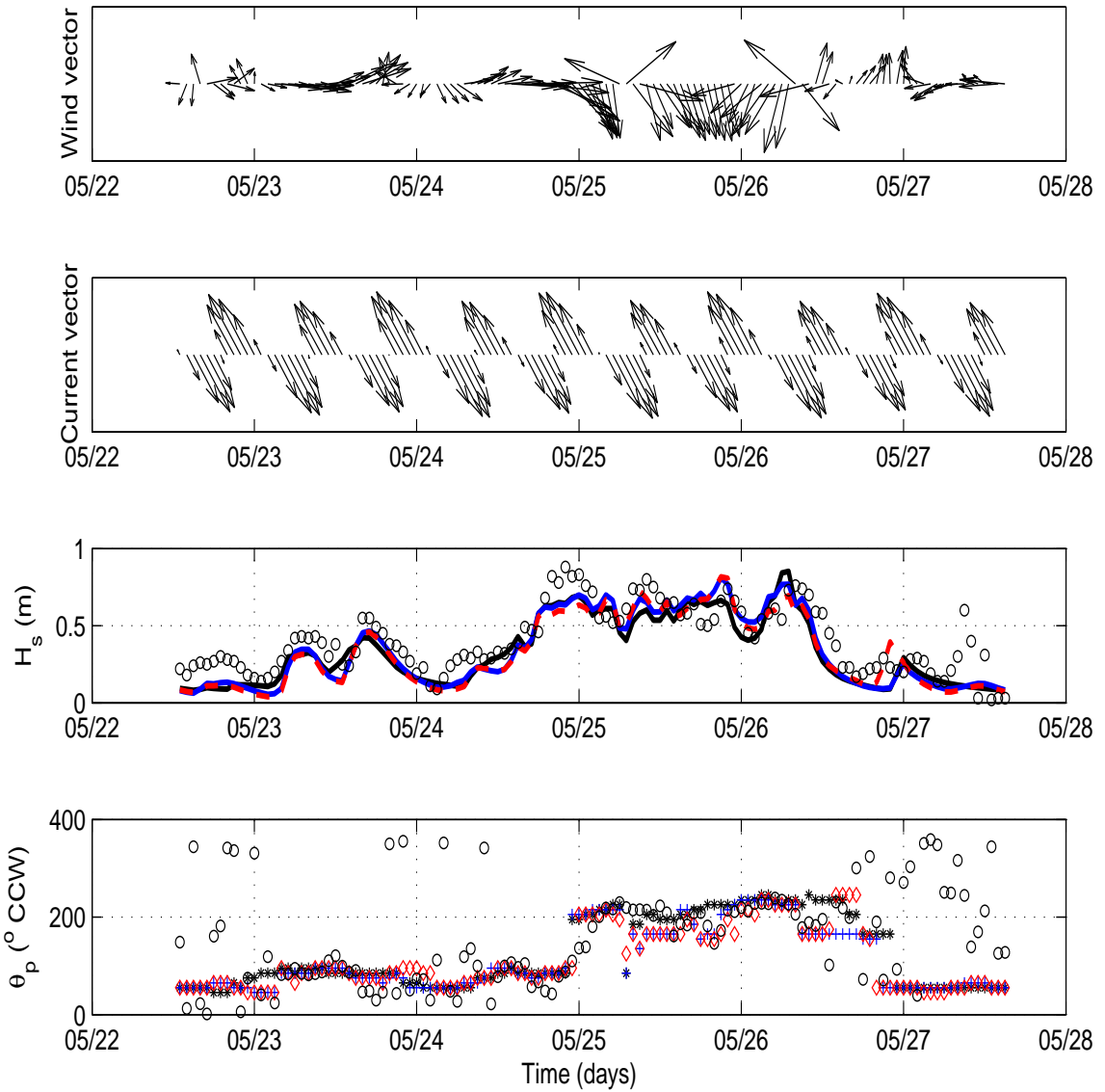


Figure 5.21: First panel is the wind vector recorded at Fourteen Ft. Bank Lighthouse during May 22 through May 27, 2005; Second panel shows the current vector at the measured station calculated by ROMS; Third panel shows H_s with uniform wind field only (black solid line), with uniform wind field and current field (blue solid line) and with variable wind field and current field (red dash line); Fourth panel shows θ_p with uniform wind field only (black stars), with uniform wind field and current field (blue crosses) and with variable wind field and current field (red diamonds). The black circles are the values measured by WSB.

Chapter 6

CONCLUSION

6.1 Conclusion

The purpose of this study was to apply the wind wave generation model SWAN to simulate the generation of fetch-limited wind waves with ambient current in the Delaware Bay.

First, a brief description of SWAN was presented. Then SWAN model was set up for Delaware Bay. The model domain included the entire Delaware estuary and the adjacent continental shelf. The bathymetry was based on an orthogonal curvilinear grid. Physical processes included wave shoaling, refraction, nonlinear interactions, depth-induced breaking, wave-current interaction, and bottom friction and whitecapping dissipation. The seaward boundary condition was specified by the wave parameters from WWIII.

Two kinds of wind field distribution were constructed. First, a uniform wind field was constructed by using wind speed and direction recorded at Fourteen Ft. Bank Lighthouse throughout the whole model domain. Then a spatially variable wind field was constructed by interpolating three stations, which located at upper bay, middle bay and outside bay respectively.

In order to take into account the interaction between the waves and currents, the coupling of ROMS and SWAN models was developed. The traditional file *I/O* method was used to couple ROMS and SWAN in this study. First, ROMS was driven by the tide at the seaward boundary. The depth-averaged current velocities

calculated by ROMS were stored in files for the desired periods, which are used as input files for SWAN.

Three sets of field measurement data were used to test SWAN simulation results. One experiment was conducted in Delaware Bay in September 1997 to investigate acoustic fluctuations and environmental parameters. The sea surface elevation and spectrum were measured using an inverted echo sounding technique. In 2003 and 2005, WSB was deployed to measure the surface at the same site as the experiment in 1997. SWAN simulations during these periods were compared the field data for significant wave height, peak period, dominant direction and frequency spectrum.

SWAN simulation is sensitive to the wind field distribution. For the particular measuring location at Fourteen Ft. Bank Lighthouse, the difference between uniform and variable wind fields does not change H_s and T_p significantly. Both H_s and T_p are affected due to the change of the wind field in the upper bay and the ocean shelf. So it is important to use a reliable wind field in simulation.

SWAN simulation is sensitive to current fields too. Since the current on the ocean shelf is small, it almost does not affect H_s and T_p . In the bay, the strong current affects the wave propagation, especially in the upper bay and the mouth of the bay.

Both SWAN and ROMS simulations were compared with measured data. The simulated current velocities from ROMS at the measuring station were compared to the ADCP data. The north-south current velocity agreed well with the measured data. The simulated east-west current velocity was underestimated in 1997 case, while it was overestimated in 2003 and 2005 cases.

Comparing SWAN results with the three sets of experimental data, it was found that both the uniform wind field and the spatially variable wind field overestimated the significant wave height at the Fourteen Ft. Bank Lighthouse measuring

station in some period of 1997 case and 2003 case. But they were underestimated slightly in 2005 case. H_s was affected by the change of the fetch due to the change of the wind distribution. θ_p did not change much due to different wind field distributions. The waves were clearly modulated by currents according to the frequency spectrum. The coupling model of ROMS and SWAN helps in showing better comparison between the modeled and the measured data. Hence, the coupling model of ROMS and SWAN with a suitable wind field should be used to simulate the wave propagation and transformation in Delaware Bay.

6.2 Suggestions for Future Work

In this study, the spatially variable wind field was constructed by interpolating three stations along x -direction in the simulation domain. The wind was still assumed to be uniform in the y -direction. It might be better to use a more realistic spatially variable wind field. It is suggested to collect wind information at more measuring stations throughout the simulation domain. Otherwise, the wind can be generated by the weather prediction model.

The offshore boundary data should be applied at a greater number of shorter segments. And lateral boundary should be treated realistically.

Since currents play an important role in SWAN simulation, it is worthwhile to develop an automated model coupling system to couple SWAN and ROMS and share the information through a server. SWAN can get current information from ROMS. At the same time, ROMS can get wave information from SWAN.

BIBLIOGRAPHY

- [1] Abbott, M.B. and D.R. Basco, "Computational fluid dynamics: an introduction for engineers", Wiley, New York, N.Y. (1989)
- [2] Alkyon and Delft Hydraulics, SWAN fysica plus, report H3937/A832 (2002)
- [3] Badiey, M., Y. Mu, J.A. Simmen, S.E. Forsythe, "Signal variability in shallow-water sound channels", IEEE Journal of Oceanic Engineering, 25: 492-500 (2000)
- [4] Badiey M., K.C. Wong, L. Lenain, "High-frequency acoustic propagation in the presence of oceanographic variability", Proceeding NATO Saclant Undersea Research Center, Roma (2002)
- [5] Battjes, J.A., "Shallow water wave modelling", Proc. Intern. Symp. on WAVES-Phys. and Num. Modelling, IAHR, Vancouver, 1-23 (1994)
- [6] Battjes, J.A. and J.P.F.M. Janssen, "Energy loss and set-up due to breaking of random waves", Proc. 16th Int. Conf. Coastal Engineering, ASCE, 569-587 (1978)
- [7] Black, K., D. Hatton and M. Rosenberg, "Locally and externally-driven dynamics of a large semi-enclosed bay in southern Australia", Journal of Coastal Research 9(2): 509-538 (1993)
- [8] Black, K.P., "Sediment transport and tidal inlet hydraulics", D.Phil. Thesis, University of Waikato. New Zealand, Hamilton, Volume 1, Text, 331pp. Volume 2, Figures and Tables (1983)
- [9] Bretherton, F.P. and C.J.R. Garrett, "Wavetrains in inhomogeneous moving media", Proc. Roy. Soc. A. 302: 529-554 (1969)
- [10] Booij, N., R.C. Ris and L.H. Holthuijsen, "A third generation wave model for coastal regions 1. Model description and validation", J. Geophys. Res., 104, C4: 7649-7666 (1999)
- [11] Cavaleri, L. and P. Malanotte-Rizzoli, "Wind wave prediction in shallow water: Theory and application", J. Geophys. Res., 86, C11: 10961-10973 (1981)

- [12] Chen, Q., K.L. Hu, H.H. Zhao, and S.L. Douglass, "Prediction of wind waves in a shallow estuary", *Journal of Waterway, Port, Coastal and Ocean Engineering*, 131, 4: 137-148 (2005)
- [13] Collins, J.I., "Prediction of shallow water spectra", *J. Geophys. Res.*, 77, 15: 2693-2707 (1972)
- [14] Dingemans, M.W., "Water wave propagation over uneven bottoms. Part 1 linear wave propagation", *Advanced Series on Ocean Engineering*, 13, World Scientific, 471 p. (1997)
- [15] Earle, M.D., Steele, K.E. and D.W.C. Wang, "Use of advanced directional wave spectra analysis methods", *Ocean Engineering*, 26: 1421-1434 (1999)
- [16] Eldeberky, Y. and J.A. Battjes, "Spectral modeling of wave breaking: Application to Boussinesq equations", *J. Geophys. Res.*, 102: 1253-1264 (1996)
- [17] Erickson, D.J., "A stability dependent theory for air-sea exchange", *Journal of Geophysics Research* 98: 8417-8488 (1993)
- [18] Golub, G.H. and C.F. van Loan, "Matrix Computations", 476 p., Academic, San Diego, Calif. (1986)
- [19] Gorman, R.M. and C.G. Neilson, "Modelling shallow water wave generation and transformation in an intertidal estuary", *Coastal Engineering*, 36: 197-217 (1999)
- [20] Günther, H., S. Hasselmann and P.A.E.M. Janssen, "The WAM Model Cycle 4.0", *Deutsch. Klim. Rechenzentrum, Techn. Rep. No. 4*, Hamburg, Germany (1992)
- [21] Haidvogel, D.B., H.G. Arango, K. Hedstrom, A. Beckmann, P. Malanotte-Rizzoli, and A.F. Shchepetkin, "Model evaluation experiments in the North Atlantic Basin: Simulations in nonlinear terrain-following coordinates", *Dynamics of Atmospheres and Oceans*, 32: 239-281 (2000)
- [22] Hasselmann, K., T.P. Barnett, E. Bouws, H. Carlson, D.E. Cartwright, K. Enke, J.A. Ewing, H. Gienapp, D.E. Hasselmann, P. Kruseman, A. Meerburg, P. Mller, D.J. Olbers, K. Richter, W. Sell and H. Walden, "Measurements of wind-wave growth and swell decay during the Joint North Sea Wave Project (JONSWAP)", *Dtsch. Hydrogr. Z. Suppl.*, 12, A8 (1973)
- [23] Hasselmann, S. and K. Hasselmann, "A symmetrical method of computing the non-linear transfer in a gravity-wave spectrum", *Hamburger Geophys. Einzelschr., Serie A.*, 52, 8 (1981)

- [24] Hasselmann, S., K. Hasselmann, J.H. Allender, and T.P. Barnett, “Computations and parameterizations of the linear energy transfer in a gravity wave spectrum, II, Parameterizations of the nonlinear transfer for application in wave models”, *J. Phys. Oceanogr.*, 15: 1378-1391 (1985)
- [25] Heitsenrether, R.M., “The influence of fetch limited sea surface roughness on high frequency acoustic propagation in shallow water”, Master’s Thesis, University of Delaware (2004)
- [26] Holthuijsen, L.H., N. Booij, R.C. Ris, I.J.G. Haagsma, A.T.M.M. Kieftenburg, E.E. Kriez, M. Zijlema, A.J. van der Westhuysen, “SWAN Cycle III version 40.31, User manual”, Department of Civil Engineering, Delft University of Technology, the Netherlands, February 5 (2004)
- [27] Janssen, P.A.E.M., “Wave induced stress and the drag of air flow over sea waves”, *J. Phys. Oceanogr.*, 19, 745-754 (1989)
- [28] Janssen, P.A.E.M., “Quasi-linear theory of wind-wave generation applied to wave forecasting”, *J. Phys. Oceanogr.*, 21: 1631-1642 (1991a)
- [29] Janssen, P.A.E.M., “Consequences of the effect of surface gravity waves on the mean air flow, paper presented at breaking waves”, *Int. Union of Theor. and Appl. Mech.*, Sydney, Australia (1991b)
- [30] Jonsson, I.G., “Wave boundary layers and friction factors”, *Proc. 10th Int. Conf. Coastal Engineering*, ASCE, 127-148 (1966)
- [31] Jonsson, I.G., “A new approach to rough turbulent boundary layers”, *Ocean Engineering*, 7: 109-152 (1980)
- [32] Jonsson, I.G. and N.A. Carlsen, “Experimental and theoretical investigations in an oscillatory turbulent boundary layer”, *J. Hydraulic Research*, 14: 45-60 (1976)
- [33] Johnson, H.K., “Simple expressions for correcting wind speed data for elevation”, *Coastal Engineering*, 36: 263-269 (1999)
- [34] Kahma, K.K. and C.J. Calkoen, “Reconciling discrepancies in the observed growth of wind-generated waves”, *J. Phys. Oceanogr.*, 22: 1389-1405 (1992)
- [35] Komen, G.J., S. Hasselmann, and K. Hasselmann, “On the existence of a fully developed wind-sea spectrum”, *J. Phys. Oceanogr.*, 14: 1271-1285 (1984)
- [36] Lalbeharry, R. “Comparison of the performances of three state-of-the-art ocean wave models in extreme storm cases”, *Proc. 7th Int. Workshop on Wave Hind-casting and Forecasting*, Banff, Alberta, October 21-25 (2002)

- [37] Lalbeharry, R., A. Behrens, H. Guenther and L. Wilson, “An evaluation of wave model performances with linear and nonlinear dissipation source terms in lake Erie”, 8th International Workshop on Wave Hindcasting and Forecasting, North Shore, Oahu, Hawaii, November 14-19 (2004)
- [38] Large, W.G. and S. Pond, “Sensible and latent heat flux measurements over the ocean”, *J. Phys. Oceanogr.*, 12: 464-482 (1982)
- [39] Lenain, L., “Characteristics of broadband high-frequency acoustic propagation in coastal environment”, Master’s Thesis, University of Delaware (2002)
- [40] Li, C.W. and M. Mao, “Spectral modelling of typhoon-generated waves in shallow waters”, *J. Hydraul. Res.*, 30: 611-622 (1992)
- [41] Lin, W.Q., L.P. Sanford and S.E. Suttles, “Wave measurement and modelling in Chesapeake Bay”, *Continental Shelf Research*, 22: 2673-2686 (2002)
- [42] Madsen, O.S., Y.-K. Poon and H.C. Graber, “Spectral wave attenuation by bottom friction: Theory”, *Proc. 21th Int. Conf. Coastal Engineering, ASCE*, 492-504 (1988)
- [43] Monbaliu, J., R. Padilla-Hernández, J.C. Hargreaves, J.C.C. Albiach, W. Luo, W. Sclavo, H. Günther, “The spectral wave model, WAM, adapted for application with high spatial resolution”, *Coastal Engineering*, 41: 41-62 (2000)
- [44] Monin, A.S. and A.M. Obukhov, “Basic law of turbulent mixing in the atmosphere near the ground”, *Transactions: Akad. Nauk SSSR Geofiz. Inst., Trudy* 24: 163-187 (1954)
- [45] Padilla-Hernández R., W. Perrie, B. Toulany, P.C. Smith, W. Zhang and S. Jiménez-Hernández, “Intercomparison of modern operational wave models”, 8th International Workshop on Wave Hindcasting and Forecasting, North Shore, Oahu, Hawaii, November 14-19 (2004)
- [46] Pierson, W.J. and L. Moskowitz, “A proposed spectral form for fully developed wind seas based on the similarity theory of S.A. Kitaigorodskii”, *J. Geophys. Res.*, 69, 24: 5181-5190 (1964)
- [47] Pires-Silva, A. A., O. Makarynsky, J. Monbaliu, C. Ventura-Soares and E. Coelho, “Wam/Swan simulation in an open coast: Comparisons with ADCP measurements”, *Littoral 2002, The Changing Coast. EUROCOAST / EUCC, Porto-Portugal Ed. EUROCOAST-Portugal, ISBN 972-8558-09-0. 169-173* (2002)

- [48] Richard, M.G. and C.G. Neilson, “Modelling shallow water wave generation and transformation in an intertidal estuary”, *Coastal Engineering*, 36: 197-217 (1999)
- [49] Ris R.C., L.H. Holthuijsen and N. Booij, “A third-generation wave model for coastal regions 2. Verification”, *J. Geophys. Res.*, 104, C4: 7667-7681 (1999)
- [50] Rogers, W.E., P.A. Hwang and D.W. Wang, “Investigation of wave growth and decay in the SWAN model: three regional-scale applications”, *Journal of Physical Oceanography*, 33, 2: 366-389 (2002)
- [51] Rusu, E., C.V. Soares, A.P. Silva, J.P. Pinto and O. Makarynskiy, “Near real time assessment of the wave propagation in the coastal environment of Portugal”, *Littoral 2002, The Changing Coast. EUROCOAST / EUCC, Porto-Portugal Ed. EUROCOAST-Portugal*, ISBN 972-8558-09-0. 175-184 (2002)
- [52] Shchepetkin, A.F. and J.C. McWilliams, “The regional ocean modeling system: a split-explicit, free surface, topography-following coordinate ocean model”, *Ocean Modelling*, 9: 347-404 (2005)
- [53] Song, Y.T. and D.B. Haidvogel, “A semi-implicit ocean circulation model using a generalized topography following coordinate system”, *J. Comp. Phys.*, 115: 228-248 (1994)
- [54] Tolman, H.L. “A third-generation model for wind waves on slowly varying, unsteady and inhomogeneous depths and currents”, *J. Phys. Oceanogr.*, 21: 782-797 (1991)
- [55] Tolman, H.L. “Effects of numerics on the physics in a third-generation wind-wave model”, *J. Phys. Oceanogr.*, 22: 1095-1111 (1992a)
- [56] U.S. Army Corps of Engineers, “Shore Protection Manual”, Vol. 1. Coastal Engineering Research Center, Vicksburg, USA (1984)
- [57] Van der Vorst, H.A., “Bi-CGSTAB: A fast and smoothly converging variant of Bi-CG for the solution of nonsymmetric linear systems”, *SIAM J. Sci. Stat. Comput.*, 13(2): 631-644 (1992)
- [58] Van Vledder, G.P., J.G. de Ronde and M.J.F. Stive, “Performance of a spectral wind-wave model in shallow water”, *Proceedings of 24th International Conference on Coastal Engineering*, Am. Soc. of Civ. Eng., New York. 761-774 (1994)
- [59] Vuik, C., “Solution of the discretized incompressible Navier-Stokes equations with the GMRES method”, *Int. J. Numer. Methods Fluids*, 16: 507-523 (1993)

- [60] WAMDI Group, “The WAM model—a third generation ocean wave prediction model”, *J. Phys. Oceanogr.*, 18: 1775-1810 (1988)
- [61] Whitham, G.B., “Linear and nonlinear waves”, Wiley, New York, 636 p. (1974)
- [62] Whitney, M. M. “Simulating the Delaware coastal current”, Ph.D. Dissertation, University of Delaware, DE, USA (2003)
- [63] Wilkin, J. and K.S. Hedström, “User’s manual for orthogonal curvilinear grid-generation package”, October 9 (1998)
- [64] Wu, J., “ Wind-stress coefficients over sea surface from breeze to hurricane”, *J. Geophys. Res.*, 87, C12: 9704-9706 (1982)